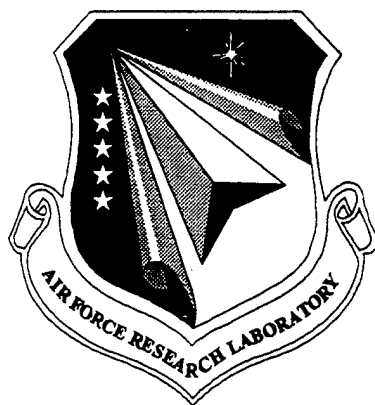


AFRL-VA-WP-TR-1998-3003

**ANALYSIS OF LIMIT CYCLE
OSCILLATION/TRANSONIC HIGH
ALPHA FLOW VISUALIZATION**



Part 1: Discussion

**Atlee M. Cunningham, Jr.
Lockheed Martin Tactical Aircraft Systems
Fort Worth TX**

and

**Evert G. M. Geurts
National Aerospace Laboratory (NLR)
Amsterdam, The Netherlands**

19980915 068

JANUARY 1998

FINAL REPORT FOR PERIOD OCTOBER 1994 - OCTOBER 1997

Approved for public release; distribution unlimited

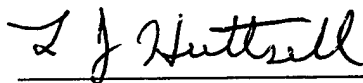
**AIR VEHICLES DIRECTORATE
AIR FORCE RESEARCH LABORATORY
AIR FORCE MATERIEL COMMAND
WRIGHT-PATTERSON AIR FORCE BASE, OH 45433-7542**

NOTICE

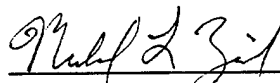
When Government drawings, specifications, or other data are used for any purpose other than in connection with a definite Government-related procurement, the United States Government incurs no responsibility or any obligation whatsoever. The fact that the Government may have formulated or in any way supplied the said drawings, specification, or other data, is not to be regarded by implication, or otherwise in any manner construed, as licensing the holder, or any other person or corporation, or as conveying any rights or permission to manufacture, use, or sell any patented invention that may in any way be related thereto.

This report is releasable to the National Technical Information Service (NTIS). At NTIS, it will be available to the general public, including foreign nations.

This technical report has been reviewed and is approved for publication.



L. J. HUTTSELL
Project Engineer
Vibration & Aeroelasticity Branch



MIKE ZEIGLER
Core Area Leader
Structural Integrity of Aging Aircraft



BRADLEY J. BUXTON, CAPT, USAF
Acting Chief, Vibration & Aeroelasticity Branch
Structures Division

If your address has changed, if you wish to be removed from our mailing list, or if the addressee is no longer employed by your organization, please notify AFRL/VASV Bldg. 45, 2130 Eighth St Ste 1, WPAFB OH 45433-7542 to help maintain a current mailing list.

Copies of this report should not be returned unless return is required by security consideration, contractual obligations, or notice on a specified document.

REPORT DOCUMENTATION PAGEForm Approved
OMB No. 0704-0188

Public reporting burden for this collection of information is estimated to average 1 hour per response, including the time for reviewing instructions, searching existing data sources, gathering and maintaining the data needed, and completing the reviewing the collection of information. Send comments regarding this burden estimate or any other aspect of this collection of information including suggestions for reducing this burden, to Washington Headquarters Services, Directorate for Information Operations and Reports, 1215 Jefferson Davis Highway, Suite 1204, Arlington, VA 22202-4302, and to the Office of Management and Budget, Paperwork Reduction Project (0704-0188), Washington, DC 20503.

1. AGENCY USE ONLY (Leave Blank)		2. REPORT DATE January 1998	3. REPORT TYPE AND DATES COVERED FINAL REPORT - OCT 94 to OCT 97	
4. TITLE AND SUBTITLE ANALYSIS OF LIMIT CYCLE OSCILLATION/TRANSONIC HIGH ALPHA FLOW VISUALIZATION Part 1: Duscussion			5. FUNDING NUMBERS C: F49620-94-C-0093 PE: 62201F PR: 2401 TA: LE WU: 00	
6. AUTHOR(S) ATLEE M. CUNNINGHAM, JR., EVERT G. M. GEURTS				
7. PERFORMING ORGANIZATION NAME(S) AND ADDRESS(ES) Lockheed Martin Tactical Aircraft Systems, Fort Worth TX National Aerospace Laboratory (NLR), Amsterdam, The Netherlands			8. PERFORMING ORGANIZATION REPORT NUMBER	
9. SPONSORING / MONITORING AGENCY NAME(S) AND ADDRESS(ES) Air Vehicles Directorate Air Force Research Laboratory Air Force Materiel Command Wright-Patterson Air Force Base, Oh 45433-7542 POC: L. J. Huttshell, AFRL/VASV, 937-255-7384			10. SPONSORING / MONITORING AGENCY REPORT NUMBER AFRL-VA-WP-TR-1998-3003	
11. SUPPLEMENTARY NOTES				
12a. DISTRIBUTION / AVAILABILITY STATEMENT Approved for public release; distribution unlimited.			12b. DISTRIBUTION CODE	
13. ABSTRACT (Maximum 200 words) A flow visualization test was conducted with the simple straked wing in August, 1996 (at the National Aerospace Laboratory [NLR], The Netherlands), for the purpose of obtaining flow visualization data to complement the pressure and force data base generated in earlier tests of the same configuration. This test was conducted in two parts to examine the flow field characteristics (1) at high alpha conditions that involve vortices, shocks, and separated flows, and (2) at low alpha conditions typical of transonic LCO flows with and without tip stores. Laser light sheet/water vapor techniques were used to illuminate the flows, and video recording was used to obtain the data. Both low and high speed video cameras were used to examine spanwise and streamwise laser sheet positions. In addition, under NLR funding, some preliminary particle image velocimetry (PIV) data were obtained at M= 0.225 and 0.6, as well as some pulsed laser flow visualization (9 nano-sec pulse) at M=0.9. Correlation was performed between the flow visualization data from this test and the pressure/force data obtained in 1992 on the same configuration.				
14. SUBJECT TERMS unsteady aerodynamics, transonic, high incidence flow, flow visualization, limit cycle oscillation			15. NUMBER OF PAGES	
			16. PRICE CODE	
17. SECURITY CLASSIFICATION Unclassified	18. SECURITY CLASSIFICATION OF THIS PAGE Unclassified	19. SECURITY CLASSIFICATION OF ABSTRACT Unclassified	20. LIMITATION OF ABSTRACT SAR	

TABLE OF CONTENTS

	Page
FOREWORD	ix
SUMMARY	
LIST OF FIGURES	v
LIST OF TABLES	vii
NOMENCLATURE	viii
 1.0 INTRODUCTION	 1
 2.0 BACKGROUND SUMMARY	 3
2.1 High Alpha Conditions	3
2.1.1 Low Speed Aerodynamic Characteristics	3
2.1.2 Transition from Low Speeds to Transonic Speeds	6
2.1.3 Transonic Aerodynamic Characteristics	6
2.2 LCO Conditions	10
2.2.1 Clean Wing Aerodynamic Characteristics	11
2.2.2 Wing With Tip Launcher Aerodynamic Characteristics	14
 3.0 DESCRIPTION OF THE EXPERIMENT AND DATA BASE	 16
3.1 Test Setup and Procedures	16
3.2 Flow Visualization Data Base for the Stationary Model	24
3.3 Flow Visualization Data Base for the Oscillating Model	25
3.4 Video Tape Data Base	26
 4.0 STEADY AND UNSTEADY FLOWS AT M=0.6 FOR THE CLEAN WING	 31
4.1 Steady Aerodynamic Characteristics for M = 0.6	31
4.1.1 Linear Flow for M = 0.6	31
4.1.2 Vortex Flow for M = 0.6	33
4.1.3 Burst Vortex Flow for M = 0.6	33
4.2 Unsteady Aerodynamic Characteristics for M = 0.6	34
4.2.1 Linear Unsteady Flow for M = 0.6	34
4.2.2 Unsteady Vortex Flow for M = 0.6	36
4.2.3 Unsteady Burst Vortex Flow for M = 0.6	37

TABLE OF CONTENTS (CONTD)

	Page
5.0 STEADY AND UNSTEADY FLOWS AT M=0.9 FOR THE CLEAN WING	39
5.1 Steady Aerodynamic Characteristics for M = 0.9	39
5.1.1 Attached Transonic Flow for M = 0.9	39
5.1.2 SITES and Tip Leading Edge Separation for M = 0.9	40
5.1.3 Transonic Vortex Flow for M = 0.9	42
5.1.4 Shocklets and Finger Vortex Structure for M = 0.9	49
5.1.5 Turbulent Separation Boundary for M = 0.9	51
5.2 Unsteady Aerodynamic Characteristics for M = 0.9	52
5.2.1 Attached Unsteady Transonic Flow for M = 0.9	52
5.2.2 Unsteady SITES and Leading Edge Flows for M = 0.9	54
5.2.3 Unsteady Transonic Vortex Flow for M = 0.9	55
5.2.4 Unsteady Shocklets and Finger Vortex Structure for M = 0.9	56
5.2.5 Unsteady Turbulent Separation Boundary for M = 0.9	57
 6.0 STEADY AND UNSTEADY LCO-TYPE FLOWS FOR THE WING WITH/WITHOUT TIP STORES	 59
6.1 Model LCO with Wing Tip Launcher	59
6.2 Steady Aerodynamic Characteristics for LCO-Type Flows	62
6.2.1 Clean Wing LCO-Type Flows	63
6.2.2 Wing with Tip Missile/Launcher LCO-Type Flows	65
6.2.3 Wing with Tip Launcher LCO-Type Flows	69
6.3 Oscillatory Aerodynamic characteristics for LCO-Type Flows	71
6.3.1 Oscillating Clean Wing LCO-Type Flows	71
6.3.2 Oscillatory Wing with Tip Missile/Launcher LCO-Type Flows	72
6.3.3 Oscillatory Wing with Tip Launcher LCO-Type Flows	73
 7.0 CONCLUSIONS	 75
 8.0 REFERENCES	 77

LIST OF FIGURES

<u>Figure</u>	Page
1 Full Span and Semi-Span Models of the Simple Straked Wing Configuration	4
2 Steady Force and Moment Results for the Full Span Straked Wing at $M = 0.225$ (Reference 1)	5
3 Comparison of Steady Force and Moment Results for the Semi-Span and Full-Span Straked Wing Models at $M = 0.225$	7
4 Effect of Mach Number on the Semi-Span Simple Straked Wing Model C_N and C_m in the NLR HST	8
5 Steady Force and Moment Characteristics for the Simple Straked Wing Semi-Span Model at $M = 0.9$	9
6 Integrated Unsteady Pressures at Section 4 Showing the Effect of Mach Number for the Clean Wing/Body Configuration (Reference 8)	12
7 Pressure Distributions at Sections 3 and 4 for the $M = 0.90$ Anomaly at $\alpha = 8$ deg for the Clean Wing/Body Configuration (Reference 8)	13
8 Integrated Unsteady Pressures at Section 4 Showing the Effect of Leading Edge Flap Deflection at $M = 0.93$ for the Wing/Body With Tip Launcher Configuration (Reference 8)	15
9 Semi-Span Straked Wing Model and Instrumentation	17
10 Laser Light Sheet Positions for Various Configurations	19
11 Vapor Screen Visualization Setup for High Speed and Conventional Video Cameras in the HST	20
12 High Speed Video Frame and Nomenclature	21
13 Negative High Speed Video Frame Format Used in Parts 2 and 3 of this Report	22
14 Particle Image Velocimetry Setup with the Pulsed Laser in the HST	23
15 Effect of Mach Number on Mean Pressure Section Characteristics	32

LIST OF FIGURES (CONT'D)

<u>Figure</u>	Page
16 Pitch Up/Push Over Maneuver Motion Between $\alpha = 7.2^\circ$ and $\alpha = 37.7^\circ$ for $M = 0.60$	35
17 PIV Data Frame for $M = 0.225$ at 20 deg (Reference 18)	44
18 PIV Calculations for $M = 0.225$ at 20 deg (a) First Example	45
(b) Second Example	46
19 PIV Calculations for $M = 0.6$ at 16 deg (a) First Example	47
(b) Second Example	48
20 Pitch Up/Push Over Maneuver Motion Between $\alpha = 7$ deg and $\alpha = 37$ deg for $M = 0.90$	53
21 Tip Launcher Pitch Mode on the Straked Wing Model at 68.5 Hz	60
22 Tip Missile/Launcher Pitch Mode on the Straked Wing Model at 70.0 Hz	60
23 Angular Response of the Tip Launcher Configuration During LCO, $M = 0.85$, $d\alpha = \pm 0.5$ deg	61
24 Flow Visualization for the Clean Wing at $M = 0.9$, $\alpha = 11$ deg (Stationary), Time Sequence Showing Natural Unsteadiness (Data Point 47, Sheet Position 12)	66
25 Variation of Spanwise Separation Locations at the Three Sheet Positions, 11, 12, and 13 at $M = 0.9$ for the Tip Missile/Launcher Configuration	68
26 Flow Visualization for the Tip Missile/Launcher Configuration at $M = 0.9$, $\alpha = 9.51$ deg (Stationary), Illustrating Multiple Flow States (Data Point 261, Sheet Position 13)	70

LIST OF TABLES

<u>Table</u>		Page
1	Listing of Data on the Composite High Speed Video/Side Camera Tape	28

NOMENCLATURE

C_m	=	wing pitching-moment coefficient
C_N	=	wing normal-force coefficient
C_p	=	pressure coefficient
	=	$(p - p_s)/Q$
$(C_p)_i$	=	unsteady pressure coefficient
	=	$p_i/Q\Delta\alpha$
	=	$\text{Re}(C_p) + i\text{Im}(C_p)$
$(C_p)_m$	=	mean pressure coefficient
C_r	=	reference chord, 0.821 m
f , FREQ	=	frequency, Hz
i	=	SQRT (-1)
k	=	reduced frequency, $= \pi f C_r / V$
M , MACH	=	freestream Mach number
m	=	wing pitching moment, positive nose up
N	=	wing normal force, positive up
p	=	pressure at model surfaces
p_s	=	freestream static pressure
Q	=	dynamic pressure
S	=	wing area, 0.144 m ²
V	=	freestream velocity, m/s
α	=	angle of attack, deg
$\Delta\alpha$, $d\alpha$	=	amplitude of pitching motion, deg
δ	=	control surface deflection, deg

Subscripts

i	=	unsteady
m	=	mean
LEF	=	leading edge flap
tip	=	wing tip pressure row

FOREWORD

This report summarizes the results of an investigation into transonic unsteady aerodynamics. Transonic wind tunnel tests were conducted for a semispan straked delta wing model with and without tip stores. Laser light sheet and water vapor were used to obtain flow visualization data to complement force and pressure data obtained in a previous test with the same model.

This test was conducted under a cooperative program of research between the Lockheed Martin Tactical Aircraft Systems (LMTAS), Fort Worth, Texas, USA and the National Aerospace Laboratory (NLR), Amsterdam, The Netherlands. The test was conducted in August, 1996 at NLR. The model and support system were designed and fabricated at NLR under an earlier subcontract during 1989 to 1993 from LMTAS (previously the Fort Worth Division of General Dynamics) that was funded under Air Force Contract F33657-84-C-0247 (CCP4551) for the Aeronautical Systems Center, Wright Patterson Air Force Base, Ohio. Additional funding was also provided for this earlier effort by NLR and the Dutch Ministry of Defense. The August, 1996 flow visualization test preparation, wind tunnel test, and reporting were performed at NLR under a follow-on subcontract from LMTAS. This work was conducted under Air Force Contract F49620-94-C-0093, Air Force Office of Scientific Research, Bolling Air Force Base, DC and administered by Dr. Leonidas Sakell, AFOSR/NA. Funding was provided by the Wright Laboratory Flight Dynamics Directorate, Wright Patterson Air Force Base, Ohio and administered by Mr. L. J. Huttshell (AFRL/VASV). Additional funding was provided by NLR. With funding provided by the Dutch Ministry of Defense, the test was extended with additional measurements on the tip launcher and tip missile configurations. This funding was monitored by Mr. C. Hoffman and Mr. E. Bos of The Netherlands Agency for Aerospace Programmes (NIVR-Contract: 07501N).

The Program Manager was Dr. A. M. Cunningham, Jr. at LMTAS. The principal investigators were Dr. Cunningham at LMTAS, Mr. E. G. M. Geurts at NLR, and Mr. R. G. den Boer (during the early part of the program) also at NLR. Assistance was provided by the following NLR specialists, C.D.G. Dogger, A. J. Persoon, and R. J. Zwaan.

This test is documented in three parts. This report (Part 1, AFRL-VA-WP-TR-1998-3003) presents background, test setup, and data base descriptions. A detailed discussion of results is also given with continuous references to the data presented in Parts 2 and 3, AFRL-VA-WP-TR-1998-3004 and AFRL-VA-WP-TR-1998-3005. Part 2 includes a large selection of flow visualization video frames and accompanying pressure data for the model stationary at varying Mach and incidence. Part 3 is similar to Part 2, but is for the model oscillating in pitch at both small and large amplitudes also for varying Mach and incidence. The three parts are listed below:

1. "Analysis of Limit Cycle Oscillation/Transonic High Alpha Flow Visualization, Part 1: Discussion", AFRL-VA-WP-TR-1998-3003.
2. "Analysis of Limit Cycle Oscillation/Transonic High Alpha Flow Visualization, Part 2: Stationary Model Data", AFRL-VA-WP-TR-1998-3004.
3. "Analysis of Limit Cycle Oscillation/Transonic High Alpha Flow Visualization, Part 3: Oscillating Model Data", AFRL-VA-WP-TR-1998-3005.

This page intentionally left blank.

1.0 INTRODUCTION

Steady and unsteady low speed wind tunnel tests were conducted in 1986 on a pitching simple straked wing model representative of modern fighter aircraft which make use of a strake/wing combination to achieve good high angle of attack aerodynamic characteristics (References 1 and 2). The model was oscillated in pitch at amplitudes sufficient to represent rapid pitch-ups and push-overs at dynamically-scaled full scale maneuver times. Force and pressure data, as well as flow-visualization information, were obtained so that a better understanding of the developing flow fields associated with such maneuvers could be obtained. These extensive analyses, which have been documented in References 3 through 6, show how wing and strake vortices develop and interact, as well as how they break down and collapse to fully stalled flows.

The interest to extend this understanding to include compressibility effects led to the consideration of another test of a similar configuration at transonic speeds. In addition, flight experience in the late 70's and early 80's with various fighter aircraft showed that limited amplitude aeroelastic oscillations (LCO) at lower angles of attack presented a serious problem by imposing further flight envelope restrictions which had not been foreseen with conventional flutter analyses and wind tunnel testing. Thus, plans were made to conduct a combined wind tunnel test, using a common instrumented wing panel to investigate (1) unsteady transonic pressures and forces for fighter configurations at typical LCO flow conditions, and (2) unsteady pressures and forces for a simple straked wing under the same dynamical conditions tested at low speeds in 1986, but at increasing speeds up to the transonic regime. These planned tests, as discussed in References 7 and 8, were accomplished in September, 1991 for the LCO test (Reference 8) and in May, 1992 for the simple straked wing test (Reference 9).

The simple straked wing test had the straightforward objective to simply extend the understanding of flow fields at low speeds and high incidences up to transonic speeds and high incidences. The LCO test, however, had the objective of providing information that could be used to help develop a prediction method for full scale LCO characteristics of elastic aircraft. The specific flow phenomenon of interest was shock-induced trailing edge separation (Reference 10) which was known to exist under conditions typical of a certain variety of transonic LCO. Early prediction method developments which modeled these flow phenomena showed promise for predicting this class of LCO using (1) steady pressure data, and (2) some type of algorithm for simulating unsteady effects, as were discussed in References 11 and 12. Recent developments based on these concepts have shown that LCO can be predicted for specific configurations (Reference 13) and more general configurations (Reference 14).

The prediction methods of References 13 and 14 utilize (1) arbitrary symmetric, antisymmetric and/or asymmetric vibration modes, (2) a steady, pressurized data base, and (3) a generic time domain algorithm for simulating unsteady aerodynamic effects with the steady pressure data. These ingredients are combined into a set of non-linear

time varying equations of motion which are integrated to produce a time history of LCO development or decay. In addition, the generic method of Reference 14 also permits the input of arbitrary aerodynamic turbulent excitation to simulate wide band buffeting or discrete frequency flutter type excitation typically used in flight testing.

Analyses of this force and pressure data from the simple straked wing (Reference 9) and the LCO configuration (Reference 8) raised many questions concerning the nature of the flow fields involved. These questions were further augmented as a result of a preliminary flow visualization investigation conducted on the simple straked wing at the conclusion of that test in May, 1992 (Reference 15). The objectives of this test and the LCO test in September, 1991 were to understand the physics of unsteady transonic flows at both LCO and high incidence conditions and to develop appropriate data bases to be used for development of LCO prediction methods and validating computational fluid dynamic codes for realistic flow phenomena. Thus, further flow visualization testing was needed in order to answer the questions that were raised in References 8, 9, and 15.

A flow visualization test was conducted with the simple straked wing in August, 1996 (at the National Aerospace Laboratory [NLR], The Netherlands), with the purpose of meeting the needs outlined above. This test was conducted in two parts to examine the flow field characteristics (1) at high alpha conditions that involve vortices, shocks, and separated flows, and (2) at low alpha conditions typical of transonic LCO flows with and without tip stores. Laser light sheet/water vapor techniques were used to illuminate the flows, and video recording was used to obtain the data. Both low and high speed video cameras were used to examine spanwise and streamwise laser sheet positions. In addition, under NLR funding, some preliminary particle image velocimetry (PIV) data were obtained at $M = 0.225$ and 0.6 , as well as some pulsed laser flow visualization (9 nano-sec pulse) at $M = 0.9$. Complete details of the test setup, procedures, data points and data base are given in the NLR test report (Reference 16).

This report, Part 1, will present the results of the above test and discussions of what has been observed. First, a brief background summary will be given to provide a basis for the discussions to follow. Next, a description of the experiment and the data base that is included in Parts 2 and 3 of this report will be presented. Finally, three sections that discuss the results will be presented covering: (1) steady and unsteady flows at $M = 0.6$ for the clean wing at high angles; (2) steady and unsteady flows at $M = 0.9$ for the clean wing at high angles; and (3) LCO flow conditions at $M = 0.9$ for the wing with and without tip stores at low angles.

2.0 BACKGROUND SUMMARY

Detailed discussions of force and pressure data for (1) high alpha conditions on the simple straked wing are given in Reference 9, and (2) for LCO conditions with and without tip stores are given in References 8 and 17. The following discussions will present highlights from those of References 8, 9, and 17, as well as pertinent figures for use in later discussions of the 1996 flow visualization results.

2.1 High Alpha Conditions

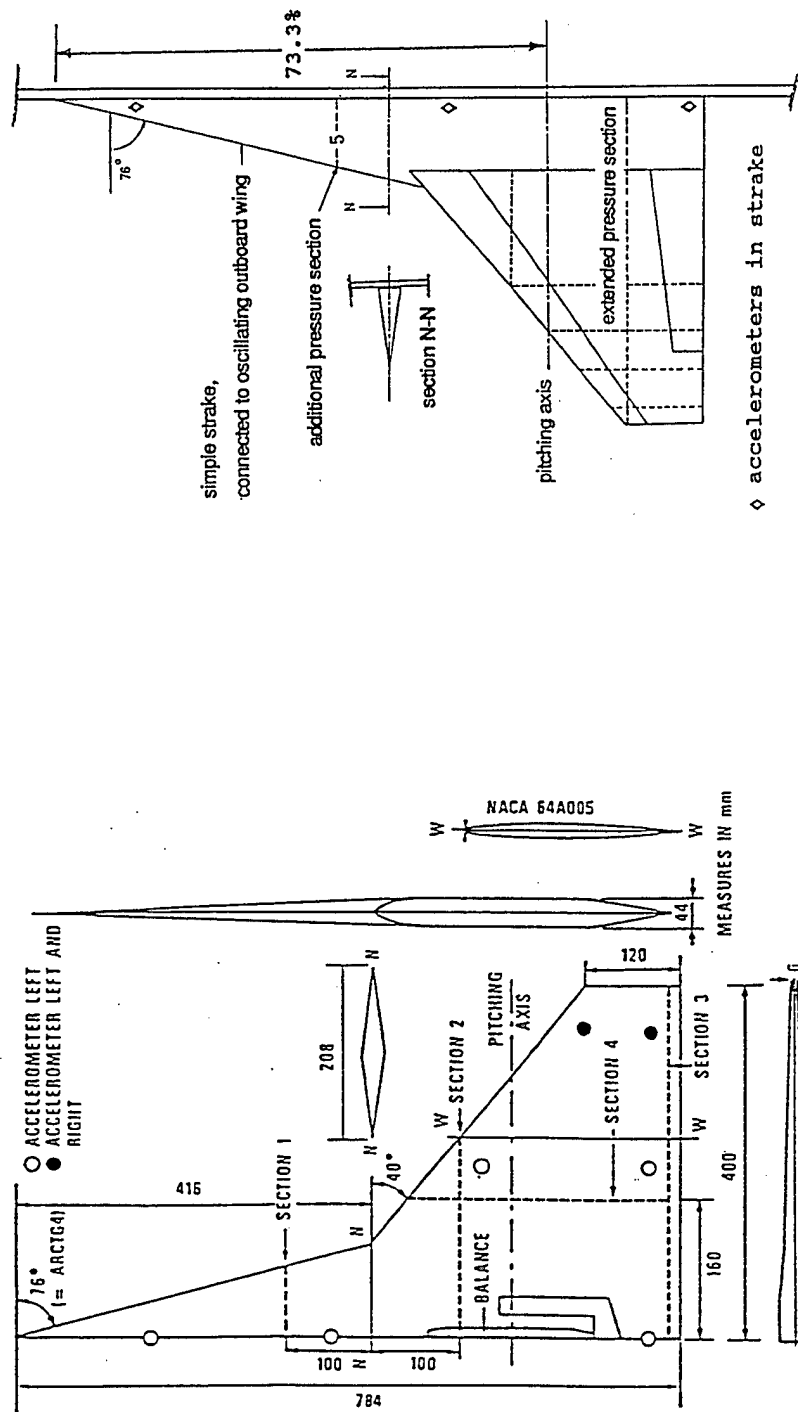
2.1.1 Low Speed Aerodynamic Characteristics

A low speed test of the full span straked wing model was conducted at NLR in 1986 (References 1 - 6). This model was instrumented for force and unsteady pressure measurements. Incidences of from -8 deg up to 50 deg were tested with the model, both stationary and oscillating in pitch at either 0 deg or ± 5 deg sideslip. Amplitudes of oscillation ranged from ± 2 deg to ± 18 deg. The Mach number was constant at $M = 0.225$ with a Reynolds number of 3.7×10^6 based on the root chord. The model and instrumentation are shown in Figure 1. The variations of steady normal force, C_N , and pitching moment, C_m , with angle of attack, α , are shown in Figure 2 for zero sideslip. Important flow field characteristics and transitions are also denoted where the "sections" referred to in those notations are the pressure transducer rows shown in Figure 1.

The "linear" range of aerodynamic force development is clearly evident in Figure 2 in both C_N and C_m data. This break signals the onset of vortex burst which represents the limit of vortex strength that can be maintained by the flow fields. Bursting tends to occur simultaneously for the wing and strake vortices when the two merge. This break also signals the end of significant C_N development up to its maximum level.

For increasing angle in the burst vortex regime, the strake vortex strength increases, but the burst point continues to move forward. These opposing trends result in a much lower slope in the C_N curve as shown in Figure 2, however, the slope is almost constant from $\alpha = 19$ deg to about 34 deg. The gain in lift forward, due to strake vortex strength increase, and the loss in lift aft, due to burst forward movement, produces a pitch-up in the C_m as also shown in Figure 2. Beyond the maximum value of C_N at $\alpha = 36$ deg, the flow over the entire wing and strake rapidly collapses to completely separated or flat plate flow. Under these conditions for increasing angle, the normal force is falling off and the center of pressure is moving toward the geometric centroid of the planform, as indicated by a rapid decrease in pitching moment.

The semi-span model tested in 1992 was shown in Reference 9 to correlate reasonably well with the full span model at $M = 0.225$ and a Reynolds number of 3.7×10^6 . However, the semi-span model was tested at a higher Reynolds number of 8.0×10^6 .



Full-Span
Model

Semi-Span
Model

Figure 1 - Full Span and Semi-Span Models of the Simple Straked
Wing Configuration

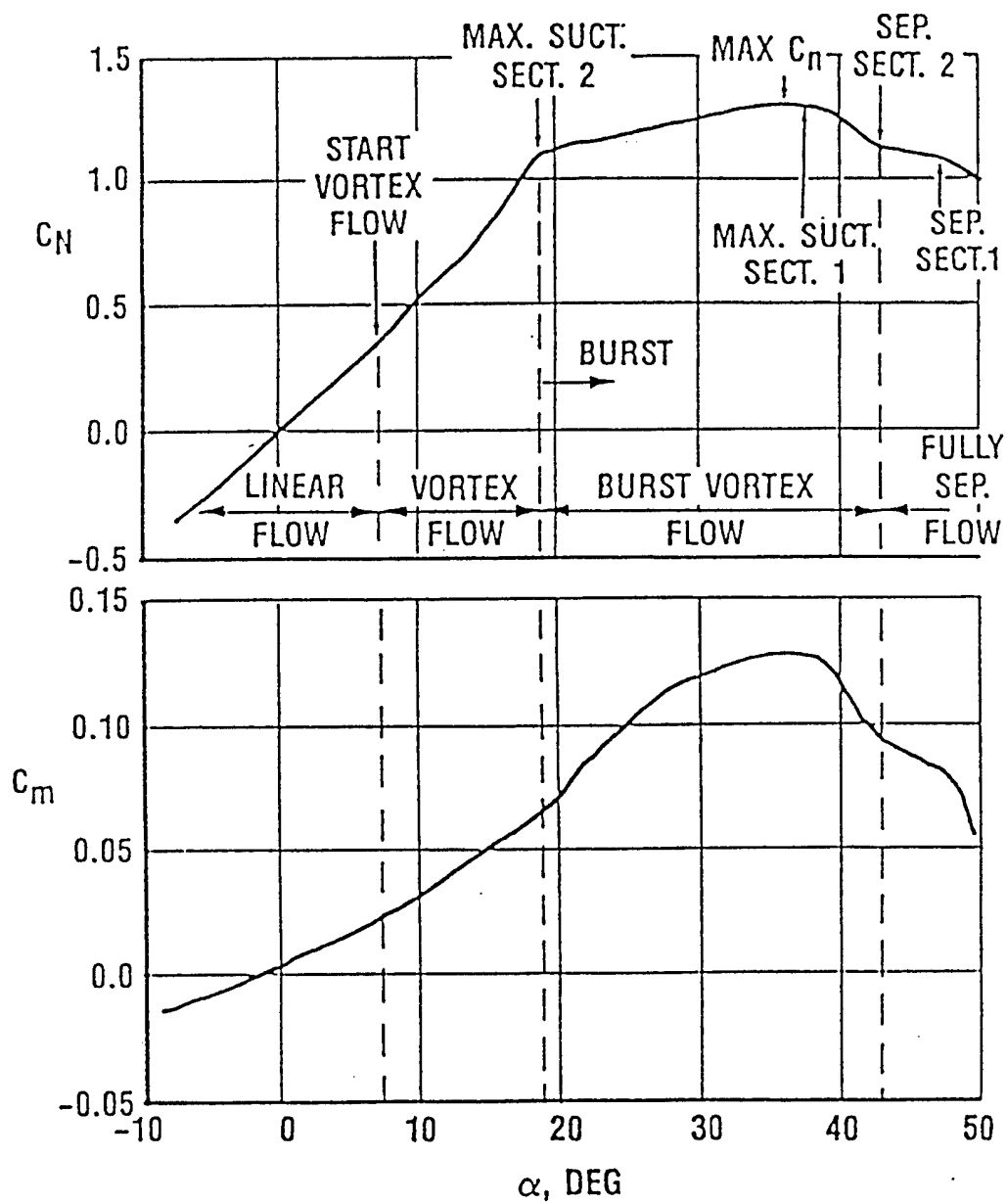


Figure 2 - Steady Force and Moment Results for the Full Span Straked Wing at $M = 0.225$ (Reference 1)

for increasing Mach from 0.225 to 0.9. A comparison of the full and semi-span data at the two different Reynolds numbers at $M = 0.225$ is shown in Figure 3 where three differences are noticed. First, vortex bursting occurs at a higher angle on the semi-span model at 22 deg than on the full span model at 19 deg. This difference is primarily attributed to wing tip twist. Second, the maximum value of C_N occurs at 31 deg on the semi-span model, but at 36 deg on the full span model. This influence is attributed to the semi-span effect where wall boundary layer weakens vortical flows at high angles as was discerned from the pressure data comparisons in Reference 9. Third, the maximum value of C_N is lower for the semi-span model which is also attributed to semi-span effects. Fully stalled flow, however, seems to develop at about 42 deg for both models.

Although the exact points for critical flow transitions do not completely match for the two models, the trends are very similar, indicating that the important flow mechanisms were preserved on the semi-span model.

2.1.2 Transition from Low Speeds to Transonic Speeds

Results for the semi-span model are shown in Figure 4 for $M = 0.225$, 0.6, and 0.9 for a Reynolds number of 8×10^6 . All three C_N curves are very similar with exception of (1) the higher slope at $M = 0.9$ and angles less than 10 deg, and (2) the higher peak at about 24 deg for $M = 0.6$. The C_m curves are also very similar, and show a typical aft movement of the center of pressure with increasing Mach.

Based on analysis of pressure data, the flow field characteristics at $M = 0.6$, are very similar to those at $M = 0.225$, as shown in Figure 2. The peak at about 24 deg in the $M = 0.6$ C_N curve is caused by a more severe process of vortex bursting where lift over most of the wing is affected. At $M = 0.225$, this process occurs more toward the trailing edge, and hence, is not as noticeable.

Although the C_N and C_m curves at $M = 0.9$ are similar to the others over much of the angle range, the flow characteristics are very different. The only common feature is the strake vortex.

2.1.3 Transonic Aerodynamic Characteristics

Discussions were presented in References 9 and 15 in which a transonic version of Figure 2 was developed, based on analysis of the force and pressure data, as well as some preliminary flow visualization results. These corresponding characteristics are shown in Figure 5 for the clean wing at $M = 0.9$ in terms of normal force, C_N , and pitching moment, C_m . The Reynolds number was 8.0×10^6 , and the model was oscillated continuously in pitch at ± 0.5 deg and 6 Hz during the incidence sweep. This small amplitude oscillation eliminated static hysteresis effects and provided some amount of smoothing to the data.

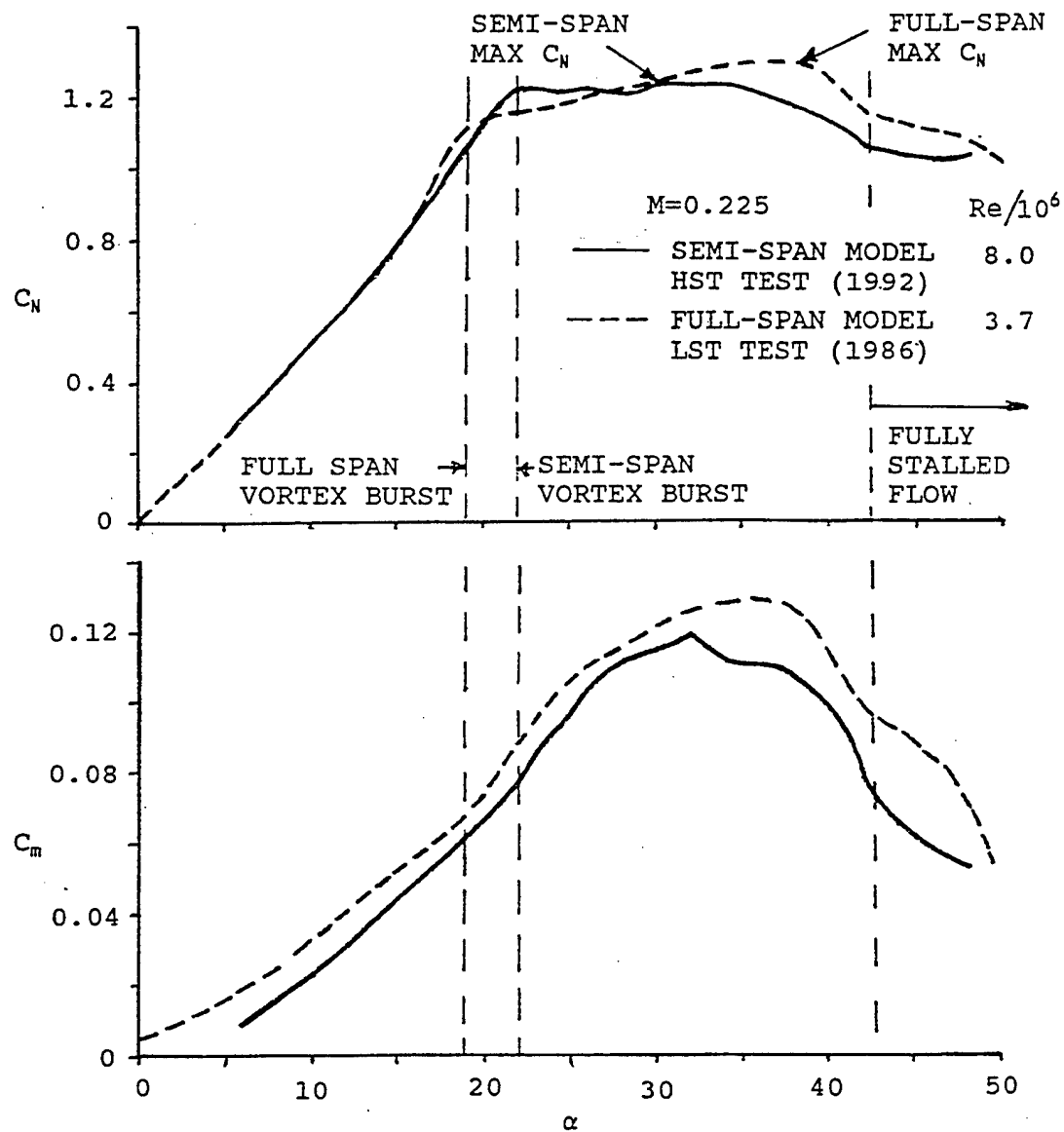


Figure 3 - Comparison of Steady Force and Moment Results for the Semi-Span and Full-Span Straked Wing Models at $M = 0.225$

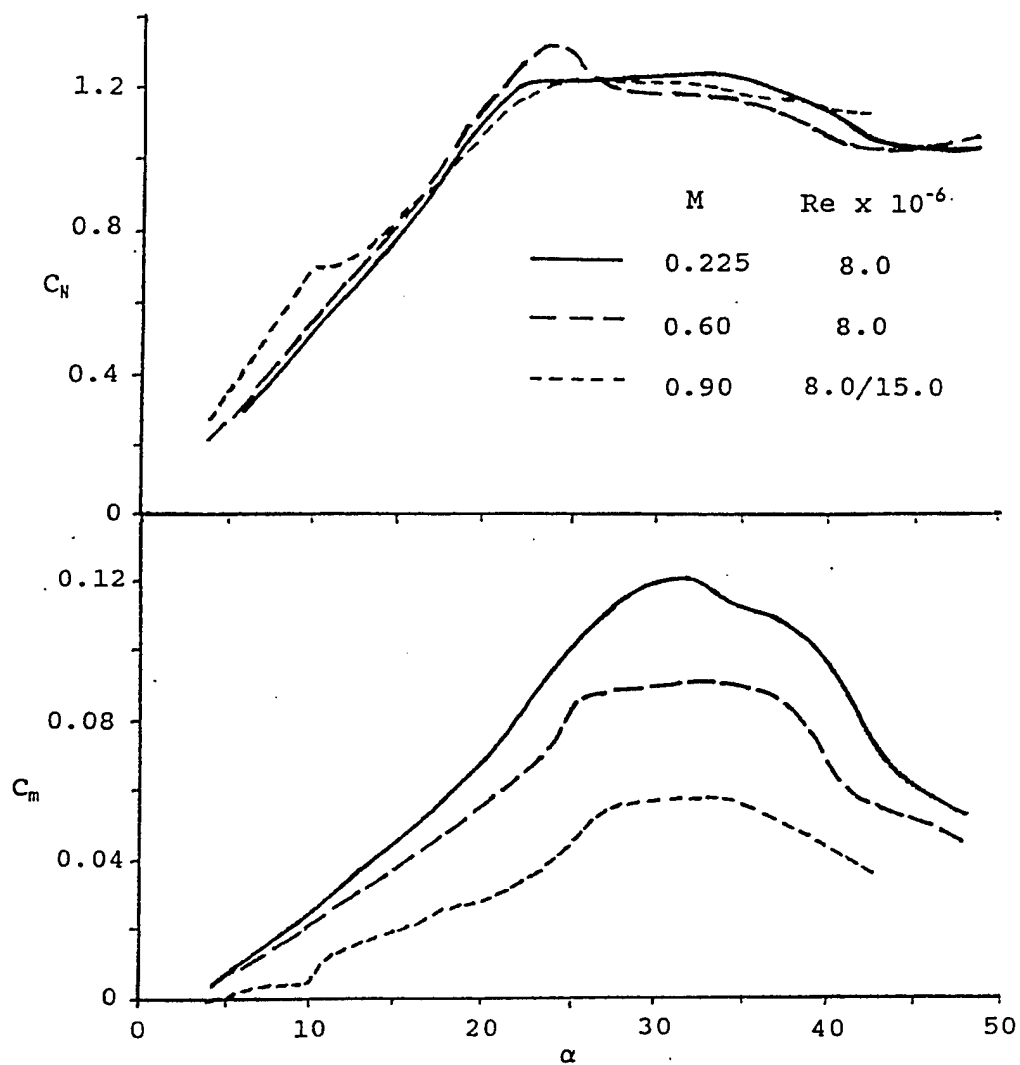


Figure 4 - Effect of Mach Number on the Semi-Span Simple Straked Wing Model C_N and C_m in the NLR HST

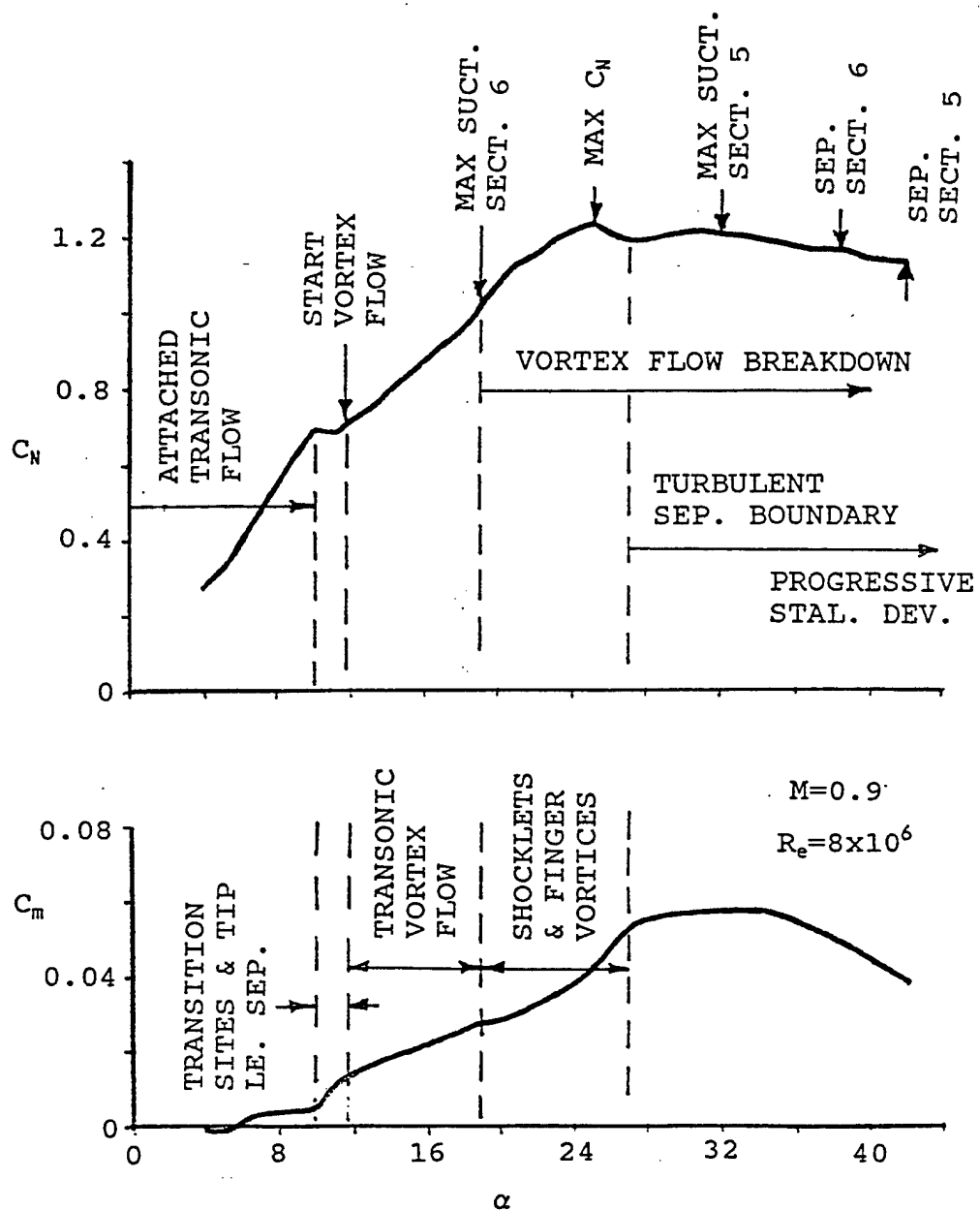


Figure 5 - Steady Force and Moment Characteristics for the Simple Straked Wing Semi-Span Model at $M = 0.9$

The trends up to about 10 deg represent essentially attached transonic flow developments which are dominated by shocks on the 40 deg swept outer wing panel. With incidence increasing beyond 10 deg, the formation of shock-induced trailing edge separation (SITES) occurs at about 10.5 deg over the outer 20% of the wing. A further increase to above 11.0 deg results in the onset of leading edge separation which is indicated at the three outboard streamwise pressure rows 2, 3, and 4 (see Figure 1). These two transitions result in a flat C_N slope and a pitch-up in C_m , as seen in Figure 5.

Above 11.0 deg, vortex flow development begins with the strake vortex. There does not appear to be a wing vortex analogous to that seen at lower speeds as postulated in References 9 and 15. Instead, the outer wing flows appear to be dominated by a mixture of leading edge separation, SITES, and forward shock development.

At around 18.5 deg, the outboard wing flow transitions to a new structure referred to as "finger vortices" and "shocklets" as was seen in the flow visualization data (Reference 15). This transition also corresponds to the occurrence of maximum suction at the spanwise pressure row, Section 6 (see Figure 1). Development of this new flow continues up to about 27.0 deg and has a more forward lift location as indicated by a greater pitch-up trend in the C_m curve. The strake vortex continues to develop until at about 25.5 deg, bursting appears in the pressure data and in the flow visualization data (Reference 15) at Section 7 (see Figure 1).

Above 27.0 deg, the finger vortex/shocklet structure breaks down, and vortex burst continues to develop. In this region, leading edge separation is becoming dominant over the outer wing panel, as indicated in both the pressure data and appearance of a "turbulent separation boundary". At about 42 deg, the wing is fully stalled and the strake is stalling in a manner similar to that seen in the cases of lower speed flows.

These characteristics will be further discussed and modified later in this report utilizing all of the flow visualization data obtained in the 1996 test at NLR.

2.2 LCO Conditions

A comprehensive investigation was conducted to better understand the non-linear aerodynamics associated with transonic LCO (References 8 and 17), as well as to develop a method for quantitatively predicting LCO response amplitudes (References 13 and 14). The experimental program described in Reference 8 was based on transonic wind tunnel testing of a wing-fuselage model with various underwing and wing tip stores. This wing panel could be oscillated in pitch at high frequencies representative of structural vibration modes, whereas the fuselage was stationary. This panel was instrumented with accelerometers, high response pressure transducers, and a main wing balance; and had deflectable leading and trailing edge flaps. The outboard 40 deg swept part of the simple straked wing model is that same wing panel used in the LCO test.

As a result of the analyses conducted in Reference 13, a parameter was found that was a good indicator of LCO sensitivity for the configuration of interest. This parameter was the chordwise integration of the upper surface pressure data on the most outboard chordwise row (Section 4 in Figure 1) of transducers on the model. This pressure row also showed the most activity with regard to SITES flow developments and transitions in both steady and unsteady flows.

2.2.1 Clean Wing Aerodynamic Characteristics

The effects of Mach number on the unsteady aerodynamics of the clean outboard wing panel in the presence of a stationary fuselage are shown in Figure 6 (Reference 8). The wing panel was oscillating at 40 Hz with an amplitude of ± 0.5 deg. Results shown in Figure 6 and the unsteady $C N_{tipi}$ and $C m_{tipi}$ obtained by chordwise integration of the measured unsteady pressure data from Section 4. They are cast in the in-phase (real) and out-of-phase (imaginary) part relative to the wing pitching oscillations.

The trends shown in Figure 6 illustrate the effects of Mach number for $M = 0.90$, 0.93 , and 0.945 . All three trends are similar with exception of the large spike at 8 deg in the imaginary parts of both $C N_{tipi}$ and $C m_{tipi}$ for $M = 0.90$. An examination of the steady and unsteady pressure data revealed that these peaks correspond to the SITES transition at the Section 4 location. The large imaginary spikes are a direct result of aerodynamic lag in the transition from attached to separated flow and vice versa. This lag effect is further illustrated in Figure 7 (Reference 8) where the mean and unsteady pressure distributions at Sections 3 and 4 (see Figure 1) are shown for the large spike condition at angles of 7.5, 8.0, and 8.5 deg. The trends shown indicate that the spike at 8.0 deg is real, and it results from the flow transition that occurs between 7.5 deg and 8.5 deg.

The SITES transition at Section 4, referred to in Figures 6 and 7, occurs at an angle of 8.0 deg for the clean LCO configuration, whereas for the clean simple straked wing configuration, the same transition occurs at about 10.5 deg. The difference is attributed to the stronger aft shock produced by the presence of the fuselage in the LCO configuration.

The results shown in Figures 6 and 7 are prime examples of the sensitive nature of transonic separation flows where small changes of 0.5 deg in mean angle can produce large changes in the unsteady aerodynamic forces. Since these components have a first order effect in amplifying or damping disturbances seen by the wing, these variations imply that dynamic aeroelastic stability can change completely with a 0.5 deg change in mean incidence.

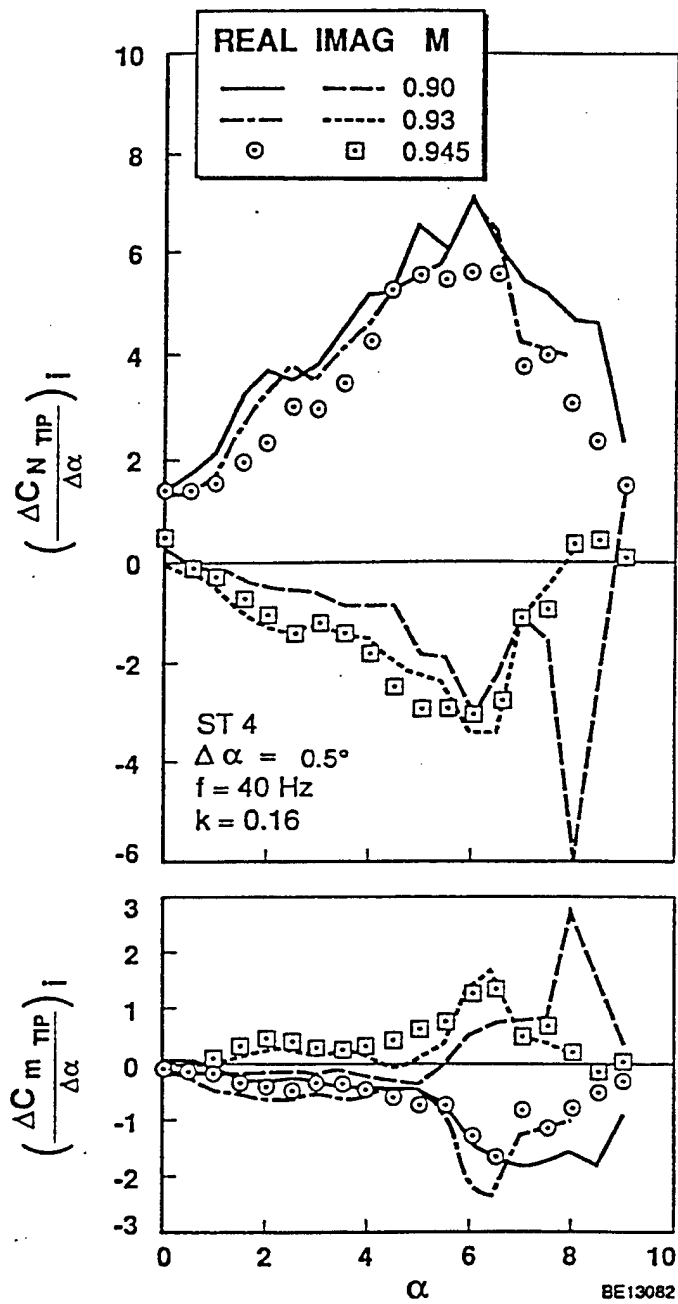


Figure 6 - Integrated Unsteady Pressures at Section 4 Showing the Effect of Mach Number for the Clean Wing/Body Configuration (Reference 8)

$f = 40 \text{ hz}$ ——— $\alpha_m = 8.0^\circ$
 $k = 0.16$ - - - - $\alpha_m = 7.5^\circ$
 $d\alpha = 0.5$ - - - - $\alpha_m = 8.5^\circ$

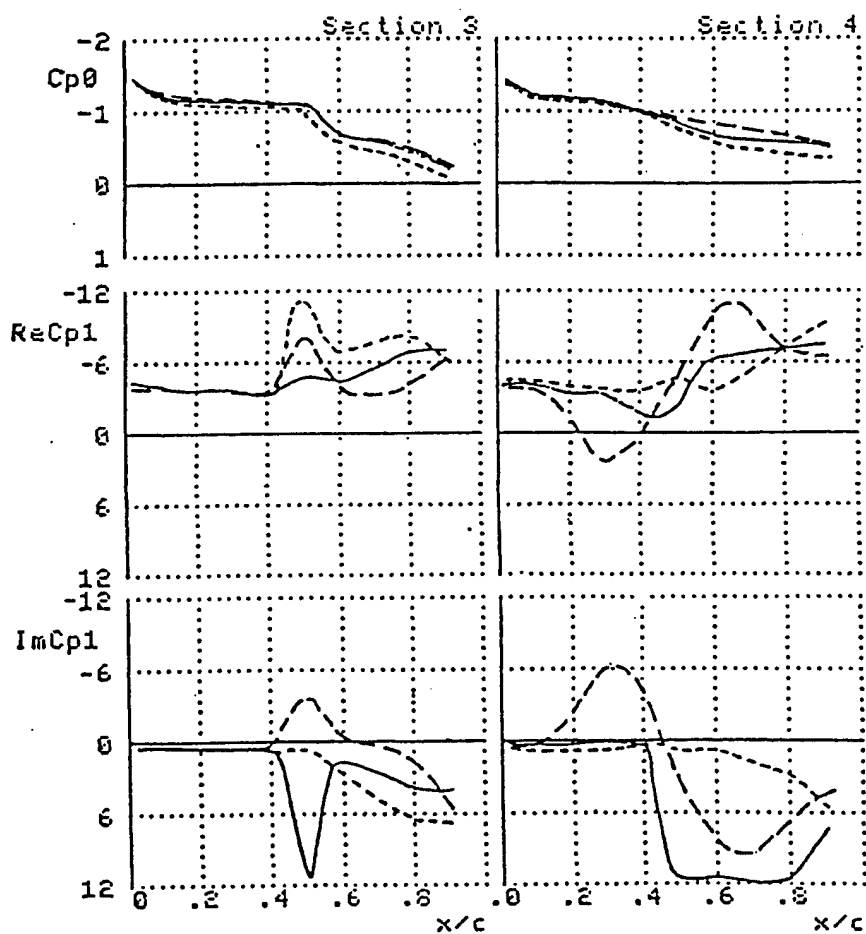


Figure 7 - Pressure Distributions at Sections 3 and 4 for the M = 0.90 Anomaly at $\alpha = 8^\circ$ for the Clean Wing/Body Configuration (Reference 8)

2.2.2 Wing With Tip Launcher Aerodynamic Characteristics

The effects of adding a tip launcher and underwing stores are shown in Figure 8, along with the additional effects of deflecting the leading edge flap 2.5 deg nose down (Reference 8). The conditions were $M = 0.93$, oscillation amplitude of ± 0.5 deg, and frequency of 40 Hz which are the same as those at $M = 0.93$ in Figure 6. The principal effect seen with addition of the stores in Figure 8 as compared with $M = 0.93$ results in Figure 6, is an overall reduction in the magnitudes of $C N_{tipi}$ and $C m_{tipi}$. The trends with incidence are about the same, except that the abrupt changes at $\alpha = 6.5$ deg and above in Figure 6 are considerably intensified in Figure 8 for no leading edge flap deflection ($\delta_{lef} = 0$ deg). The majority of these effects are produced by the tip store, while the underwing stores have little effect.

Results shown in Figure 8 for a leading edge flap setting at $\delta_{lef} = 2.5$ deg nose down, provide a classic example which illustrates the displacement of major flow transitions by an incremental angle that is similar to the flap deflection angle. The large discontinuities at 6.5 and 7.0 deg for $\delta_{lef} = 0$ deg are pushed up to about 9.0 and 9.5 deg for $\delta_{lef} = 2.5$ deg, but their characteristic shapes are very similar. This implies that the basic flow field transitions which produce these changes still occur with $\delta_{lef} = 2.5$ deg, but at a higher mean angle.

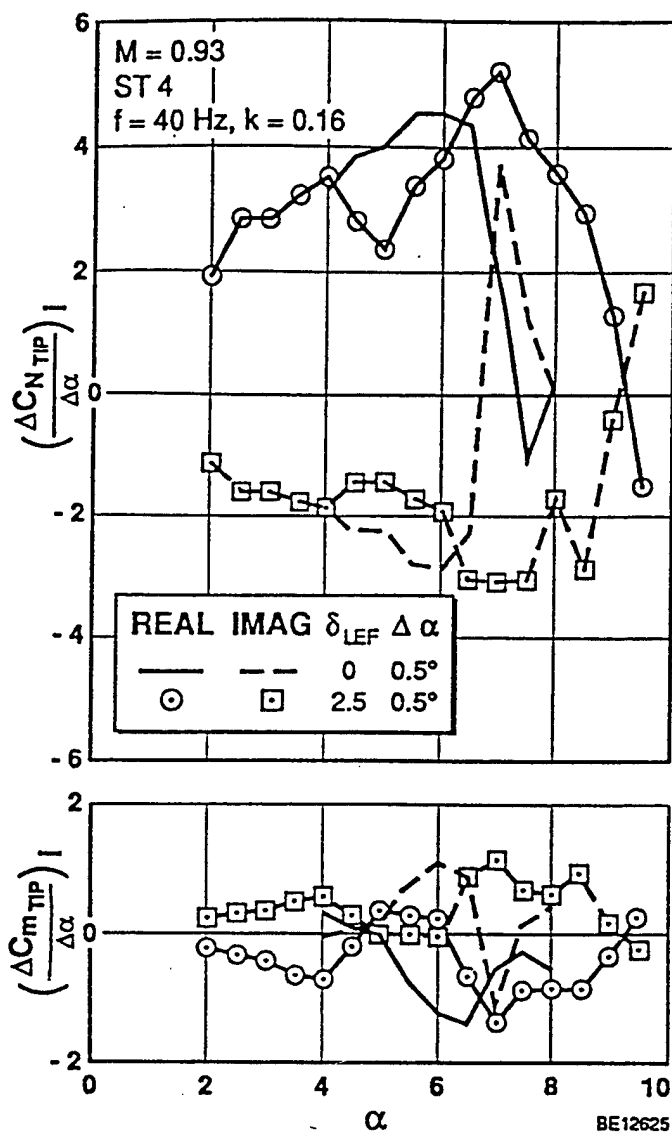


Figure 8 - Integrated Unsteady Pressures at Section 4 Showing the Effect of Leading Edge Flap Deflection at $M = 0.93$ for the Wing/Body With Tip Launcher Configuration (Reference 8)

3.0 DESCRIPTION OF THE EXPERIMENT AND DATA BASE

This section presents a brief description of the flow visualization experiment conducted at NLR in August of 1996 on the simple straked wing model. Next a summary is given for the flow visualization data base contained in Part 2 of this report for the stationary model, followed by a similar summary for Part 3 of this report pertaining to the oscillating model. Finally, brief descriptions are given for several VHS video tapes which are very helpful in understanding the unsteady flow fields.

3.1 Test Setup and Procedures

The simple straked wing model used in this flow visualization test in August, 1996 was the same model used in the force/pressure test up to post stall conditions at transonic speeds in May, 1992 at NLR (Reference 9). The objective of the 1996 test was to obtain flow visualization data that would complement the force and pressure data obtained in 1992. Thus, test conditions for the second test were driven by those of the first test.

A complete description of the NLR high speed wind tunnel (HST) in Amsterdam and its operation is given in Reference 16. Also included in Reference 16 are descriptions of the model, model support, model excitation (pitch oscillation), instrumentation, and flow visualization setup. A description of the pulsed laser flow visualization and particle image velocimetry (PIV) setup is included in Reference 18. The following discussions will present brief summaries of the above subjects.

The flow visualization test was conducted in the NLR HST located in Amsterdam. The tunnel has a closed circuit with a test section length of about 2.5m. It was operated with a 2.0m x 1.6m test section in order to be compatible with the force/pressure test conducted in 1992. Sidewall mounting was used for the semi-span straked wing model also, as was done in the 1992 test. The tunnel has a Mach range of 0.3 to 1.2, and a maximum Reynolds number of 22×10^6 per meter at $M = 0.95$.

The model was the semi-span, simple straked wing configuration shown in Figure 1 which was supported on a semi-span balance that was driven by a hydraulic actuator mounted on a movable turntable. This arrangement permitted independent control of oscillatory pitching motion and model mean angle-of-attack. Although equipped with leading and trailing edge flaps, neither could be deflected. Tip stores used in the previous LCO test in 1991 (Reference 8) at NLR were also used in this test for investigating the effects of tip stores on flow fields at LCO-type conditions.

The model was instrumented with a main wing semi-span balance, tip store balance, dynamic incidence transducer, in situ pressure transducers, and vertical accelerometers, all located as shown in Figure 9. The pressure transducers were taped over for this flow visualization test and were not operative. The pressure rows, however,

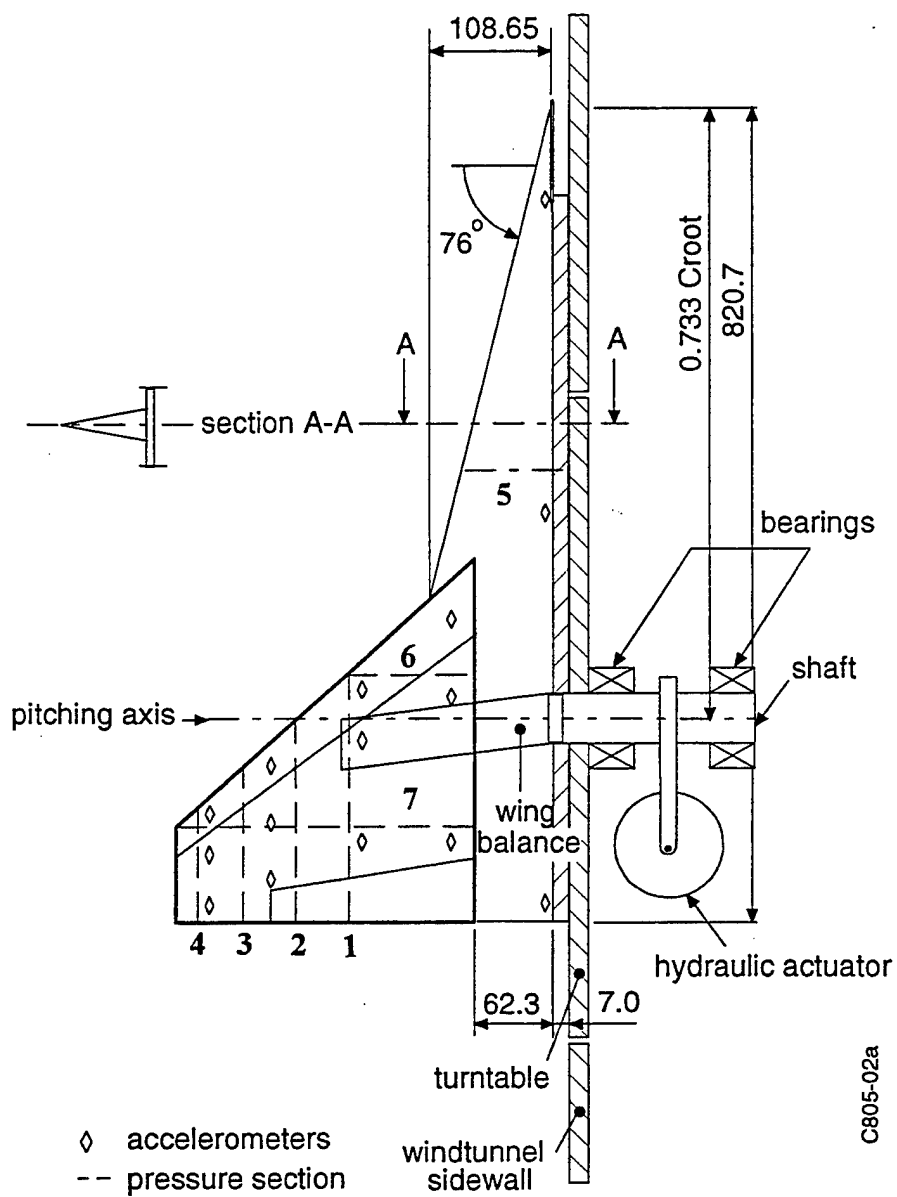


Figure 9 - Semi-Span Straked Wing Model and Instrumentation

were used as reference positions for the laser light sheet locations. Numbering and locations of the light sheet positions are shown in Figure 10, where it will be noted that these numbers do not generally correspond to those for the pressure rows in Figure 9.

Flow visualization was accomplished by controlling humidity in the wind tunnel by spraying water downstream of the model into the tunnel, as needed, and varying the tunnel temperature as pressure during the test. This approach provided the proper conditions to produce water condensation only in the expansion regions above the model. The technique worked for both $M = 0.6$ and 0.9 flows, but was not usable at $M = 0.225$. Illumination of the water vapor was achieved with a 5-watt continuous argon laser whose beam was spread into a sheet with a cylindrical lens (See Figure 11). The sheet position and orientation was remotely controlled on a traversing system which provided a coverage that exceeded the model dimensions. High speed video recording with the Kodak Intensified High Speed Video Camera (IHSV) was accomplished only for span-wise sheet orientations, however conventional video recording was accomplished from both downstream (sting camera) and side view directions, also shown in Figure 11. The high speed video recordings were in a positive format of white vapor image on black background, as shown in Figure 12. This positive image was inverted and reversed, since the camera view was through a mirror, as shown in Figure 11. The frame also includes time and identification information, as well as other data, as noted in Figure 12. A negative image of the IHSV frames provided improved quality and contrast for use in this final report, as is shown in Figure 13.

The pulsed laser flow visualization and PIV setup is shown in Figure 14 (Reference 18). Side view mounting for the high resolution camera lids was used in order to conduct preliminary tests on making PIV measurements at high speeds. The pulsed laser was set at a single streamwise position (Number 3 in Figure 10), and all PIV and flow visualization measurements were at this position. Seeding for PIV was accomplished at $M = 0.225$ and 0.6 by injecting oil smoke and nebulized oil into the settling chamber from a rake. At $M = 0.9$, flow visualization was accomplished with water vapor in the same manner as discussed above.

At the beginning of the test program, force measurements were made with both dry air and humid condensing air in order to evaluate the effects of moisture on the model aerodynamics. The differences were small, but were documented in Reference 16. With exception of the high angle testing, wing and tip store balance loads were measured during the flow visualization testing. These data are listed in tabular form in Reference 16 (Part II) for both steady mean and the first and second harmonic for unsteady loads. Accelerometer measurements were recorded for all test points and are given in both tabular and plotted form in Reference 16 (Part II).

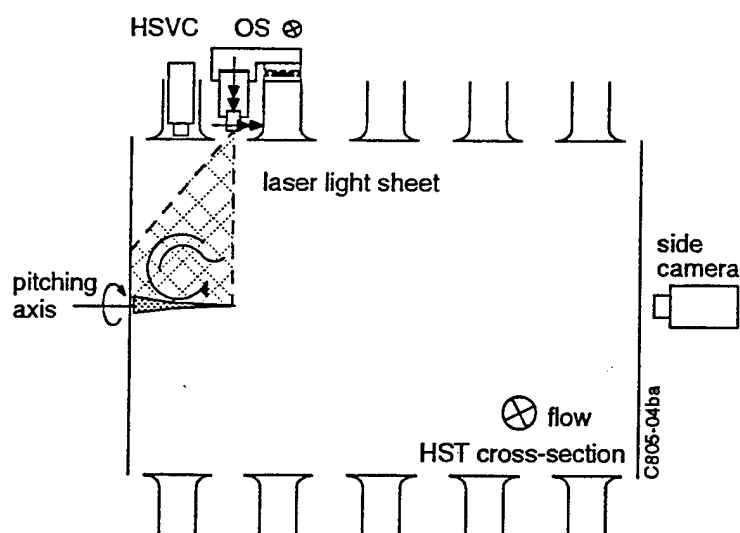
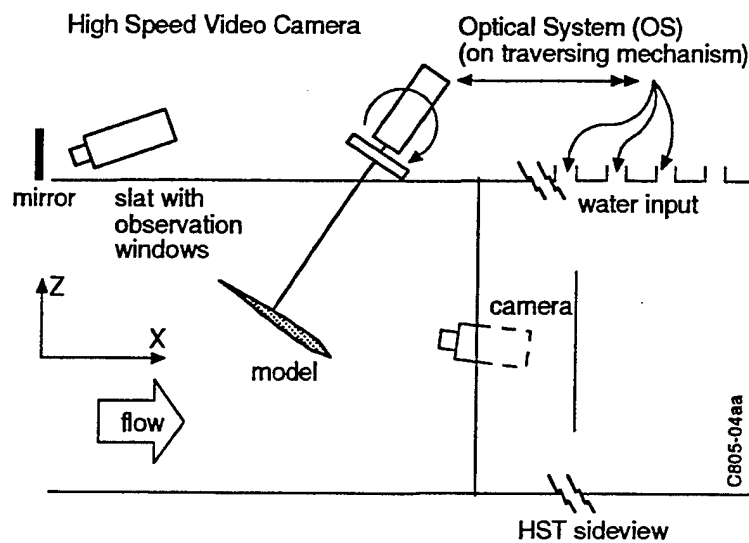


Figure 11 - Vapor Screen Visualization Setup for High Speed and Conventional Video Cameras in the HST

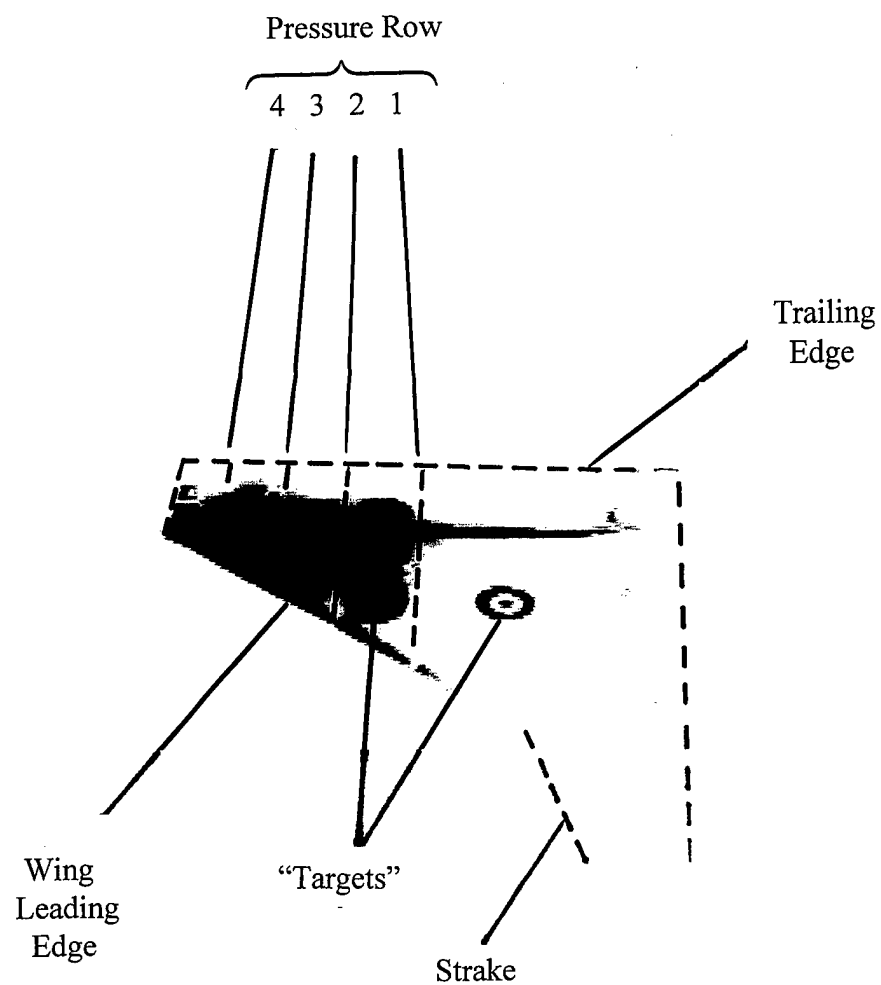


Figure 13 - Negative High Speed Video Frame Format Used in Parts 2 and 3 of this Report

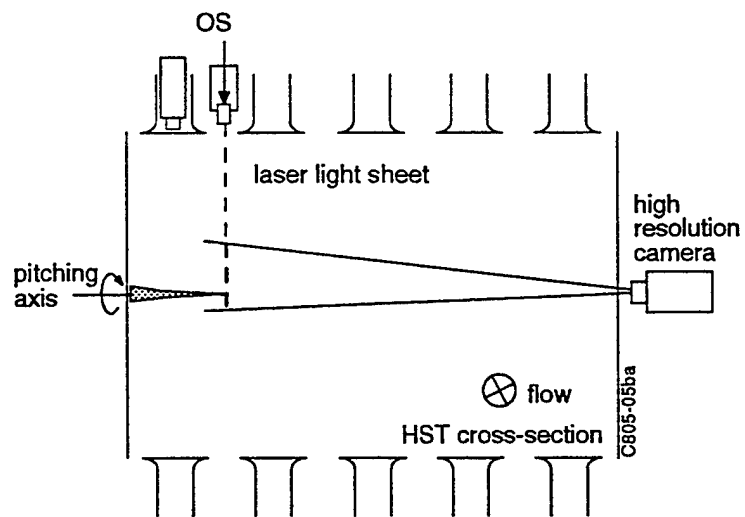
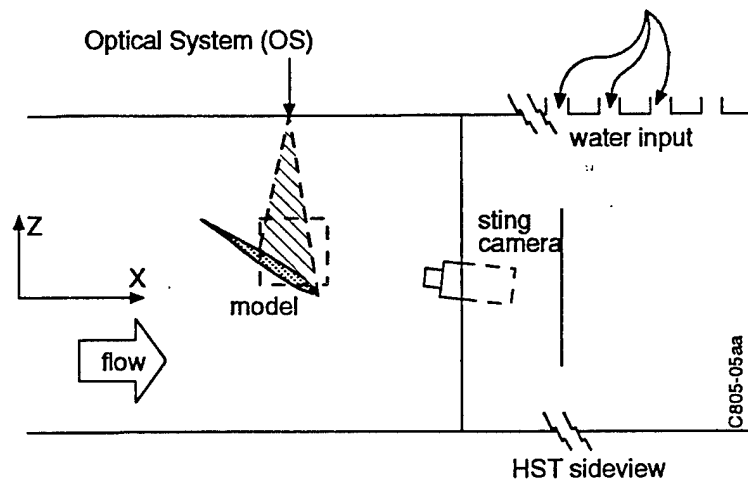


Figure 14 - Particle Image Velocimetry Setup with the Pulsed Laser in the HST

3.2 Flow Visualization Data Base for the Stationary Model

This data base is presented in Part 2 of this report and includes pressure data plots (Reference 9) and flow visualization video frames from the high speed camera, low speed side view camera, and the high resolution camera (pulsed laser light sheet). The conditions are steady model incidence, but in cases of flow separation, the flow is inherently unsteady. This format was selected in order to facilitate understanding of the discussions in Part 1, where constant reference to the figures is necessary. Six sections are included in Part 2, and will be briefly described in the following paragraphs.

Sections 1.0 and 2.0 present individual frames from the high speed video data base (1000 frames per second) on tape for spanwise sheet positions 8 and 9, as shown in Figure 10 for the clean wing configuration. Section 1.0 covers $M = 0.6$ conditions at sheet position 9 only, and Section 2.0 covers $M = 0.9$ conditions at sheet positions 8 and 9. These data were taken from a slow incidence sweep for which the video data were stored only on VHS tape. The angles chosen for presentation were selected to correspond to pressure data points that are available from Reference 9. Both pressure and flow visualization data are shown in a side-by-side format in order to permit direct correlation. In addition, the white vapor image on black background of the high speed video data base was reversed to provide a dark vapor image on white background. This negative image was superior in contrast and detail to the original positive image. An example of the negative image is shown in Figure 13, where it is mounted right side up and has been cropped to reduce wasted space. Important details in the frame are also noted to aid in interpretation of the data.

Section 3.0 presents individual frames from the side view camera recordings for three chordwise sheet positions, 1, 3, and 14, as shown in Figure 10 for the clean wing configuration. In addition, several frames are presented that were obtained during a rotating sweep of the light sheet from Position 8 toward the wing tip. These data were taken during a slow incidence sweep for which the video frames were recorded on VHS tape at the conventional frame rate of 50 frames per second. Hence, no instantaneous flow structures are recorded, but the time-averaged images provide another view that is very complementary to the high speed camera recordings. The four sheet position data frames were selected to match the incidence values shown in the figures in Section 2.0 of Part 2. The four frames are also grouped together in each figure corresponding to a common incidence value.

Results for flow visualization obtained with a pulsed laser of 9 nano-seconds duration located at sheet position 3 are presented in Section 4.0 for the clean wing configuration. (This was part of an effort funded by NLR to investigate the applicability of particle image velocimetry [PIV] at high speeds, as described in Reference 18.) Selected angles were chosen in order to highlight various flow transition conditions. Although frame rates were limited to 10 frames per second, the high resolution of 1000x1000 pixels and very short exposure time, provided excellent detail of the highly turbulent nature of separated transonic flows. In addition, image enhancement software

was used to bring out even more detail, much of which is not understood at this time. These data shown in Section 4.0 also include multiple shots for the same condition to emphasize natural unsteadiness of the separated flows, where appropriate.

Individual frames from the high speed video data base for LCO-type conditions are presented in Section 5.0 for three spanwise sheet positions, 11, 12, and 13, as shown in Figure 10. (Note: Position 11 is the same as 9, except that it is focused on the outer wing panel.) The clean wing and wing with tip missile configurations are included in this section. The frame rate was 640 frames per second, which was synchronized to give 16 frames per cycle at 40 Hz in order to be compatible with data taken with the model oscillating at ± 0.5 deg. These data are available on the high speed video VHS tape and selected frames in the digital data base (see Reference 16). The data presented in Section 5.0 are from the digital data base, and were selected to highlight the development of flow field differences between the clean wing and wing with tip missile at $M = 0.9$. All images are presented in the negative black-on-white background format used in Sections 1.0 and 2.0.

Section 6.0 presents individual frames from the high speed video data base for LCO-type conditions on the wing with tip launcher configuration at two spanwise sheet positions, 11 and 12, as shown in Figure 10. These data in the negative image format are similar to those presented in Section 5.0, and were selected to highlight the effect of Mach number on the development of LCO-type flows for the tip launcher configuration at $M = 0.85$ and 0.90 . This particular configuration encountered severe 70 Hz LCO at $M = 0.9$, and had to be tested at the lower speed. Limited data were obtained at $M = 0.90$, however, the majority of the testing concentrated on $M = 0.85$. This problem was not encountered with the tip missile configuration. Reasons for these LCO trends have not been determined as yet, but it is suspected that wing tip aerodynamic forces are most likely responsible. Response data are presented in Reference 16 for further investigations.

3.3 Flow Visualization Data Base for the Oscillating Model

This data base is presented in Part 3 of this report, and includes pressure data plots (Reference 9) and flow visualization video frames from the high speed camera in a manner similar to and compatible with Part 2. The conditions and model pitching oscillations at large amplitudes (± 13 deg) for the high incidence clean wing investigations and low amplitudes (± 0.5 deg) for the LCO investigations with and without tip stores. Five sections are included in Part 3 and will be briefly described in the following paragraphs.

Sections 1.0 and 2.0 present individual negative format frames from the high speed video data base (243 frames per second) on tape for the spanwise sheet position 9, as shown in Figure 10 for the clean wing configuration. Section 1.0 covers $M = 0.6$ conditions, and Section 2.0 covers the $M = 0.9$ conditions. These unsteady data

correspond to the steady data presented in Sections 1.0 and 2.0 in Part 2. The flow visualization data were obtained at 64 frames per cycle, with the model oscillating in pitch at 3.8 Hz between the angles of 9 deg and 35 deg, and were recorded only on VHS tape. The corresponding pressure data (Reference 9) were obtained with the model performing single pulsed (1-cos) motions between 7 deg and 37 deg back to 7 deg. Thus, exact matching of model angular positions does not exist at the extremes of motion, but exist at the mean angle of 22 deg. Also, the flow visualization data were obtained with continuous oscillations of the model, whereas the pressure data were obtained with a single pulse transient motion. These differences were found to be important only at the lower angles during the cycle at low speeds (References 1 - 6), and appear to be the same at higher speeds. Even with the differences, both pressure and flow visualization data are shown in Sections 1.0 and 2.0 in a side-by-side format to permit direct correlation on the basis of motion phase angle and approximate correlation on the basis of angle.

Individual negative format frames from the high speed video data base for unsteady LCO-type conditions on the clean wing are presented in Section 3.0 for three spanwise sheet positions, 11, 12, and 13, as shown in Figure 10. (Note: Position 11 is the same as 9, except that it is focused on the outer wing panel.) These data are for the model oscillating, and are the unsteady counterpart of the steady clean wing data in Section 5.0 of Part 2. The frame rate was 640 frames per second, which was synchronized to give 16 frames per second at the model oscillation frequency of 40 Hz. These data are available on the high speed video VHS tape and selected cycles in the digital data base (see Reference 16). The data shown in this section are from the digital data base. Four phase angles were chosen during a cycle of oscillation at ± 0.5 deg amplitude corresponding to (1) 0 deg pitching up through the mean angle, (2) 90 deg at maximum angle, (3) 180 deg pitching down through the mean angle, and (4) 270 deg at minimum angle.

Section 4.0 presents unsteady LCO flow visualization data in the negative image format for the wing with tip missile configuration at $M = 0.9$ in a manner identical to that for the clean wing data in Section 3.0. In addition, data are also presented at $M = 0.85$ at a mean angle of 9.0 deg to illustrate the effect of Mach number with tip missile.

The presentation of unsteady LCO flow visualization for the wing with tip launcher given in Section 5.0 is also identical to that in Sections 3.0 and 5.0. Results for $M = 0.85$ only are shown because of the limited data base available for this configuration. As discussed previously for steady model conditions, severe LCO was encountered on this model which did not occur in the case of wing with tip missile on the clean wing configurations.

3.4 Video Tape Data Base

A complete set of video tapes with recordings of all test conditions with the side and sting-mounted cameras is available (see Figure 11). These cameras ran at the

conventional speed of 50 frames per second (European standard), and produced very high quality images. Listings of the recordings and conditions for all tapes are given in Reference 16. All images are in color and test conditions are shown in each frame, along with time averaged over 1/25 second. The high quality and multiple views provided valuable overall spatial information. This is well illustrated with the frames presented in Section 3.0 of Part 2.

The high speed video data base was recorded in two ways. After a set of digital images was acquired with the Kodak system during the test, all images were transferred to an analog VHS tape, and selected images were transferred to a digital storage device. The digital data have been collected on a CD-ROM, along with the Kodak software necessary to retrieve the images. A complete listing of all data obtained in this manner is given in Reference 16, where the data base is referred to as the Intensified High Speed Video (IHSV) data base. A complete listing of the CD-ROM data base is also given in Reference 16.

A composite, 26-minute video tape of selected side view camera and high speed camera data was assembled in a more logical order as an aid to understanding the phenomena that were recorded during the test. The first part of the tape is dedicated to high alpha conditions for the clean wing, whereas the second part is devoted to LCO conditions with and without tip stores. A listing of the video segments on this tape is given in Table 1.

The tape begins with high speed video recordings of a slow incidence sweep up to 35 deg at $M = 0.6$ for sheet position 9, followed by a sequence with the model oscillating at 3.8Hz between 9 deg and 35 deg. Next, high speed video recordings of a slow incidence sweep up to 35 deg at $M = 0.9$ for sheet position 8, followed by the same at sheet position 9, and then with model oscillating for sheet position 9. Side view camera recordings are then presented for slow incidence sweeps up to 35 deg at sheet positions 3, 1, and 14, as well as the rotating sheet from position 8 to the wing tip. Finally, a spanwise sweep of the laser sheet moving from position 1 to position 14 is shown over a limited incidence range.

The LCO portion of the tape is composed of high speed camera data at sheet positions 11, 12, and 13, with maximum incidences of 11.0 deg from $M = 0.85$ and 0.90. The first record shows a severe LCO condition for the tip launcher configuration at $M = 0.9$, and 10.0 deg incidence for sheet position 11. This is followed by a recording of the same condition with the light sheet on the forward tip of the launcher to highlight severity of the LCO. Next, incidence records from 8.0 deg to 11.0 deg at $M = 0.90$ are shown for sheet position 12 on the stationary model in the clean wing configuration. A similar sequence is then shown for the tip launcher configuration from 7.0 deg to 9.0 deg at $M = 0.85$ which is concluded with the model oscillating at ± 0.5 deg amplitude, 36 Hz and 8.5 deg incidence. Records for the tip missile configuration follow for 7.0 deg to 10.0 deg incidence at $M = 0.9$ where the model oscillating record is for 10.0 deg incidence. The next sequence returns to the clean wing at $M = 0.9$ but at sheet position 13, and an

TABLE 1 - LISTING OF DATA ON THE COMPOSITE HIGH SPEED VIDEO/SIDE CAMERA TAPE

HIGH ALPHA (CLEAN WING)

Test Data Point	IHSV ID	MACH	α (deg)	Model Motion	Sheet Position
-	79	0.6	6-35	SWEEP	9
-	77	0.6	8-36	OSC	9
-	64	0.9	6-35	SWEEP	8
-	69	0.9	6-35	SWEEP	9
-	73	0.9	8-36	OSC	9
-	(Side View)	0.9	1-35	SWEEP	3
-	(Side View)	0.9	1-35	SWEEP	1
-	(Side View)	0.9	35-Down	SWEEP	Rotating
-	(Side View)	0.9	1-35	SWEEP	14

LCO

Test Data Point	IHSV ID	CONFIG	MACH	α (deg)	Model Motion	Sheet Position
168	22	LAU	0.9	10.0	LCO	11
150	03	LAU	0.9	10.0	LCO	Fwd Tip of LAU
-	53	CLEAN	0.9	8.0	STDY	12
-	51	CLEAN	0.9	9.0	STDY	12
-	49	CLEAN	0.9	10.0	STDY	12
-	47	CLEAN	0.9	11.0	STDY	12
183	36	LAU	0.85	7.0	STDY	12
184	37	LAU	0.85	7.5	STDY	12
185	38	LAU	0.85	8.0	STDY	12
186	39	LAU	0.85	8.5	STDY	12
187	40	LAU	0.85	9.0	STDY	12
188	41	LAU	0.85	8.5	OSC, ± 5 deg	12
241	68	LAU/MIS	0.9	7.0	STDY	12
242	69	LAU/MIS	0.9	7.5	STDY	12
243	70	LAU/MIS	0.9	8.0	STDY	12
244	71	LAU/MIS	0.9	8.5	STDY	12
246	72	LAU/MIS	0.9	9.0	STDY	12
247	73	LAU/MIS	0.9	9.5	STDY	12
249	74	LAU/MIS	0.9	10.0	STDY	12
250	75	LAU/MIS	0.9	10.0	OSC, ± 5 deg	12
326	21	CLEAN	0.9	8.0	STDY	13
328	23	CLEAN	0.9	9.0	STDY	13
330	25	CLEAN	0.9	10.0	STDY	13
331	26	CLEAN	0.9	10.0	OSC, ± 5 deg	13
256	83	LAU/MIS	0.9	7.0	STDY	13

**TABLE 1 - LISTING OF DATA ON THE COMPOSITE HIGH SPEED VIDEO/SIDE CAMERA
TYPE (CONTINUED)**

LCO (CONTD)

Test Data Point	IHSV ID	CONFIG	MACH	α (deg)	Model Motion	Sheet Position
257	84	LAU/MIS	0.9	7.5	STDY	13
258	85	LAU/MIS	0.9	8.0	STDY	13
259	86	LAU/MIS	0.9	8.5	STDY	13
260	87	LAU/MIS	0.9	9.0	STDY	13
261	88	LAU/MIS	0.9	9.5	STDY	13
262	89	LAU/MIS	0.9	10.0	STDY	13
263	90	LAU/MIS	0.9	10.0	OSC, ± 5 deg	13
229	54	LAU/MIS	0.9	8.0	STDY	11
243	70	LAU/MIS	0.9	8.0	STDY	12
258	85	LAU/MIS	0.9	8.0	STDY	13
234	61	LAU/MIS	0.9	10.5	STDY	11
238	65	LAU/MIS	0.9	10.5	STDY	12
253	80	LAU/MIS	0.9	10.5	STDY	13

oscillating condition is included at 10.0 deg incidence. The tip missile runs are also repeated at sheet position 13 for the same condition shown at sheet position 12. Finally, the tip missile records are shown for sheet position sweeps 11, 12, and 13 at $M = 0.9$ and at the stationary angles of 8.0 deg and 10.5 deg, respectively, to highlight spatial variations.

All high speed video data shown in this edited tape are in the positive white image on black background format (Figure 12) of the original IHSV tape (see Section 3.1, above). This positive image in the original format was also inverted and reversed, since the camera view was through a mirror, as shown in Figure 11. An example of this image was shown in Figure 12, which includes the time and identification information, as well as other data. The negative image video frames presented in Parts 1 and 3, Sections 1.0 and 2.0, were cut from frame photocopies made of a negative copy of the original IHSV tape, shown in Figure 13. This was done in order to take advantage of the greater detail visible in the negative images and to reduce wasted space on the report pages. These frames were also mounted right side up, so as to correspond to the accompanying pressure data plots. The processed digital images in Parts 2 and 3 for the LCO conditions were also printed in negative form and mounted right side up. Before viewing the edited tape or the IHSV tape, a complete familiarization with images shown in Parts 2 and 3 is recommended so that the time varying effects can be more fully understood.

4.0 STEADY AND UNSTEADY FLOWS AT $M = 0.6$ FOR THE CLEAN WING

This section presents discussions on the pressure and flow visualization data for the clean wing configuration at $M = 0.6$ deg and incidences up to 28 deg for steady flow (model stationary) and 35 deg for unsteady flow (model oscillating). The data to be discussed are the figures in the Sections 1.0 of Part 2 (steady) and Part 3 (unsteady) of this report. Reference to figures in Parts 2 or 3 will be denoted by the part number in parenthesis following the figure call-out, i.e., Figure 4.02 (p.2) refers to Figure 4.02 in Part 2 of this report.

4.1 Steady Aerodynamic Characteristics for $M = 0.6$

As discussed in Section 2, the flow field characteristics at $M = 0.6$ are very similar to those at $M = 0.225$. thus, the characteristics for $M = 0.225$ shown in Figures 2 and 3 are appropriate for $M = 0.6$ flows. The three regimes to be discussed in the following paragraphs are (2) linear flow, (2) vortex flow, and (3) burst vortex flow. Fully separated flow was not visible in this test with the water vapor technique, and will not be addressed.

4.1.1 Linear Flow for $M = 0.6$

This range exists up to about 8 deg, at which point the influence of vortex flow begins to be important. The first appearance of the strake vortex is seen at $\alpha = 11.0$ in the flow visualization data in Figure 2.04 (p.2) and what appears to be the wing vortex at about $\alpha = 8.0$ deg in Figure 2.02 (p.2). The pressure distributions are more sensitive, however, and show that the strake vortex appears before $\alpha = 5.92$ deg at pressure rows 5, 6, and 7 in Figure 2.01 (p.2). At this angle, the outer wing is attached and the wing vortex has not yet appeared. At $\alpha = 7.93$ deg in Figure 2.01(p.2), development of a leading edge vortex on the wing is very apparent where the peak in the spanwise distribution at pressure row 7 corresponds to the wing vortex image in Figure 2.02 (p.2) at $\alpha = 8.0$ deg.

Even though vortex flow developments contribute to the aerodynamic forces at angles less than 8.0 deg, the characteristic is still linear. This is more clearly illustrated in the integrated pressure section steady mean normal force data shown in Figure 15 (from Reference 9) for all three Mach numbers. The pressure rows represented are the chordwise Sections 2 and 4 and the spanwise Sections 5 and 6. Linear variation at Sections 4 (wing tip) and 5(strake) exists up to about 8 deg which must be considered as the limit, even though Sections 2 (inboard) and 6 (wing/strake) continue to be linear up to about 12 deg.

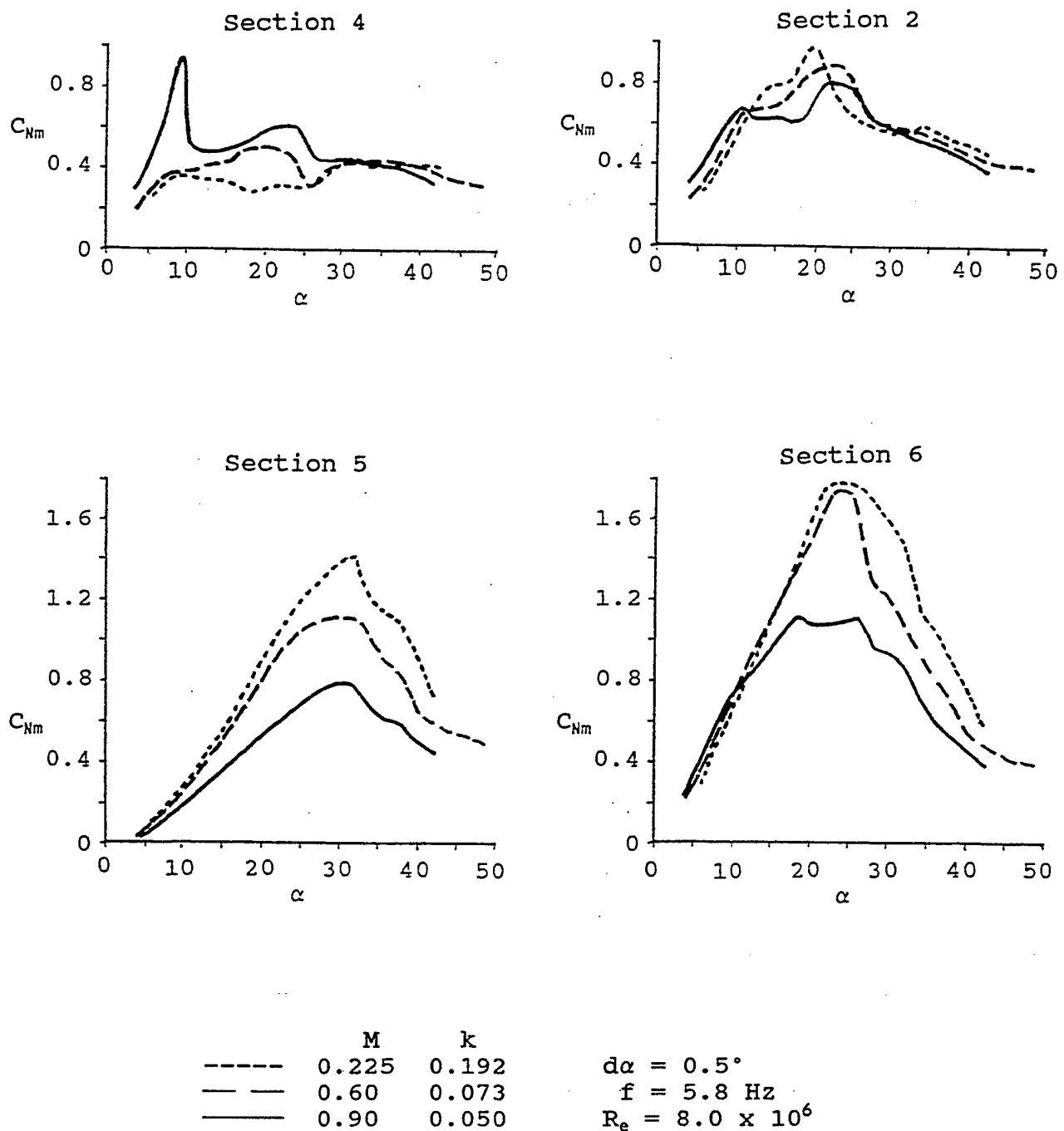


Figure 15 - Effect of Mach Number on Mean Pressure Section Characteristics

4.1.2 Vortex Flow for $M = 0.6$

The continued development of vortex flow characteristics exists up to vortex burst at about 25 deg at $M = 0.6$ which is only slightly higher than the vortex burst angle of 22 deg at $M = 0.225$ (see Figure 3). Growth of the strake vortex is very apparent in Figure 2.04 (p.2) at $\alpha = 11.0$ deg through Figure 2.18 (p.2) at $\alpha = 24.3$ deg. The same trend is reflected in the pressure data in Figure 2.03 (p.2) through Figure 2.17(p.2) at $\alpha = 23.93$ deg.

Wing vortex development is more subtle in the flow visualization data, but is clearly shown in the pressure data over the same α range. Large suction peaks in Sections 1 (forward) and 6 (outboard) are the dominant features in the pressure distribution plots in Figures 2.03 through 2.17(p.2). The wing vortex peak, although more like a hump, in Section 7 is also very apparent in its growth and inboard movement with increasing angle up to 22.94 deg in Figure 2.15(p.2). Above this angle, it rapidly disappears by $\alpha = 24.95$ deg in Figure 2.17(p.2). Flow visualization data show that the strake vortex begins to interact with the wing vortex at about 20.0 deg in Figure 2.14(p.2), and that the latter has broken down by $\alpha = 24.3$ deg in Figure 2.18(p.2). This process is very similar to that described in References 3, 4, 5, and 6 for the full span straked wing model at $M = 0.225$.

The integrated section normal force data in Figure 15 for $M = 0.6$ show that breakdown at the tip Section 4 begins at about 22 to 23 deg in agreement with the results discussed above. It occurs at about 25 deg at Section 2 and 26 deg at Section 6. On the strake at Section 5, the breakdown effect is exhibited as a slope reduction in the normal force.

4.1.3 Burst Vortex Flow for $M = 0.6$

Flow visualization data beyond angles of about 29 deg at $M = 0.6$ were not very useful because of the weak images. However, the important vortex burst transition was captured at $\alpha = 25.5$ deg in Figure 2.18 (p.2) and burst flow was recorded up to 28.4 deg in Figure 2.20 (p.2). The corresponding pressure data shown in Figures 2.17 and 2.19 (p.2) emphasize the overall collapse of the pressures with vortex burst onset. This explains the drop noted in the normal force peak at $M = 0.6$ in Figure 4, as discussed in Section 2.1.2.

The integrated section data in Figure 15 show that the aerodynamic forces vary in a more regular pattern after burst onset. More discussions will be given on this flow regime in Section 4.2.

4.2 Unsteady Aerodynamic Characteristics for $M = 0.6$

This section addresses the effects of model pitching motion on the flow fields discussed above in Section 4.1. Emphasis will be placed on the differences observed between pitching up and pitching down motions, as well as how these relate to conditions for the stationary model at similar angles. References will be made to the figures in Section 1.0 of both Part 2 and Part 3. The three flow regimes discussed will also be (1) linear flow, (2) vortex flow, and (3) burst vortex flow.

4.2.1 Linear Unsteady Flow for $M = 0.6$

The variations of wing normal force, C_N , and pitching moment, C_m , are shown in Figure 16 at $M = 0.6$ for the model at static conditions and pitch-up, pitch-down for a $(1 - \cos)$ motion at 3.8 Hz. With this type motion, the wing starts from rest at 7.2 deg, reaches maximum incidence or 37.7 deg and returns to rest at 7.2 deg where the motion is described by a $(1 - \cos \omega t)$ wave form. Up to about 20 deg, there is very little difference between the normal force curves for static, pitch-up, or pitch-down. The moment trends in Figure 16, show that the static and pitch-up curves are very similar up to about 23 deg, but the pitch-down curve is quite different and exhibits a more nose-up tendency to the minimum angle.

Pressure data shown in Figures 2.01 and 2.03 (p.3) for pitch-up and Figures 2.61 and 2.63 (p.3) for pitch-down corresponds to the linear flow range of 7.32 deg to 8.26 deg. These data also correspond to those shown in Figure 2.01(p.2) for model stationary. With exception of the erroneous pressure spike in pressure row 1 (inboard), the wing data in Figures 2.01 and 2.63(p.3) are very similar in characteristics to those in Figure 2.01(p.2) at $\alpha = 5.92$ deg. The strake vortex pressures at Sections 5, 6, and 7 in Figures 2.01, 2.03, 2.61, and 2.63 (p.3) are more pronounced for both pitch-up and pitch-down than those in Figure 2.01(p.2) at $\alpha = 7.93$ deg. The unsteady wing vortex development in Figures 2.03 and 2.61 (p.3) as compared with stationary data in Figure 2.01 (p.2) at $\alpha = 7.93$ deg are less developed on pitch-up (Figure 2.03[p.3]) and about the same on pitch-down (Figure 2.61 [p.3]).

The unsteady flow visualization data in Figures 2.02 and 2.04 (p.3) for pitch-up and Figures 2.62 and 2.64 (p.3) for pitch-down, do not match the pressure data angles because of the difference in model motion amplitude for the two tests. Since these data start at about 9 deg at the lowest angle, they are outside of the linear range, but still show some interesting characteristics. In Figure 2.02 and 2.04 (p.3) for pitch-up, no strake vortex image is seen up to $\alpha = 9.57$ deg and is similar to the steady flow images shown in Figure 2.02 and 2.04 (p.2) up to $\alpha = 10.0$ deg. Pitch-down images in Figures 2.62 and 2.64 (p.3) from a maximum angle of 9.57 deg down to 9.07 deg, do show the strake vortex image which disappears in Figure 2.64 (p.3) at 9.26 deg.

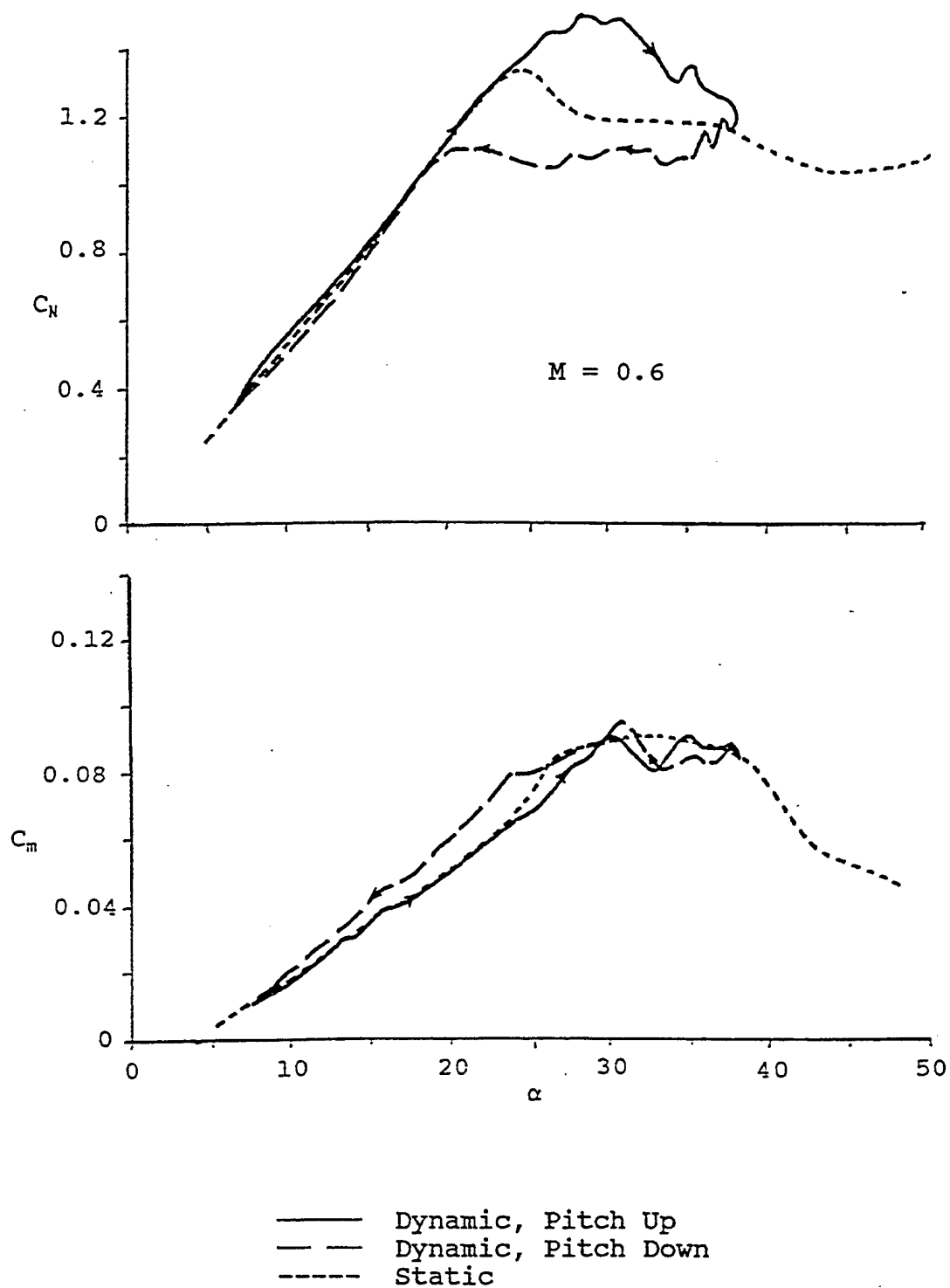


Figure 16 - Pitch Up/Push Over Maneuver Motion Between $\alpha = 7.2^\circ$ and $\alpha = 37.7^\circ$ for $M = 0.60$

These observations are a natural result of weakening of the strake vortex on pitch-up and strengthening of it on pitch-down due to model motion effects on the effective angle of attack, i.e., pitch-up produces a negative incidence on the strake and pitch-down a positive incidence. The opposite effect takes place on the main wing aft of the pitch axis. Natural lag in aerodynamic flow developments also contributes a large effect to this phenomenon. All of these effects are similar to those discussed extensively for $M = 0.225$ on the full span model in References 2 through 6.

4.2.2 Unsteady Vortex Flow for $M = 0.6$

The appropriate incidence range for vortex flow developments depends on the model motion directions. Referring to Figure 16, the maximum angle for stationary model is about 25 deg, whereas for pitch-up and pitch-down it is about 30 deg and 23 deg, respectively, as reflected in both normal force and pitching moment trends.

Comparisons between the unsteady pressure data from Part 3 during pitch-up and steady data from Part 2 for vortex flow development, begins at the 14 to 15 deg alpha range. At this point, vortex flows are well-developed and, according to the force and moment results in Figure 16, should be very similar. A comparison of the pressure data in Figure 2.11 (p.3) for unsteady flow and steady data in Figure 2.07(p.2) shows this to be the case where the distributions are quite similar at the nominal angles of 14 deg and 15 deg. A similar correlation is also seen at higher angles at about 19.5 deg to 21 deg in Figure 2.15 (p.3) for dynamic pressures and in Figure 2.13(p.2) for static data. This condition exists up to 24.95 deg in Figure 2.12(p.2) just before static burst, after which the dynamic pressures reflect unburst flow up to a maximum measure angle of 28.46 deg in Figure 2.21(p.3), with burst starting at 29.81 deg also in figure 2.21(p.3).

A similar trend is seen in the flow visualization data during pitch-up starting with the 13 to 14 deg range. Direct correlations between steady and unsteady flow visualization are complicated by the generally weaker images in Part 3, as compared with those in Part 2. Nevertheless, a direct comparison of dynamic data at 12.81 deg in Figure 2.12(p.3) with static data at 13.0 deg in Figure 2.06(p.2) shows correlation; however, the weaker dynamic image looks more like the static image at 11.0 deg in Figure 2.04(p.2). A similar comparison is seen at 13.76 deg for the dynamic in Figure 2.12(p.3) and the static data at 14.0 deg in Figure 2.08(p.2). Likewise, this trend follows at higher angles for dynamic data at 19.46 deg in Figure 2.16(p.3) and 20.72 deg in Figure 2.18(p.3) and for static data at 19.0 deg in Figure 2.12(p.2) and at 20.0 deg in Figure 2.14(p.2). The highest angle prior to vortex burst is observed at 30.22 deg for dynamic data in Figure 2.24 (p.3) and 24.30 deg for static data in Figure 2.18(p.2).

Pitch-down trends in the pressure data also reflect the tendency of flow field transitions to lag where unburst dynamic vortex flow begins at a lower angle than that for static flow. Re-establishment of vortex flow occurs in the dynamic case at 20.93 deg in Figure 2.49(p.3), as compared with steady data at 24.95 deg in Figure 2.17(p.2). The dynamic transition actually began at 24.11 deg in Figure 2.57(p.3) and continued to 22.55

deg in Figure 2.49(p.3). This agrees with the point of the onset of a more nose-down pitching moment trend at about 23 deg in Figure 16. Comparisons of dynamic pressures at 19.34 and 17.80 deg in Figure 2.51(p.3) with static pressures at 18.93 and 17.94 deg in Figure 2.11(p.2) show that the strake vortex pressures are similar, but that the main wing pressures are lower. This effect is produced by both the aerodynamic lag and the surface vertical velocities fore and aft of the pitch axis. With less aft lift development, a more nose-up pitching moment trend is produced in the dynamic case, as compared with static results as shown in Figure 16 at the same angles. The trends just noted at 18 to 19 deg are continued to lower angles, as demonstrated by the dynamic pressures at 13.68 deg and 12.46 deg in Figure 2.55(p.3), as compared with static data at 13.96 deg in Figure 2.07(p.2) and 12.94 deg in Figure 2.05(p.2).

Flow visualization data indicate that vortex burst disappears on pitch-down at an angle between 24.52 deg and 23.26 deg in Figure 2.48(p.3). This is slightly below the static point between 24.3 deg and 25.5 deg in Figure 2.18(p.2). It is generally in the range of transition noted in the pressure data between 24.11 deg in Figure 2.47(p.3) and 22.55 deg in Figure 2.49(p.3) and agrees with the onset of more a nose-down pitching moment trend at 23 deg in Figure 16. A good match of flow visualization results is seen for dynamic data at 19.46 deg and 18.22 deg in Figure 2.52(p.3) and steady data at 19.0 deg and 18.0 deg in Figure 2.12(p.2) even though the dynamic image is lighter. A similar comparison is also seen at 14.78 deg and 13.76 deg for dynamic data in Figure 2.56(p.3) and for static data at 15.0 deg and 14.0 deg in Figure 2.08(p.2). Even with the weaker image for the dynamic data, the strake vortex remains visible to 9.57 deg in Figure 2.62(p.3) as compared with the lowest angle of 11.0 deg for static data in Figure 2.04(p.2).

4.2.3 Unsteady Burst Vortex Flow for $M = 0.6$

This discussion will be mostly limited to the pressure data, since no visible flow structure was seen in the flow visualization data at angles much above the vortex burst point.

Once vortex burst occurs on pitch-up as seen at 31.17 deg in the flow visualization data in Figures 2.26(p.3) and at 31.11 deg in the pressure data in Figure 2.23(p.3), the wing and strake pressures start to deteriorate and continue to do so up to the peak angle of 37.81 deg. The main wing pressures at 33.34 deg in Figure 2.25(p.3) are not much higher than those seen at the peak angle of 37.81 deg in Figure 2.33(p.3). The strake vortex pressures at Section 5 also begin deteriorating at 35.16 deg in Figure 2.27(p.3) and continue up to the peak. These observations agree with the fall-off of normal force in Figure 16 as the peak angle is approached.

On pitch-down from the peak, the low levels of pressure persist over both the main wing and the strake. This also agrees with the flat trend for normal force for pitching down from the maximum angle in Figure 16. Comparisons of pressure distributions during pitch-up and pitch-down show this effect quite well. The pitch-down

pressures at 36.22 deg and 36.80 deg in Figure 2.37(p.3) are very flat in comparison to those during pitch-up at similar angles of 36.42 deg and 37.02 deg in Figure 2.29(p.3). This is true for both the main wing and strake pressures. A similar comparison of pitch-down data at 32.35 deg in Figure 2.41(p.3) and pitch-up data at 32.28 deg in Figure 2.23(p.3) shows the same characteristics. The low levels of wing pressure persist during pitch-down to 28.58 deg in Figure 2.45(p.3) when they begin to rise at 27.13 deg in the same figure. The strake vortex pressures at Section 5 start rising at a higher angle of 31.26 deg in Figure 2.43(p.3).

5.0 STEADY AND UNSTEADY FLOWS AT $M = 0.9$ FOR THE CLEAN WING

This section presents discussions on the pressure and flow visualization data for the clean wing configuration at $M = 0.9$ and incidences up to about 36 deg for both steady and unsteady flows. The data to be discussed are the figures in Sections 2.0, 3.0, and 4.0 of Part 2 (Steady) and Section 2.0 of Part 3 (Unsteady) of this report.

5.1 Steady Aerodynamic Characteristics for $M = 0.9$

A comparison of the normal force and pitching moment curves for $M = 0.225$, 0.6, and 0.9 in Figure 4 shows that the characteristics at $M = 0.9$ are quite different, particularly at angles below about 12 deg. A further comparison of Figure 2 at $M = 0.225$ and Figure 5 at $M = 0.9$ shows that the differences are much more widespread with regard to flow field developments. Following the format used at $M = 0.6$ for steady aerodynamic characteristics in Section 4.1, the five flow regimes shown in Figure 5 will be discussed in following paragraphs. These are (1) attached transonic flow, (2) SITES and tip leading edge separation, (3) transonic vortex flow, (4) shocklets and finger vortices, and (5) turbulent separation boundary. The above names were developed in an earlier investigation based on some preliminary flow visualization data (Reference 15) and will be used in these discussions for convenience.

5.1.1 Attached Transonic Flow for $M = 0.9$

This is the simplest flow regime to discuss since it is restricted to the development of attached transonic flows with embedded multiple shocks and no significant separations. Two primary shocks are present, the forward shock which is swept, and the aft shock which is approximately parallel to the trailing edge. These characteristics are clearly seen in pressure data in Figures 4.01(p.2) and 4.03(p.2) at angles increasing from 6.45 deg to 9.38 deg. The forward shock sweep angle continually increases, and its point for crossing pressure Section 7 moves inboard from between pressure Sections 3 and 4 at 6.45 deg to between pressure Sections 1 and 2 at 9.38 deg. Trailing edge separation begins to appear in the tip pressures at Section 4 and 8.39 deg. The pressure data in Figure 4.05(p.2) at 10.39 deg represent the last data point prior to the onset of SITES at about 10.5 deg. Also shown in Figure 4.05(p.2) are the pressures after the onset of wing tip leading edge separation which occurs just below 11.0 deg. This data point will be discussed in Section 5.1.2.

Flow visualization data to be discussed are contained in Figures 4.xx, 6.xx, and 8.xx in Part 2 of this report. The video frames in Figures 4.02(p.2) and 4.04(p.2) contain data for light sheet positions 8 and 9 corresponding to pressure Sections 6 and 7, respectively. (Since the $M = 0.6$ data were presented in Figures 2.xx(p.2) for sheet position 9, the two data sets can be compared directly.) The strake vortex is increasingly visible at position 9 as the angle is increased from 7.5 deg to 9.4 deg, at which point it is

beginning to appear at position 8. Also at 9.4 deg, the “shear layer” that develops spanwise is more clearly seen as it wraps around the strake vortex. It is more visible at 10.5 deg in Figure 4.06(p.2) just prior to SITES onset.

This “shear layer” is the “gull wing” pattern referred to in Reference 19 and is occasionally seen on aircraft flying at transonic speeds in humid air for which many examples are given in Reference 19. Side view camera video frames in Figures 6.02(p.2) through 6.06(p.2) for angles increasing from 6.52 deg to 10.31 deg, respectively, provide streamwise cuts through the shear layer at sheet positions 1, 3, and 14. In agreement with Figures 4.02 through 4.06(p.2), the shear layer which starts at the wing leading edge crank at position 14, is closer to, as well as more diffused at the outboard position 3. A suggestion is posed that this shear layer represents the interface between (1) the outer flows which see the spanwise flow potential propagating from the inboard strake region, and (2) the inner supersonic flows near the wing surface. The justification for referring to this as a shear layer is the way that it wraps around the strake vortex which also implies that its vorticity is the same sign as that of the strake vortex. Since the shear layer starts on the wing leading edge at the 76 deg/40 deg crank, further justification is given for this being a true shear layer whose vorticity is in the same direction as the strake vortex.

The side views also show the aft shock quite clearly, which in agreement with pressure data, does not move significantly with increasing angle up to 10.31 deg at both sheet positions. Pulsed laser recordings at sheet position 3 are shown in Figures 8.01(p.2) at 6.0 deg, 8.02(p.2) at 8.0 deg, and 8.03 at 10.0 deg where each provides more detail than is seen in the side camera frames at position 3 in Figures 6.02 through 6.06(p.2). The shock is more clearly shown at 8.0 deg; and at 10.0 deg, a “lamda” shock with a thin boundary layer separation within the legs of the lamda is also seen. This condition at 10.0 deg is the precursor to SITES onset in Figure 8.04(p.2).

Turning to sheet position 14 in Figures 6.01 through 6.06(p.2), development of the strake vortex is seen. This sheet position, as shown in Figure 10, is angled so that it always cuts through the strake vortex core no matter what the angle is. Vortex development is first apparent at 8.56 deg in Figure 6.04(p.2) where the aft shock is also visible at about the same chordwise position as it is seen at sheet position 1 (in reference to the side wall “targets”). A core is visible at 9.49 deg in Figure 6.05(p.2), and the aft shock is a little more defined. At 10.41 deg in Figure 6.06(p.2), both the vortex core and the aft shock are clearly visible.

5.1.2 SITES and Tip Leading Edge Separation for $M = 0.9$

The pressure data shown in Figure 4.05(p.2) at 10.39 deg and 11.39 deg imply that a single, very catastrophic flow transition occurs between these two angles on the outboard wing. The same is true for the flow visualization data in Figure 4.06(p.2) at 10.5 deg and 11.6 deg. This is not the case and, in actuality, two distinct flow transitions

occur which are (1) SITES at just below 10.5 deg, and (2) wing tip leading edge separation at just below 11.0 deg.

This side view camera data in Figures 6.06 through 6.10(p.2) cover the angle range of 10.31 deg to 11.75 deg which is the same as that in Figures 4.05 and 4.06(p.2) of 10.39 deg to 11.6 deg. The height of the shear layer at sheet position 1 increases up to 11.03 deg in Figure 6.09(p.2) and decreases at 11.75 deg in Figure 6.10(p.2). Sheet position 3 shows the onset of SITES at 10.67 deg in Figure 6.07(p.2) and wing tip leading edge separation at 10.86 deg in Figure 6.08(p.2).

The weak side view camera images at position 3 are augmented by the enhanced pulsed laser recordings at position 3 for the angles of 10.0, 10.5, and 11.0 deg in Figures 8.03 through 8.08(p.2). Multiple recordings were made at angles 10.5 deg and 11.0 deg in order to emphasize the unsteadiness of the flows at those angles. The data in Figure 8.03(p.2) at 10.0 deg shows the development of the lamda shock structure and the thin shock-induced boundary layer separation within the lamda region. The multiple frames at 10.5 deg in Figures 8.04, 8.05, and 8.06(p.2) show the structure of SITES to extend much farther above the wing than had been previously thought. The heights of these excursions in the figures are on the order of 15% to 20% of the chord length. It is also of interest to note that the shock moves considerably forward with the onset of SITES at 10.5 deg as compared to 10.0 deg.

The character of wing tip leading edge separation at 11.0 deg just after transition is captured in Figures 8.07 and 8.08(p.2). The turbulent shear layer is close to the wing and not much higher than the turbulent structures observed for SITES in Figures 8.04, 8.05, and 8.06(p.2). The white regions above the turbulent shear layer indicate that this flow is still accelerated to supersonic speeds as was observed forward of the aft shock in Figures 8.02 and 8.03(p.2). The structure of the turbulent shear layer in Figures 8.07 and 8.08(p.2) appears to be composed of small vortical structures and larger structures that have a wave length of about 25% of the local wing chord.

Returning to the flow visualization data in Figure 4.06(p.2) at 11.6 deg, it is easier to understand the flow structure indicated by the deterioration and distortion of the shear layer at sheet position 9. Also, it is now understandable as to why no indication of these transitions is seen at sheet position 8 in the same figure. The structure outboard of pressure Section 1 at sheet position 9 is extremely unsteady as can be seen in the IHSV tape or the edited VHS tape that were both discussed in Section 3.0. It is also the structure that will persist up to about 18 deg or 19 deg in the transonic vortex flow regime to be discussed below.

5.1.3 Transonic Vortex Flow for $M = 0.9$

In this flow regime, remnants of transonic flow with the forward shock present exist at pressure Section 1 at 12.39 deg and 13.41 deg in Figure 4.07(p.2). The forward shock moves inboard of this position to 14.42 deg in Figure 4.09(p.2). The peak in pressure in Section 6 near its intersection with pressure Section 1 starts increasing for angles higher than 14.42 deg as is shown in Figure 4.09(p.2) at 15.46 deg. This peak continues to grow up to 18.45 deg in Figure 4.13(p.2) where it levels off at 19.45 deg and begins falling at 20.44 deg in Figure 4.14(p.2). A bump in the spanwise pressures in Section 7 centered on the intersection with pressure Section 1 is also seen to develop from 13.41 deg in Figure 4.07(p.2) to angles beyond 19.45 deg in Figure 4.13(p.2).

This bump in Section 7 and the large peak in pressure Section 6 just discussed bear a strong resemblance to similar characteristics at $M = 0.6$ over the same incidence range. Since these characteristics at $M = 0.6$ were indicative of the wing vortex which starts at the leading edge crank, it is suspected that the same holds true for the $M = 0.9$ case. The transonic wing vortex should be quite different from that at $M = 0.6$ because of the presence of the forward shock, which probably follows along the same path.

Flow visualization data corresponding to the pressure data discussed above and given in Figures 4.08, 4.10, and 4.12(p.2) which cover the angles 12.39 deg to 17.44 deg. These data at sheet positions 8 and 9 show a fairly consistent development of a pattern that contains three basic elements: (1) the strake vortex (positions 8 and 9), (2) a strong shear layer that wraps around the strake vortex (position 9), and (3) outboard wing separation with an "s"-shaped transition in the shear layer at about pressure Section 1 (inboard chordwise row). The strake vortex image development is simply an extension of that seen at the lower angles, and the shear layer becomes stronger with increasing angle but does not change its character. Nothing is seen of the outboard separation development in Figures 4.08 through 4.12(p.2), but the s-transition at pressure Section 1 becomes more sharply defined at the higher angles up to 17.6 deg in Figure 4.12(p.2). The s-shape of this transition has all of the appearances of some type of vortical/shock interaction, but this has not been verified with data from this test.

The side view camera frames at sheet positions 1 and 3 for the corresponding conditions discussed above are shown in Figures 6.11 through 6.16(p.2). Very little information is available at position 3, but shear layer development at position 1 is seen as changing both in position (increasing height with increasing angle) and in character where it splits into two layers at 13.53 deg in Figure 6.12(p.2). Since sheet position 1 also corresponds to the location of this s-transition at pressure Section, the chordwise character of this phenomenon should be discernible. The point of splitting at 13.53 deg in Figure 6.12(p.2) is about the same as 13.5 deg in Figure 4.08(p.2) where the s-transition becomes much better defined with a steeper spanwise slope. The double shear layer, as is more clearly seen in Figure 6.15(p.2) at 16.62 deg, shows that the lower layer appears to emanate from near the wing leading edge at sheet position 1. The upper layer tends to

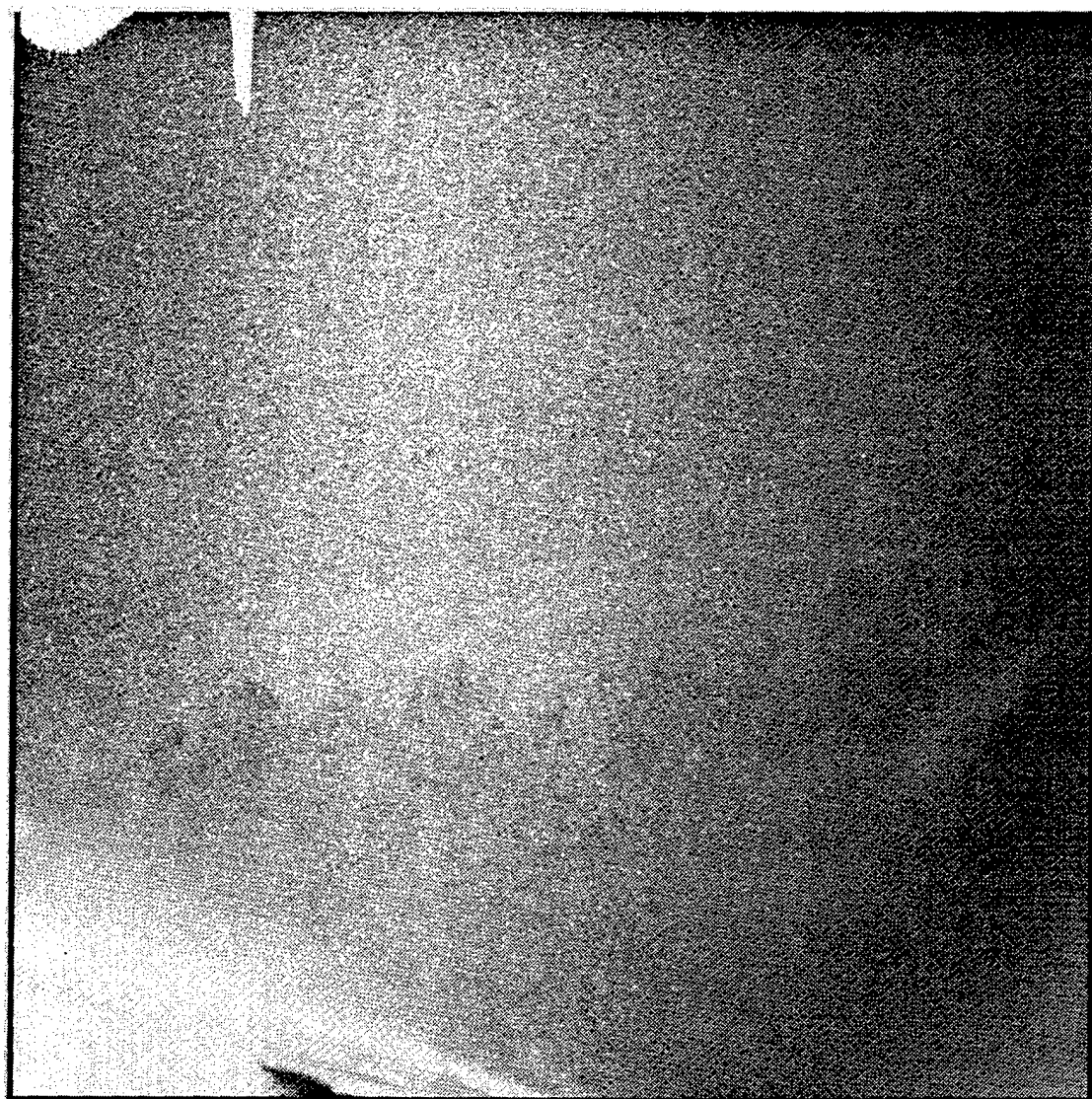
line up with the upper boundary of the strake vortex image at sheet position 14 also in Figure 6.15(p.2). The same trends can be seen at other angles below 18 deg.

Since the double shear layer image disappears at about the center of the middle "targets" in the sidewall turntable, this implies that the s-transition is not necessarily oriented streamwise, but could be emanating from the leading edge crank. This latter postulation is more consistent with the possibility of a combination of forward shock and wing vortex existing in this region. Such a flow structure would also help explain why not much activity is seen at the sheet position 8 where the wing vortex would be very close to the wing and therefore very difficult to detect with the vapor screen technique.

There is no difficulty in seeing the strake vortex developments at sheet position 14 in Figures 6.11 through 6.16(p.2). The core is clearly visible up to 14.67 deg in Figure 6.13(p.2) where the aft shock becomes another dominant feature in the images. Further developments up to 17.51 deg in Figure 6.16(p.2) show growth of the core and stronger interactions with the aft shock, both in the upper outer shear layer and the lower layer near the wing surface. The location of this shock in this sequence of frames is just aft of pressure Section 7 (and sheet position 9).

The leading edge separation outboard of the s-transition is very well identified with the pulsed laser recording frames at position 3 in Figures 8.09 and 8.10(P.2) at 12.0 deg, Figures 8.11, 8.12, and 8.13(p.2) at 17.0 deg, and Figures 8.14 and 8.15(p.2) at 18.0 deg. The frames at 12.0 deg look similar to those at 11.0 deg in Figures 8.07 and 8.08(p.2) but more developed and much more unsteady, as illustrated by the differences in Figures 8.09 and 8.10(p.2). At 17.0 deg, in Figures 8.11, 8.12, and 8.13(p.2), the separation surface has developed a smooth structure above the band of smaller vortices that is seen in all three frames. This same structure is also shown at 18.0 deg in Figure 8.14(p.2), but a very different structure is seen in Figure 8.15(p.2) which indicates that a transition is about to take place.

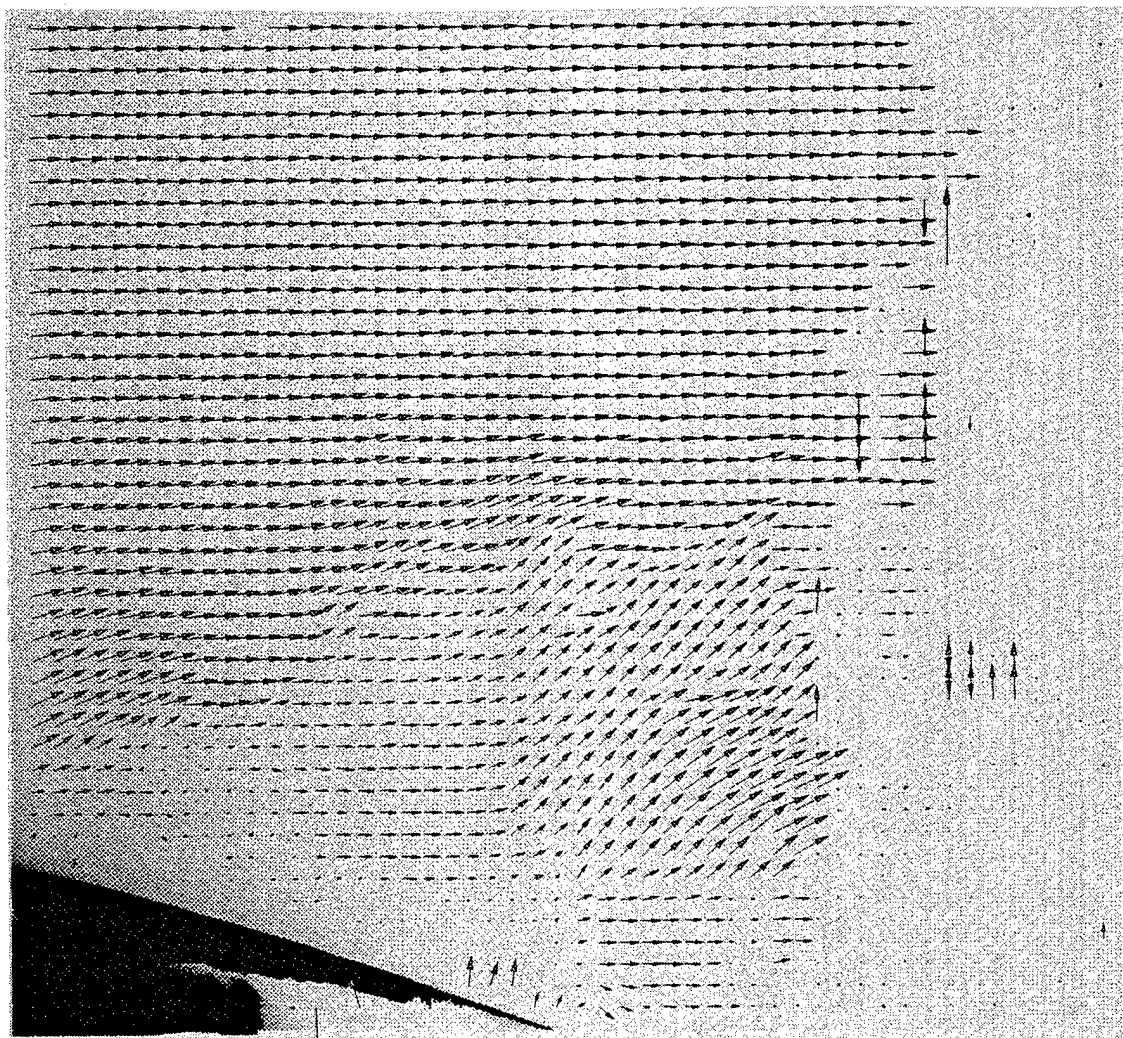
Limited quantitative data using particle image velocimetry (PIV, Reference 18) were obtained on the clean wing configuration at $M = 0.225$ and 0.6. An example of PIV data is shown in Figure 17 for $M = 0.225$ at 20 deg incidence which contains a double exposure of two pulsed laser images separated by 1.5 micro-sec. Processed data into velocity field vector plots are shown in Figures 18 and 19 at $M = 0.225$ and 0.6, respectively. Two sets are shown in Figure 18 at 20 deg and $M = 0.225$ to illustrate the typical unsteadiness of leading edge separated flows. Results at $M = 0.6$ and 16 deg shown in Figure 19 have a similar appearance. In both cases, the vortical structure along the boundary of the separation, as well as that within the separation, is shown where the characteristic wave lengths are on the order of about 15% to 20% of the local chord. This structure is similar to that observed in many of the pulsed laser flow visualization frames in Figures 8.07 through 8.15(p.2).



Leading Edge

Trailing Edge

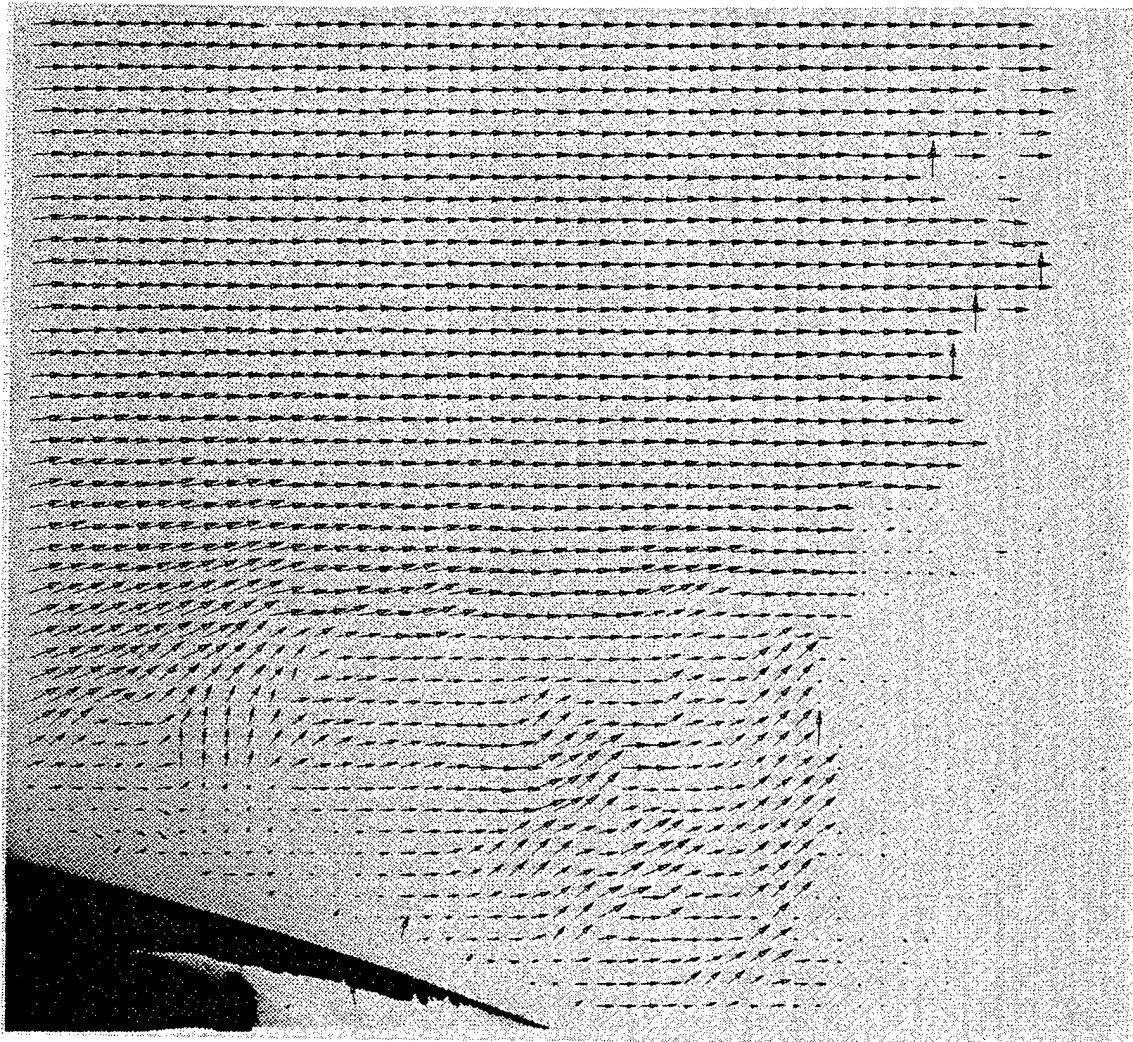
Figure 17 - PIV Data Frame for $M = 0.225$ at 20 deg (Reference 18)



Leading Edge

Trailing Edge

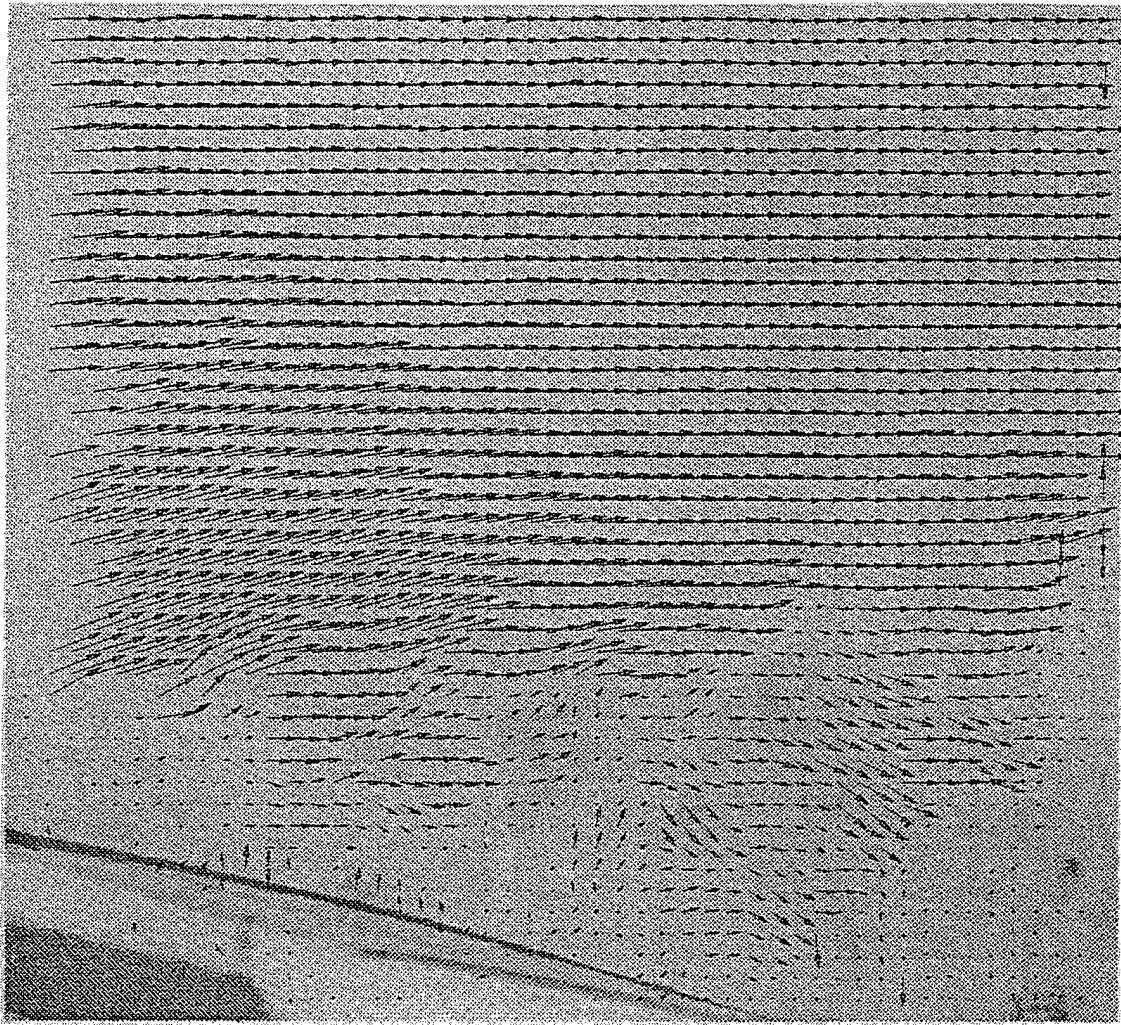
Figure 18 - PIV Calculations for $M = 0.225$ at 20 deg (a) First Example



Leading Edge

Trailing Edge

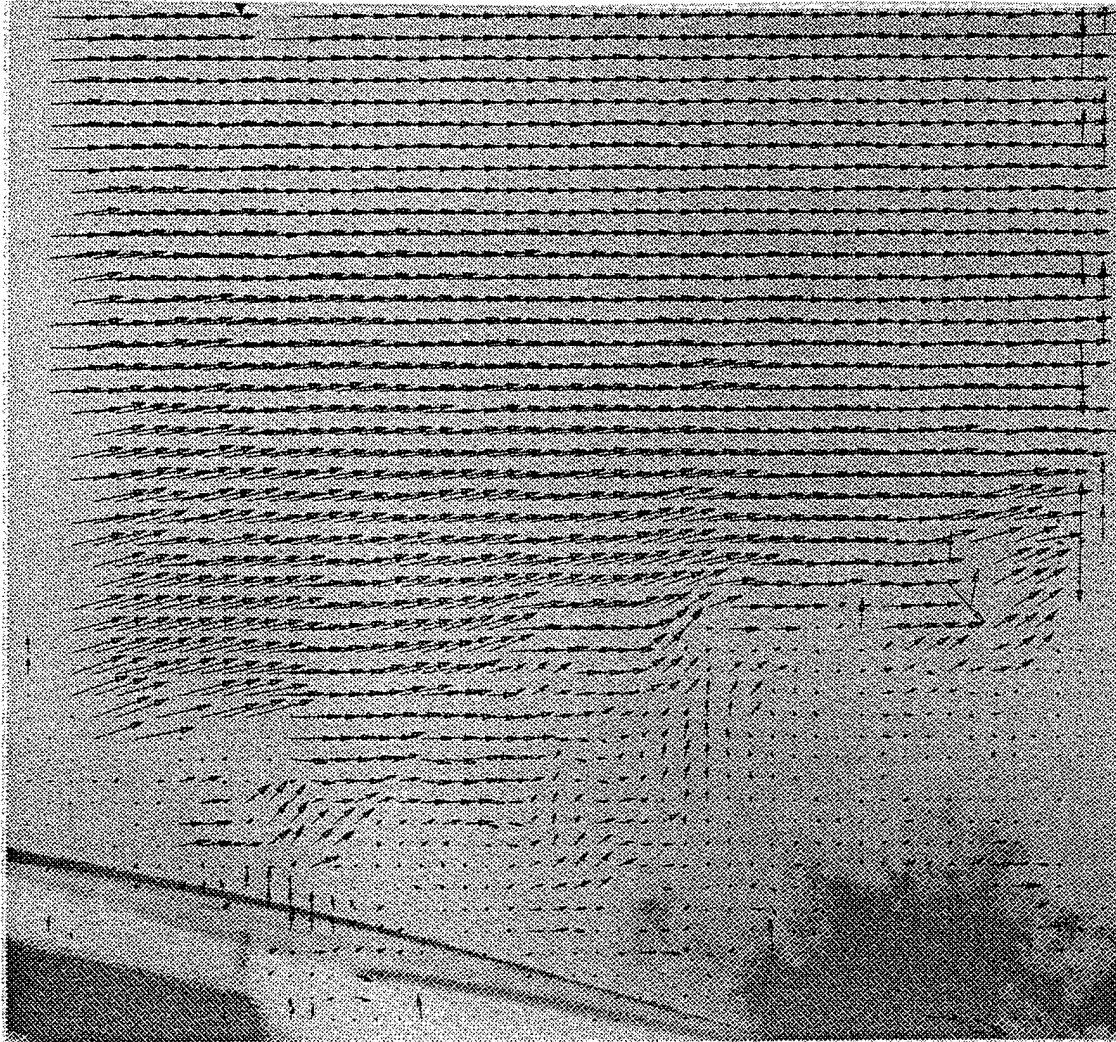
Figure 18 - (b) Second Example



Leading Edge

Trailing Edge

Figure 19 - PIV Calculations for $M = 0.6$ at 16 deg (a) First Example



Leading Edge

Trailing Edge

Figure 19 - (b) Second Example

5.1.4 Shocklets and Finger Vortex Structure for $M = 0.9$

At angles above 18.45 deg, the pressure data show a continuous deterioration of the wing vortex signature at pressure Section 6. The growth of the corresponding pressure peak at this section for angles up to 18.45 deg stops at 19.45 deg is seen in Figure 4.13(p.2). This growth is reversed until the peak disappears by about 25.43 deg in Figure 4.19(p.2). Wing pressures overall, however, experience a slow, steady growth with exception of the wing vortex region. The strake vortex also grows in strength, as indicated by the pressures at Section 5 in the Figures 4.13 through 4.25(p.2). These observations are in agreement with the normal force and moment trends seen in Figure 5 where peak normal force occurs at about 25 deg, and pitching moment is increasingly more nose-up until 27 deg to 28 deg where it levels off.

The corresponding flow visualization data are shown in Figures 4.14 through 4.20(p.2) for sheet positions 8 and 9. The beginning of this transition is seen in Figure 4.14(p.2) at 18.45 deg where multiples of the s-transition structure appear at sheet position 9 in the region outboard of pressure Section 1 as the shear layer alters its shape dramatically. The strake vortex signature does not change much until about 23.4 deg in Figure 4.18(p.2) where it begins to widen significantly.

The most notable features in this flow regime are the multiple s-transitions with extensions into the upper flows that appear to be shocks. It was postulated that these flow features were composed of multiple vortical structures emanating from the leading edge which led to the term, "finger vertices". Each set of those finger vortices had an apparent shock associated with it, which likewise led to the term, "shocklets". The best views of the shocklet and finger vortex structures are shown in Figure 4.16(p.2) at both angles of 20.5 deg and 21.6 deg. In these examples, two sets are seen where the inboard set corresponds approximately to pressures Section 2 and the outboard set to Section 3.

Another interesting observation in Figures 4.14 through 4.20(p.2) is the development of the strake vortex image at sheet position 8. This observation centers on the abrupt termination of the shear layer wrapping around the strake vortex. Following the layer from the vortex core in a counterclockwise direction in Figure 4.16(p.2) at 20.6 deg, the layer stops outboard and above the core with a shape that looks similar to the s-transition discussed earlier at sheet position 9 (see Figure 4.10[p.2] at 14.6 deg). Although the image is not as strong at sheet position 8, it is repeatable and appears at the angles consistent with breakdown of the wing vortex seen in the pressure data over the incidence range of 19.45 deg through about 24.45 or 25.43 deg. This observation lends more credibility to the postulation presented in Section 5.1.3 that the forward shock and the wing vortex are combined into a single flow phenomenon.

The side view camera frames for this flow regime are very interesting also and provide streamwise cuts through the structures discussed based on the spanwise sheet positions. Sheet position 4 at the wing tip shows a definite development of a vortex looking streak that emanates from the wing leading edge. It is very faint at 18.46 deg in

Figure 6.17(p.2) and becomes much more visible at 25.67 deg in Figure 6.24(p.2). As wing incidence increases, this flow feature also shows a corresponding increasing angle of separation above the wing. Sheet position 1 shows that the double shear layer structure at 18.50 deg in Figure 6.17(p.2) changes to a more diffuse structure and increasing height above the wing as the angle is increased up to 25.57 deg in Figure 6.24(p.2). This is in agreement with the spanwise developments of the shear layer seen in Figures 4.14 through 4.20(p.2).

Another new structure shown at sheet position 1 near the wing surface moves forward from the trailing edge of the wing starting at 21.67 deg in Figure 6.20(p.2). It also appears at sheet position 3 at 25.67 deg in Figure 6.24(p.2). Motion of this structure as seen in the video tapes is very unsteady and appears to be associated with breakdown in the strake vortex.

Sheet position 14 shows the strake vortex development up to 25.56 deg in Figure 6.24(p.2). Progression of vortex growth and shock development in the range of 19.53 deg in Figure 6.18(p.2) to 25.56 deg, are consistent and steady with no apparent strong transitions. The shock-induced separation of a layer near the wing that was discussed previously in Section 5.1.3 does not move until the angle reaches 23.55 deg in Figure 6.22(p.2) where it starts moving forward. At 24.45 deg in Figure 6.23(p.2), it has moved forward enough to be in view of spanwise sheet position 9. Referring to Figure 4.18(p.2) at 23.4 deg and Figure 4.20(p.2) at 24.3 deg and 25.4 deg, a distinct change is seen in the portion of the shear layer that is below the strake vortex near the wing. It is also shown by the pressure data in Figure 4.19(p.2) at 25.43 that a significant drop occurs in the pressures at Section 7 corresponding to the strake vortex location. Thus, it appears that the maximum normal force seen in Figure 5 occurs at about the time this shock-induced separation begins to move rapidly forward.

The sweeping sheet frames also shown in Figures 6.18 through 6.24(p.2) provide data that tie together the characteristics discussed above for sheet positions 1, 3, 8, 9, and 14. This sweep shows that the finger vortex/shocklet/shear layer structure is continuous from the wing leading edge. It also shows that the strake vortex is the primary flow feature over this angle range, and that it is well formed over the wing.

The pulsed laser recordings at sheet position 3 and 19.0 deg are shown in Figures 8.16, 8.17, and 8.18(p.2) to emphasize the transitional nature of this condition. This is in agreement with the above discussions with regard to the angles around 18 to 19 deg. Figure 8.17(P.2) appears similar to Figure 8.14 at 18 deg, whereas Figure 8.18(p.2) looks more like Figure 8.19(p.2) at 22.0 deg. Figure 8.18(2) also shows what looks like shocks in the flow above the vortical structures in the separation region. This could be the "shocklet" referred to earlier in this subsection. At 22.0 deg, Figures 8.19, 8.20, and 8.21(p.2) show a very "stable" separated flow which does appear to be composed of multiple "finger vortices" above which is a supersonic region which must terminate in a shock at some point. Since sheet position 3 is close to the outer finger vortex/shocklet structure seen in Figure 4.16(p.2) at 21.6 deg, Figures 8.19, 8.20, and 8.21(p.2)

apparently provide a detailed view of that phenomenon and verify both its character and relative stability as was noted earlier.

5.1.5 Turbulent Separation Boundary for $M = 0.9$

Above angles of 25.43 deg, the pressure data show that the wing tip is stalled and remains so, as evidenced by the pressures at row 4 in Figures 4.21(p.2) through 4.27(p.2). A continuous breaking down of pressures at the inboard rows 2 and 3 in this sequence of figures is indicative of progressive stalling of the outboard wing panel. Accompanying this breakdown, is a rising peak in the pressure row 6 distribution which corresponds to a "new" wing vortex. The crossing of this wing vortex at the forward part of pressure row 1 is also seen at angles up to 30.46 deg in Figure 4.25(p.2) where, by the next angle of 32.40 deg, this growth process has broken down. The small peak in normal force in figures at 32 deg also corresponds to this angle of 32.40 deg. By 36.39 deg in Figure 4.27(p.2), the wing aft of the leading edge crank is almost fully stalled. The strake vortex pressure peak continues to grow until it reaches a maximum at 30.46 deg and 32.40 deg in Figure 4.25(p.2), after which it deteriorates in Figure 4.27(p.2) at 34.42 deg and further at 36.39 deg.

The flow visualization data in Figures 4.22 and 4.24(p.2) for sheet positions 8 and 9 show a continuous breakdown of the strake vortex at position 9. At 29.4 deg in Figure 4.24(p.2), the strake vortex breakdown reaches sheet position 8, and the image at sheet position 9 takes on a new character which is seen to evolve at the previous angles of 26.4 deg, 27.7 deg, and 28.4 deg. This structure remains dominant until 34.0 deg in Figure 4.28(p.2) at sheet position 9 where it becomes less distinct and picks up a weak outboard extension that is also seen at 36.0 deg. The image at sheet position 8 shows a continuous change up to 34.0 deg in Figure 4.28(p.2) where at 36.0 deg, it becomes very diffuse as is consistent with the weak vortex signature in the pressures at row 6 for 36.39 deg in Figure 4.27(p.2).

Images at sheet position 9 in Figures 4.22(p.2) through 4.28(p.2) are indicative of very turbulent, full span leading edge separation which is bounded by a likewise very turbulent shear layer. This observation was the basis in Reference 15 for referring to this flow regime as "turbulent separation boundary". The shape of this boundary is defined by the wing tip and leading edge up to the strake wing crank where transition into this strake vortex structure occurs. This intersection of two different flow fields is probably the source of the link seen in the sheet position 9 image in Figure 4.24(p.2) at 29.2 deg. There is a strong similarity between this kink and the "s-transition" structure discussed for transonic vortex flow in Section 5.1.3 (see Figure 4.12([p.2], for example). There is also a continuity seen between the images at sheet positions 8 and 9 in Figures 4.24 and 4.26(p.2) for 29.2 deg, 30.4 deg, and 32.3 deg where the dark upper region at position 8 appears to be a forward extension of the dark upper region at position 9. These two images, in turn, tend to line up with the wing leading edge crank.

Side view images in Figure 6.25(p.2) at sheet position 14 shows that the strake vortex structure at 26.48 deg is similar to that at 25.56 deg in Figure 6.24(p.2). This structure changes at 27.61 deg in Figure 6.26(p.2) and remains the same to the highest angle of 34.61 deg in Figure 6.31(p.2). This structure is the single outer shear layer wrapping around the burst strake vortex, as shown in Figures 4.22 through 4.28(p.2).

Returning to the “new” wing vortex observed in the pressure data between 26.43 deg and 34.42 deg, the flow visualization structure that is associated with its position appears to be the outboard end of the strake vortex shear layer next to the wing. This is seen as a bump in Figure 4.22(p.2) at sheet position 9 and 26.4 deg near pressure row 1 which has almost disappeared at 27.7 deg in the same figure. A similar structure is seen in the same figure at about mid-span of sheet position 8 where the outer shear layer next to the strake vortex is leaving the wing surface. The structure seen in Figures 6.24 through 6.27(p.2) at sheet positions 1 and 3 which is next to the wing and moving forward from the trailing edge is also believed to be the same phenomenon. This is based on the comparison of the images in Figure 4.22(p.2) at 26.4 deg, sheet position 9, and in Figure 6.25(p.2) at 26.46 deg, sheet position 1, where the two sheets cross. This crossing occurs just inboard of the row of three targets (pressure row 1) in Figure 4.22(p.2) and between the last two of the three targets in Figure 6.25(p.2). Thus, the structure near the wing at the trailing edge for sheet position 3 in Figure 6.25(p.2) is also part of that seen in Figure 4.22(p.2) at sheet position 9 (since it was shown in Section 5.1.4 to be the same as that at sheet position 1 in Figure 6.25[p.2]). These structures at positions 1, 3, 8, and 9 all lineup with the leading edge crank at 26.4 deg as well as other angles. It is suspected that the associations’ common flow phenomenon is an extension of the reverse circulation secondary vortex that exists on the strake as it passes over the wing.

5.2 Unsteady Aerodynamic Characteristics for $M = 0.9$

This section addresses the effects of model pitching motion on the flow fields discussed above in Section 5.1. Emphasis will be placed on the differences observed between pitching-up and pitching-down motions, as well as how they relate to conditions for the stationary model at similar angles. References will be made to the figures in Section 2.0 of both Part 2 and Part 3. The five flow regimes to be discussed will be (1) attached transonic flow, (2) SITES and tip leading edge separation, (3) transonic vortex flow, (4) shocklets and finger vortices, and (5) turbulent separation boundary. These discussions follow the same sequence used in Section 5.1 for stationary model conditions.

5.2.1 Attached Unsteady Transonic Flow for $M = 0.9$

The variation of wing normal force, C_N , and pitching moment, C_m , are shown in Figure 20 at $M = 0.9$ for the model at static conditions and pitch-up, pitch-down for a (1-cos) motion at 3.8 Hz. (This is a $M = 0.9$ version of Figure 16 at $M = 0.6$). With this type of motion, the wing starts from rest at 7.2 deg, reaches maximum incidence of 37.7

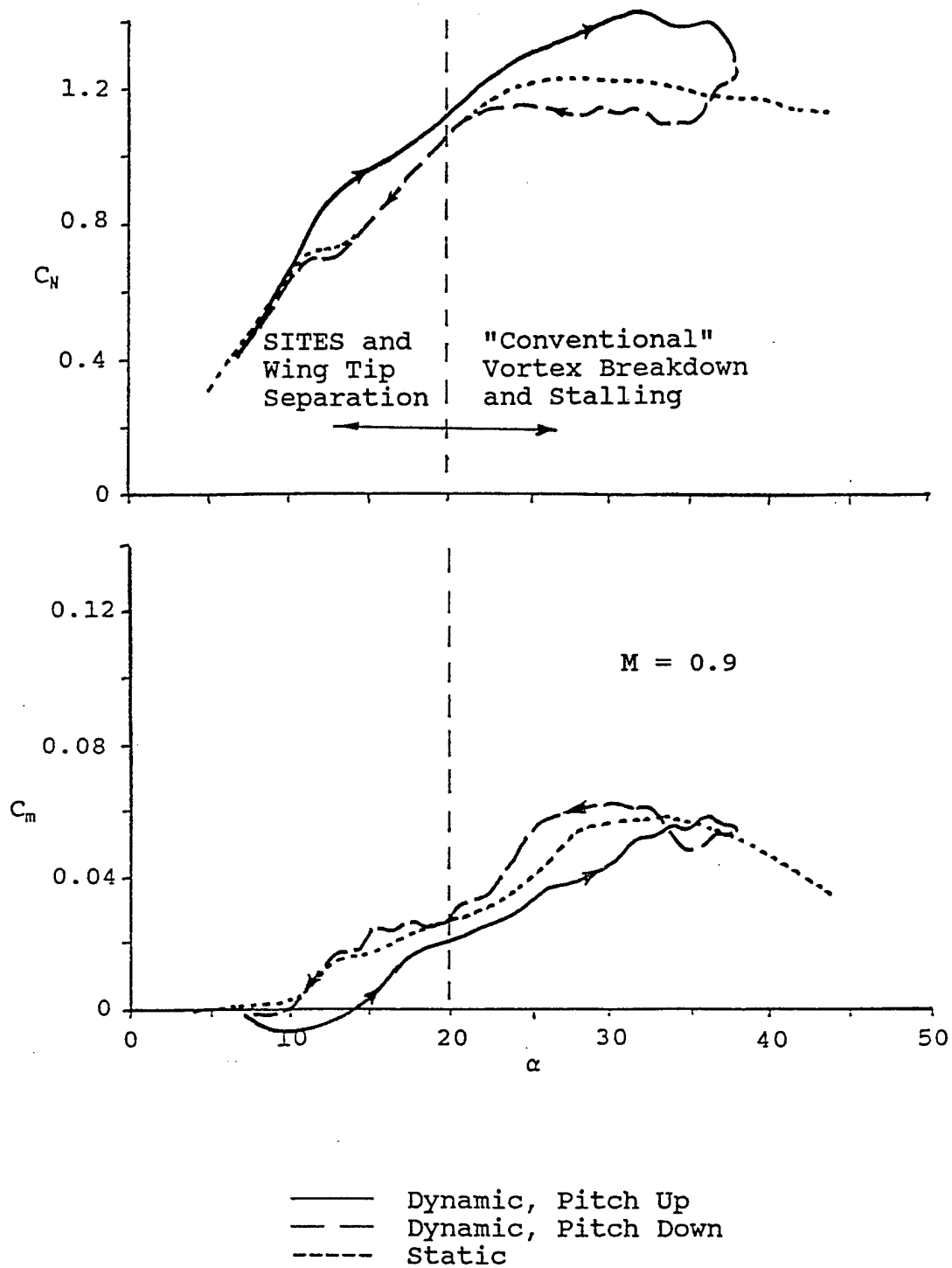


Figure 20 - Pitch Up/Push Over Maneuver Motion Between $\alpha = 7$ deg and $\alpha = 37$ deg for $M = 0.90$

deg and returns to rest at 7.2 deg where the motion is described by a $(1 - \cos \omega t)$ wave form. The attached flow regime seems to be extended up to about 12 deg in pitch-up for both normal force and pitching moment. The pitch-down trends appear to be no different than the static curve for normal force and pitching moment.

The dynamic effects seen in Figure 20 at $M = 0.9$, as compared to those in Figure 16 at $M = 0.6$, are much less pronounced because with a constant frequency of 3.8 Hz but a higher velocity, the non-dimensional pitch rate is proportionately smaller by the ratio of $0.6/0.9$, as discussed in Reference 9.

The pressure data for pitch-up are shown in Figures 4.01 through 4.09(p.3) and correspond to the steady data in Figures 4.03 through 4.05(p.2). Pressures at 7.39 deg in Figure 4.01(p.3) on pitch-up approximately match those at a steady 7.45 deg in Figure 4.01(p.2). At 9.24 deg, the dynamic pressures on pitch-up in Figure 4.05(p.3) have about the same lift on the outboard pressure rows, but they are more aft-developed when compared with the steady data at 9.38 deg in Figure 4.03(p.2). At higher angles in the overshoot region for the pitch-up data, pressures at 12.71 deg in Figure 4.09(p.3) are very similar to those at a steady 10.39 deg in Figure 4.05(p.2). The differences are mostly in the distribution where the dynamic data show a more aft lift consistent with the nose-down pitching moment seen in Figure 26 at about 13 deg.

The pitch-down pressure data for attached transonic flow are shown in Figures 4.59 through 4.65(p.2). Pressure distribution features at steady 10.39 deg in Figure 4.05(p.2) are not completely reproduced in the unsteady pitch-down distributions, but those seen at 9.41 deg and 8.71 deg in Figure 4.59(p.3) come very close where the former shows a rise in leading edge suction as the latter shows the aft sweeping of the forward shock. A comparison of the unsteady pitch-down data in Figure 4.63(p.3) at 7.36 deg with that at a steady 7.45 deg in Figure 4.01(p.2) shows a reasonable match.

Flow visualization data for pitch-up from 9.01 deg in Figure 4.02(p.3) to 12.81 deg in Figure 4.10(p.3) show a continuous development of the shear layer and an increasingly prominent strake vortex. This is in agreement with the pressure data discussed above. Pitch-down flow visualization data in Figures 4.58 through 4.64(p.3) show that outboard leading edge separation persists down to about 10.00 deg or 9.47 deg in Figure 4.62(p.3). This is also in agreement with the discussions above on pressure data comparisons.

5.2.2 Unsteady SITES and Leading Edge Flows for $M = 0.9$

On pitch-up, the variations of normal force and pitching moment in Figure 20 indicate that this transitional region is more diffuse and begins at about 12 to 13 deg. The corresponding trends on pitch-down show the transition to be very similar to that for steady model data, both in sharpness and location.

The pressure data for pitch-up in Figure 4.11(p.3) show that SITES probably didn't exist as that leading edge separation in the outer pressure rows has appeared by 13.87 deg. There is no comparable distribution in the steady flow data.

For pitch-down, re-attachment of the tip leading edge flow doesn't appear until 9.41 deg in Figure 4.59(p.3). SITES appears at 8.41 deg in the same figure, but has disappeared by 8.09 deg in Figure 4.61(p.3).

The dynamic effects seen in the pressure data discussed above for this transitional flow seem to be more confined to the wing tip region. The flow visualization data for pitch-up shown in Figures 4.10 and 4.12(p.3) at 13.76 deg and 14.78 deg, respectively, indicate that the leading edge flow separation is more outboard as seen in the pressure data. This is in comparison with data for steady flow in Figure 4.06(p.2) at 11.6 deg. The same trend is seen for pitch-down at 11.96 deg in Figure 4.58(p.2).

5.2.3 Unsteady Transonic Vortex Flow for $M = 0.9$

Normal force variations on pitch-up in Figure 20 up to about 20 deg have a higher level than those for the static data. Pitching moment is less nose-up than the static data indicating that the additional lift is aft. On pitch-down, no difference is seen in the normal force trends compared to static data and pitching moment is only slightly more nose-up.

The pressure data for vortex flow development during pitch-up are shown in Figure 4.11(p.3) starting at 13.87 and Figure 4.13(p.3) at 17.85 deg. The unsteady data are quite ragged in the distributions when compared with steady data in the corresponding Figures 4.07 through 4.11(p.2). Also, a sharp drop and rise is seen in the spanwise distributions at row 7 and chordwise distributions at row 1 for 16.40 deg and 17.85 deg in Figure 4.13(p.3). Generally higher levels of pressure exist overall which are located more aft when compared with the static pressure data. This correlates with the trends seen in Figure 20.

Starting at 17.67 deg in Figure 4.51(p.30), the pressure distributions for pitch-down show generally a very good agreement with the steady data down to 12.31 deg in Figure 4.55(p.3), as compared with the 12.39 deg steady data in Figure 4.07(p.2).

Flow visualization data during pitch-up for transonic vortex flow are shown in Figure 4.10(p.3) at 13.76 deg through Figure 4.14(p.3) at 18.22 deg. Comparing with steady data in Figure 4.06(p.2) at 11.6 deg through Figure 4.12(p.2) at 17.8 deg, the images are virtually identical if the unsteady data are displaced about 1 deg higher. For example, steady data at 15.5 deg in Figure 4.10(p.2) are very close to the unsteady data at 17.02 deg in Figure 4.14(p.3). The dynamic angle for transition to shocklet/finger vortex flow is also about 1 deg higher at 19.46 deg on Figure 4.16(p.3), as compared with the transition at 18.5 deg in Figure 4.14(p.2).

The pitch-down effects on unsteady flow visualization are shown in Figure 4.54(p.3) at 17.02 deg through Figure 4.56(p.3) at 13.76 deg for transonic vortex flow with remnants shown in Figure 4.58(p.3) at both angles of 12.83 deg and 11.96 deg. In all cases, the shock above the s-transition in the shear layer is much more pronounced than for the steady or unsteady pitch-up images. The unsteady images don't appear to be displaced from the steady images to a lower angle, as might be expected. The onset of shocklet/finger vortex flow in steady flow at 18.5 deg compares well with the last image on pitch-down at 18.22 deg in Figure 4.52(p.3), both in terms of angle and image. Overall, the image structure in Figures 4.54 and 4.56(p.3) is smaller than that at comparable steady conditions.

The dip noted above at 16.40 deg and 17.85 deg in the unsteady spanwise pressure distributions are also accompanied by a "bump" just outboard which is more pronounced at lower angles of 12.71 deg in Figure 4.09(p.3), as well as 13.87 deg and 15.04 deg in Figure 4.11(p.3). This "bump" appears to coincide with the inner part of the s-transition in the unsteady flow visualization image. A comparison of the spanwise pressure distribution at row 7 in Figure 4.11(p.3) at 15.04 deg with the image at 14.78 deg in Figure 4.12(p.3) demonstrates this correlation. The alignment of the "bump" at row 7 also lines up with a corresponding bump at rows 1 and 6 which were attributed to the wing vortex in Section 5.1.3. Thus, it is quite possible that the "bump" is actually the signature of the wing vortex which under dynamic pitch-up conditions remains close to the wing. On pitch-down, the structure of this vortex appears to be the same as for steady data, based on the pressure data.

Another observation on the flow visualization data and pitch-up is that the strake vortex is closer to the wing which would explain the higher pressure levels seen at row 7 that correspond to the strake vortex.

5.2.4 Unsteady Shocklets and Finger Vortex Structure for $M = 0.9$

The pitch-up trend for normal force above 20 deg, shown in Figure 20, continues that begun in the vortex flow phase just discussed. The maximum normal force is achieved at above 32 deg. Pitching moment also continues the trend of being less nose-up than the static data, but is driving toward that curve. On pitch-down, the normal force and pitching moment trends mimic the steady curves, but at about 2 deg lower angle and a slight undershoot of the normal force.

Pressure data corresponding to this flow regime are shown in Figures 4.15(p.3) through 4.21(p.3) for the incidence range of 19.37 deg to 28.38 deg. The equivalent steady data are shown in Figures 4.13(p.2) through 4.19(p.2) for the incidence range of 19.45 deg to 24.45 deg. The trends in pressure distributions are very similar, except that the maximum angle range has been extended by about 4 deg from 24.45 deg to 28.38 deg. The next angles of 29.71 deg in Figure 4.21(p.3) and 25.43 in Figure 4.19(p.2) both show the breakdown of the strake vortex signature at pressure row 7.

Pitch-down pressure data for this flow regime are shown in Figures 4.47(p.3) through 4.51(p.3) for the incidence range of 23.95 deg to 17.67 deg. At the upper end of this range, this pitch-down pressure distributions at 23.95 deg in Figure 4.47(p.3) are similar in shape, but not in amplitude, as compared with the steady data in Figure 4.19(p.2) at 24.45 deg. A close match in pressures is seen in the dynamic data at 22.37 deg in Figure 4.49(p.3) with steady data in Figure 4.17(p.2) at 22.44 deg. Finally, dynamic data at 17.67 deg in Figure 4.51(p.3) agrees quite well with the steady distribution at 18.45 in Figure 4.13(p.2).

Flow visualization data for pitch-up are shown in Figures 4.16 through 4.24(p.3) for the angle range of 19.46 deg to 30.22 deg. These images are very similar to those for steady flow shown in Figures 4.14 through 4.20(p.2) for the angles of 18.50 deg through 25.4 deg. Both dynamic images in Figure 4.24(p.3) at 29.20 deg and 30.22 deg are very close to those for steady conditions in Figure 4.20(p.2) at 24.3 deg and 25.4 deg. This approximately agrees with the pressure data correlations that the maximum angle for this flow regime on pitch-up is extended by about 4 or 5 deg.

Pitch-down flow visualization data shown in Figures 4.46 through 4.52(p.3) correspond to the angle range of 25.76 deg to 18.22 deg. The images at 25.76 deg in Figure 4.46(p.3) and 24.52 deg in Figure 4.48(p.3) appear to bracket this image seen in Figure 4.20(p.2) for steady flow at 25.4 deg. This agrees with the pressure data comparisons where the transition back to this shocklet/finger vortex structure was about the same for both steady and pitch-down conditions.

5.2.5 Unsteady Turbulent Separation Boundary for $M = 0.9$

The pitch-up curve in Figure 20 for normal force shows that the maximum value is achieved at about 32 deg which corresponds to the turbulent separation boundary flow regime for dynamic flow. After this point, the normal force quickly falls off. Pitching moment trends for pitch-up approach and follow the steady trend, but on pitch-down become less nose-up and crossover to more nose-up at about 32 deg. After this maximum angle, dynamic normal force falls to below the steady levels and remains so back to the re-establishment of the shocklet/finger vortex structure at about 25 deg.

Unsteady pressure data during pitch-up are shown in Figures 4.23(p.3) through 4.31(p.3), corresponding to angles of 30.99 deg to 37.60 deg. Steady pressure data for this condition are shown in Figures 4.19 through 4.27(p.2) for the angles of 25.43 deg to 36.39 deg. Comparing the two data set reveals amazing similarities with the dynamic data again displaced to a higher angle. For example, the dynamic pressure distribution at 36.43 deg in Figure 4.29(p.3) is virtually identical to that for steady flow at 32.40 deg in Figure 4.25(p.2).

The pitch-down pressure data are shown in Figures 4.33 through 4.47(p.3) for the angle range of 37.7 deg to 23.95 deg. This stalled flow condition at the maximum angle is quite evident in Figure 4.33(p.3) where the strake vortex has broken down at pressure

row 5. This condition remains during pitch-down to 32.30 deg in Figure 4.41(p.3) where the strake and wing vortices start to show up in the pressure rows 5 and 6. As pitch-down continues, the shape of the pressure distributions develop in a manner similar to steady flow, but at lower amplitudes.

Comparisons of flow visualization for pitch-up is not too meaningful, because the upper angle in the pitching motion was 34.97 deg for this test. Thus, the effects of pitch rate in the data are very low during the pitch-up portion of this flow regime.

Pitch-down flow visualization data are more useful as shown in Figures 4.34 through 4.28(p.3) corresponding to the incidence range of 34.7 deg to 24.52 deg. Compared with steady data in Figures 4.20 through 4.28p.2), the stalled characteristic persists on pitch-down to 30.22 deg in Figure 4.42(p.3), after which the steady characteristics are repeated at comparable angles. For example, compare Figure 4.46(p.3) at 26.96 deg with the image at 26.4 deg in Figure 4.22(p.2).

6.0 STEADY AND UNSTEADY LCO-TYPE FLOWS FOR THE WING WITH/WITHOUT TIP STORES

This section presents discussions on pressure data for the clean wing and flow visualization data for the clean wing with and without tip stores for LCO conditions at $M = 0.85$ and 0.90 . The data to be discussed are the figures in Sections 5.0 and 6.0 of Part 2 (Steady) and Sections 3.0, 4.0, and 5.0 of Part 3 (Unsteady) of this report. Prior to the aerodynamic discussions of pressure and flow visualization data, a discussion will be given on the LCO that was encountered during this test only on the wing with tip launcher.

6.1 Model LCO with Wing Tip Launcher

An unexpected occurrence of severe LCO on the model with wing tip launcher was encountered at the beginning of this test. The levels of tip balance loads quickly approached design limits at the LCO onset even without model excitation. A vivid demonstration of this LCO is provided in the high speed video tape and in the composite 26-minute video tape described in Section 3.5 of this part, where the LCO is actually visible. The planned test Mach number of 0.90 was relaxed to $M = 0.85$ which gave some relief at higher angles of 10.0 deg, but the maximum angle also was restricted to 8.5 for model excitation. Thus, the planned test program for wing with tip launcher configuration was significantly reduced. In addition, much wind tunnel time was consumed in the identification of the problem, as well as in the changing of test conditions, particularly angle of attack.

The LCO involved the tip store pitch mode of the model shown in Figure 21 for the wing with tip launcher with a frequency of 70.0 Hz. The corresponding mode for the wing with tip launcher and missile is shown in Figure 22 which had a frequency of 68.5 Hz. These two modes are very close in frequency, but are slightly different where the tip missile configuration shows more wing motion. Each store was mounted on a balance designed for the expected store loads. Thus, the lighter and smaller launcher balance was more flexible than the balance for the heavier and larger launcher/missile combination. This resulted in a nearly constant ratio of balance stiffness to store mass, which in turn resulted in the two tip store frequencies of 70.0 Hz and 68.5 Hz being almost identical. The more interesting consequence was that very different aerodynamic characteristics of the two tip stores were tested under LCO-type conditions while the structural dynamic characteristics were held nearly constant.

Measured tip store responses obtained from wing tip balance output data for the model oscillating at ± 0.5 deg are shown in Figure 23 for the zero harmonic (steady mean), first harmonic (at the forcing frequency), and the second harmonic (at twice the forcing frequency). In each case, the forcing frequencies were different at 36 Hz for the launcher configuration and 40 Hz for the missile configuration. Thus, second harmonics were 72 Hz and 80 Hz, respectively. Although data are shown in Figure 23 for the model

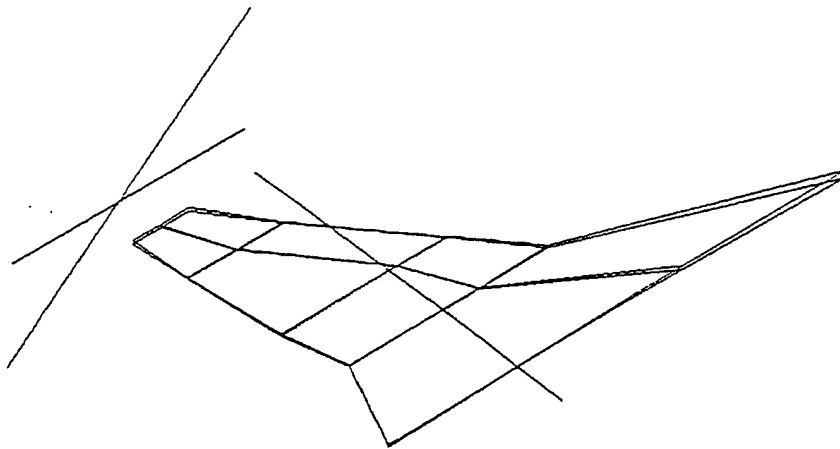


Figure 21 - Tip Launcher Pitch Mode on the Straked Wing Model at 68.5 Hz

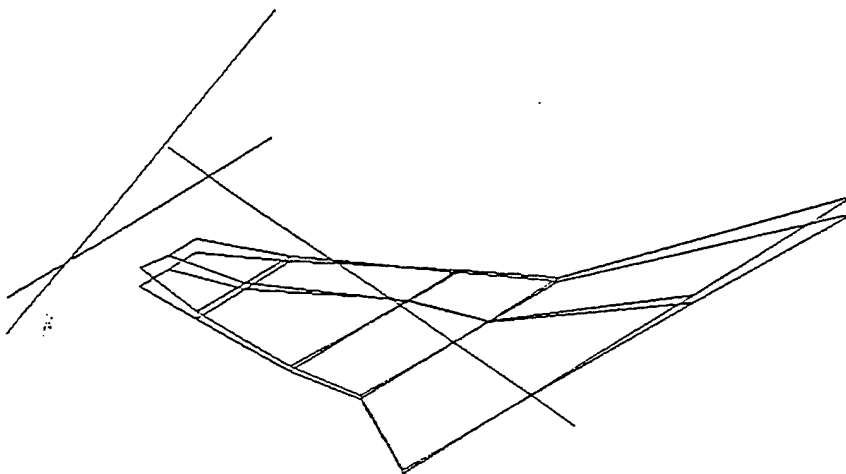
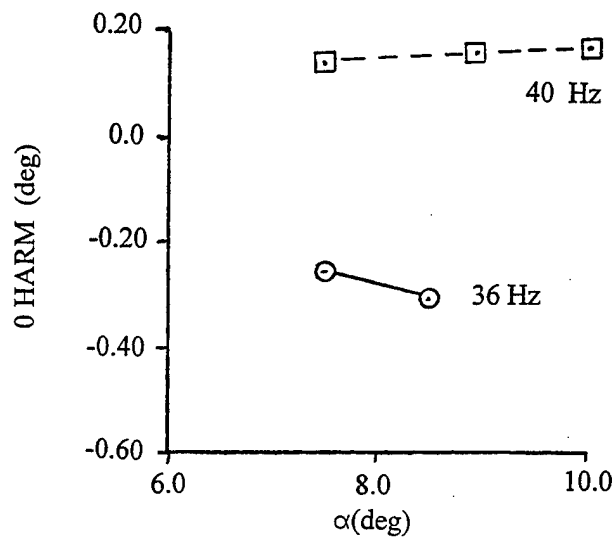


Figure 22 - Tip Missile/Launcher Pitch Mode on the Straked Wing Model at 70.0 Hz



⊙ Launcher, 36 Hz and 72 Hz

□ Mis/Lau, 40 Hz and 80 Hz

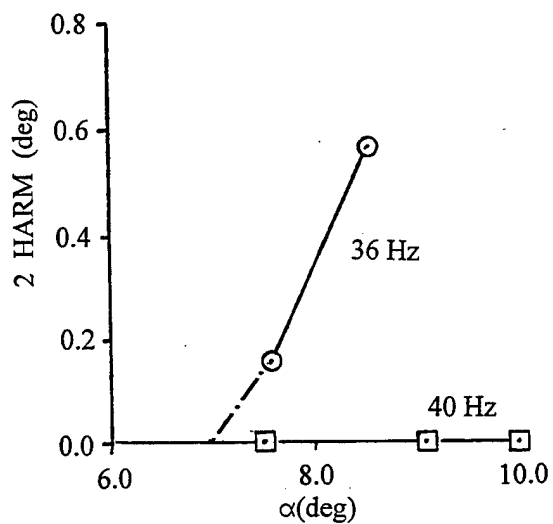
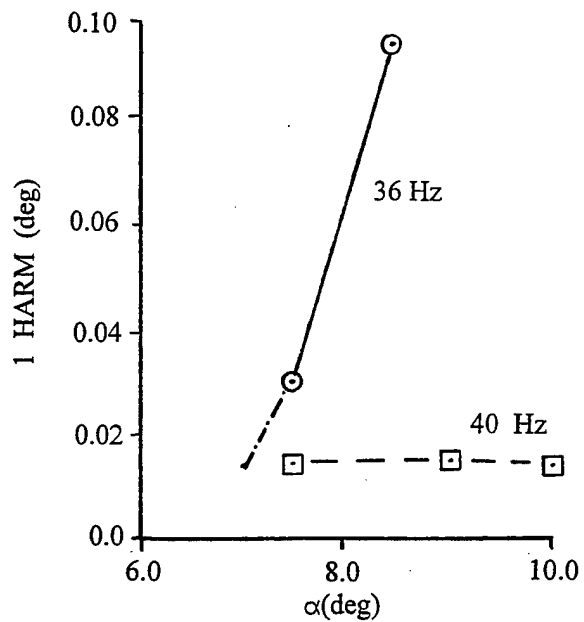


Figure 23 - Angular Response of the Tip Launcher Configuration During LCO,
 $M = 0.85$, $d\alpha = \pm 0.5$ deg

under forced oscillation, the LCO trends were the same for unforced conditions. These data were available from the NLR data processing system and only during forced model motion where a distinct input was required in order to obtain a distinct output.

Trends for the static mean zero harmonic data in Figure 23 reflect the effect of a more nose-up moment on the tip balance for the missile/launcher combination than for the launcher only. The positive (nose-up) deflection of about 0.15 deg for the former is contrasted to the negative (nose-down) deflection for the latter.

The first harmonic amplitudes shown in Figure 23 illustrate how the launcher configuration experiences a rapid onset of LCO at some angle below 8.0 deg, whereas the missile/launcher configuration shows low-level constant response up to 10.0 deg. An even more striking difference is observed in the second harmonic results where the amplitudes for the launcher configuration of up to 0.64 deg are about 10 times those for the first harmonic and are nearly the same as the forcing amplitude of ± 0.5 deg. The missile/launcher configuration second harmonic responses are essentially zero.

Since the tip store pitch mode for the launcher configuration is 70.0 Hz which is very close to the second harmonic of 72.0 Hz for the forcing frequency, it is not surprising that this LCO becomes very noticeable for that harmonic. The same reasoning applies to the missile launcher configuration whose tip store pitch mode has a frequency of 68.5 Hz and the second harmonic is at 80 Hz where, if this mode was involved in an LCO, it would also show up in the second harmonic. The absence of significant response for the missile/launcher configuration in either mode confirmed that it did not experience LCO within the conditions tested. It was also not necessary to restrict this configuration to lower speeds and angles as was the launcher configuration.

6.2 Steady Aerodynamic Characteristics for LCO-Type Flows

The pressure data appropriate to discussions in this section are shown in Figures 4.01 through 4.05(p.2) for $M = 0.9$ at angles from 6.45 deg to 11.39 deg. These data were discussed in Section 5.1.1 and 5.1.2 for the clean wing with regard to the interactions of the forward and aft shocks with increasing incidence. As the angle increases, the forward shock's aft sweep angle also increases until it crosses the aft shock. This shock intersection produces a much stronger shock that results in shock-induced separation that extends to the trailing edge referred to as SITES (Reference 10). It was shown in References 11, 12, and 13, that SITES onset can produce LCO, provided modes of vibration are present which have the proper characteristics to couple with SITES in a non-linear aeroelastic process.

Pressure data for the wing with tip stores configurations were obtained in the 1991 test at NLR (References 7 and 8) with a fixed fuselage. The presence of the fuselage produced a stronger aft shock than was observed on the simple straked wing; hence, the process leading to SITES onset occurred at lower angles than were observed in the

current test with the same tip store on the simple straked wing. Consequently, no pressure data are available that correspond to the current test configuration with the tip launcher and with the tip missile/launcher combination. Similarity of the flows, but at different angles, will be shown in this section.

The following discussions will address the effects of tip stores by examining (1) the clean wing, (2) wing plus tip missile/launcher, and (3) wing plus tip launcher. The tip launcher case will be discussed last, because the data base is not as complete due to limitations imposed by the LCO discussed in Section 6.1, above.

6.2.1 Clean Wing LCO-Type Flows

Flow visualization data presented in Section 5.0 of Part 2 of this report, Figures 10.01 through 10.09(p.2), for $M = 0.9$ on the clean wing and wing with tip missile/launcher in a side-by-side format. The sheet positions are 11, 12, and 13 as shown in Figure 10, proceeding from the tip leading edge (11), to the tip mid-chord (12), to the tip trailing edge (13). These sheet positions provide spanwise cross-sections through the chordwise flow visualization data obtained with the side view camera shown in the corresponding Figures 6.01 through 6.10(p.2). Because emphasis was on the wing tip for LCO-type flows, the inboard edge of the frame did not extend far enough to capture the strake vortex as well. However, that flow regime was covered by other data in this test.

The pre-SITES development of the shear layer, both chordwise and spanwise, with incidence as shown in Figures 10.01 through 10.08(p.2) for the clean wing, is regular and follows that seen in Figures 6.01 through 6.05 (p.2) for the side view camera. The aft shock is most likely located just aft of the sheet position 12, and the forward shock diagonally cuts the sheet position 11 at increasingly inboard stations with increasing angle. According to the pressure data in Figure 4.01(p.2) at 6.45 deg, this crossing is between pressure rows 3 and 4. At 7.45 deg, the crossing is right at pressure row 3. In Figure 4.03(p.2), the crossings are between pressure rows 2 and 3 at both 8.39 deg and 9.38 deg. At 10.39 deg in Figure 4.05(p.2), the crossing is at about the same location as it was at 9.38 deg. The difference between 10.39 deg and 9.38 deg pressures is the spanwise propagation of trailing edge pressure divergence seen at the higher angle.

The shape of the shear layer images at positions 11 and 12 are not clear at all near the wing tip, although position 12 images are a little better. The position 13 data at the trailing edge, however, are very clear and show considerable detail in the wing tip region, especially toward the higher angles. The vertical shape seen at 6.5 deg in Figure 10.01(p.2) develops with an inflection that continues up to 8.0 deg in Figure 10.04(p.2) where a small "foot" is becoming visible. The "foot" likewise develops with a shock that is clearly seen at 9.5 deg in Figure 10.07(p.2). This last characteristic remains until SITES occurs above 10.5 deg. (The shock actually exists at the lower angles starting at 6.5 deg in Figure 10.01[p.2], but is not easily seen until 9.5 deg in Figure 10.07[p.2]).

The inboard edge of this vertical tip portion of the shear layer lines up approximately with the pressure section 4 at the wing tip. Pressure data at Section 4 in Figures 4.01 and 4.03(p.2) indicate that trailing edge separation exists at the angles shown, 6.45 deg to 9.38 deg, and extends to 10.39 deg in Figure 4.05(p.2). This suggests that either the flow is locally separated outboard of the shear layer or that the characteristic shape is produced by the wing tip vortex. The latter seems more plausible, but the explanation becomes more complicated when the "foot" and strong shock begin to appear. This structure may be related to the "s-transition" noted in Section 5.1.3 which is presumably a result of wing vortex interaction with the shear layer. These characteristics in the wing tip region may best be further investigated through computational fluid dynamics (CFD) where details of the flow can be more closely scrutinized. PIV tools may also provide sufficient information to establish what these flow fields actually look like.

Flow visualization data for the clean wing at $M = 0.9$ are shown in Figure 24 at 11.0 deg for sheet position 12. These frames are from a consecutive sequence in time at 576 frames per second to illustrate the unsteady nature of the wing tip flow separation process. The image in Frame 870 appears to be associated with SITES where the pulsed laser frames at sheet position 3 in Figures 8.04, 8.05, and 8.06(p.2) at 10.5 deg provide a streamwise cut at pressure row 3. The same image exists in frame 871, but starts changing in 872, as evidenced by blurring of the image outboard of pressure row 3. In Frames 873, 874, and 875, a double image develops where a distinct structure with shock appears just above pressure row 3. The outer structure diminishes in the Frames 876 and 877, and has disappeared in Frame 878.

This last structure which is constant until the end of the sequence in Frame 881, is representative of local leading edge separation. The corresponding pulsed laser frames are shown in Figures 8.07 and 8.08(p.2) which provide a streamwise cut at pressure row 3 of the image in Frame 881. As discussed in Section 5.1.2, this structure was repeatable and agrees with the momentary stability shown in Frames 877 through 881 in Figure 23. Referring to Figure 8.07(p.2), the position of sheet position 11 is about 70% chord where the dark separated region below the bright area should correspond to the space below the outboard bottom of the shock/shear layer image at pressure row 3 in Figure 24, Frames 877 to 881. The bright region above the separated region in Figure 8.07(p.2) should likewise correspond to the outboard bright position or the shock/shear layer. This comparison and its implications will be discussed further in the next subsection.

The images in Figure 24 establish a pattern for the identification of local flow structures in the wing tip region. That of Frames 870 and 871 represent SITES flow; and leading edge separation is represented by the image in Frames 877 through 881. These images will be used in the following subsections to evaluate the effects of wing tip stores on these flow fields.

6.2.2 Wing with Tip Missile/Launcher LCO-Type Flows

The side-by-side images shown in Figures 10.01 through 10.09(p.2) are arranged to highlight the differences between the wing tip flow visualization data for the clean wing and the wing with tip missile/launcher. Only minute differences are seen in Figures 10.01, 10.02, and 10.03(p.2) for angles corresponding to 6.5 deg, 7.0 deg, and 7.5 deg. The shear layer positions are slightly higher at all three sheet positions for the missile/launcher data, but their characteristic shapes are the same. The sharp spike seen at sheet position 13 just inboard of the aft missile fins is not a flow feature, but is a reflection of the laser from a bright spot on the model.

At 8.0 deg in Figure 10.04(p.2), the onset of SITES is observed at sheet position 12 for the missile/launcher data. This is identified on the basis of similarity to Frame 870 in Figure 24 discussed in the previous subsection. Sheet position 13 also shows a corresponding inboard movement of the vertical section of the shear layer, along with a zone of separated flow that is seen between the vertical shear layer section and the aft missile fins. Conversely, no activity is shown forward at sheet position 11 which is also confirmed by video recording sequences at 8.0 deg included in the edited 26-minute video tape described in Section 3.0(see Table1). The characteristics shown at 8.0 deg in Figure 10.04(p.2) are also shown at 8.5 deg in Figure 10.05(p.2) and at 9.0 deg in Figure 10.06(p.2). Some minor changes occur at sheet position 13, but the basic shape is unchanged.

Local leading edge separation is shown at 9.5 deg in Figure 10.07 as observed at sheet position 12 for the missile/launcher data. Again, the assessment is based on similarity with the clean wing data at 11.0 deg in Figure 23 where Frames 877 through 881 represent local leading edge separation. Evidence of this is shown at all three sheet positions, including position 11. The spanwise location of separation at each sheet position is similar where the two forward positions, 11 and 12, are just outboard of pressure row 3, and position 13 is very close to that row. Images at positions 12 and 13 are very similar in character where the aft image is higher above the wing. Data in Figure 10.08(p.2) at 10.0 deg are virtually identical to those at 9.5 deg. The same is true at 10.5 deg in Figure 10.09(p.2), with exception of data at the forward sheet position 11 where the next phase of leading edge separation is shown. This image is not believed to be consistent with those at positions 12 and 13 at 10.5 deg.

The streamwise alignment of the separation points at the three sheet positions in Figures 10.07 and 10.08(p.2) agrees with the pulsed laser frames at 11.0 deg in Figures 8.07 and 8.08(p.2). This also implies that the vortical structure in the shear layer in the pulsed laser frames at 11.0 deg is possibly oriented in a nearly streamwise direction. Such a postulation would explain the elongated cross-section of the larger vortical structures shown in these streamwise cuts through the flow field.

Figure 25 shows a summary of the locations for the outboard termination of the shear layer at the three sheet positions included in Figures 10.01 through 10.09(p.2). The

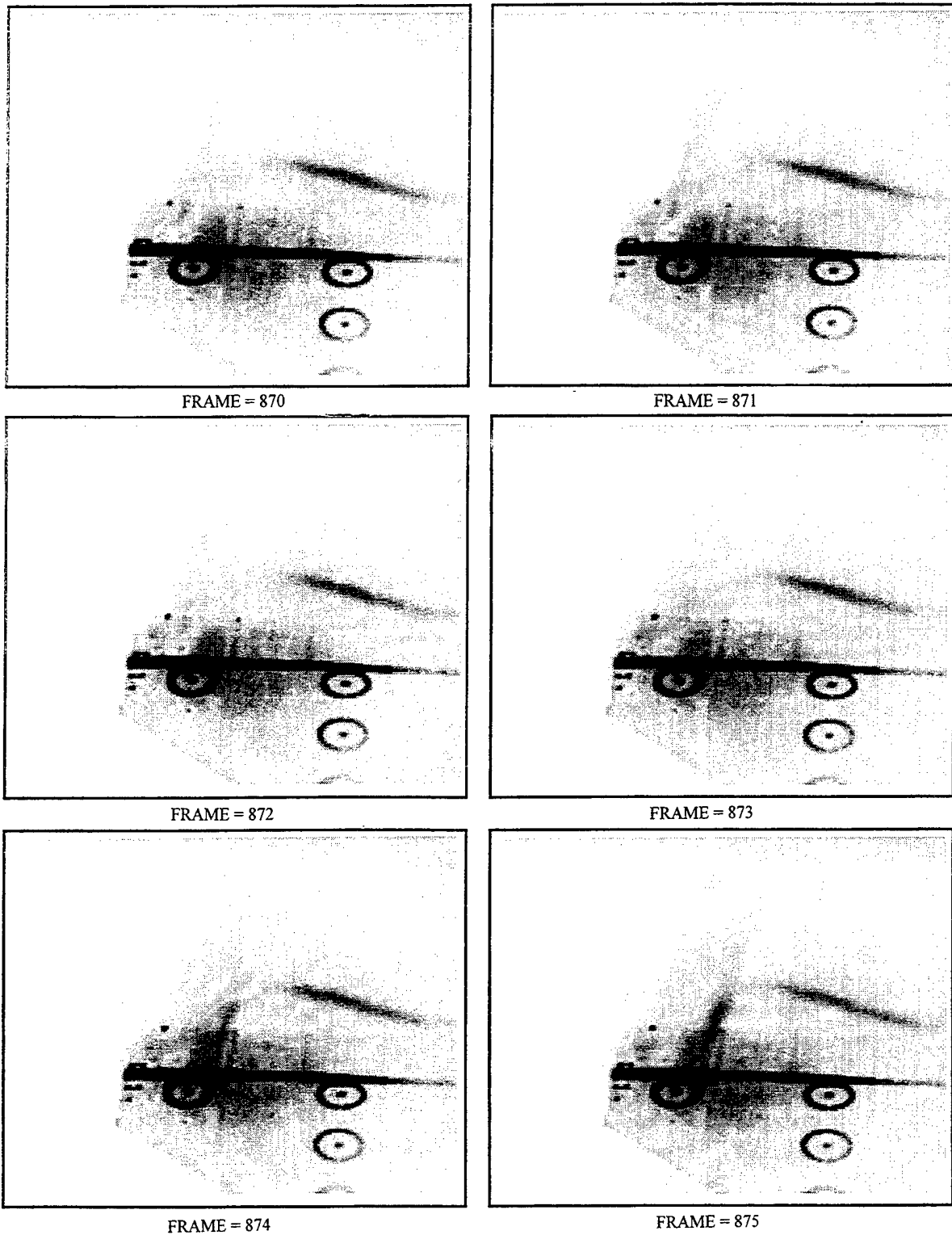
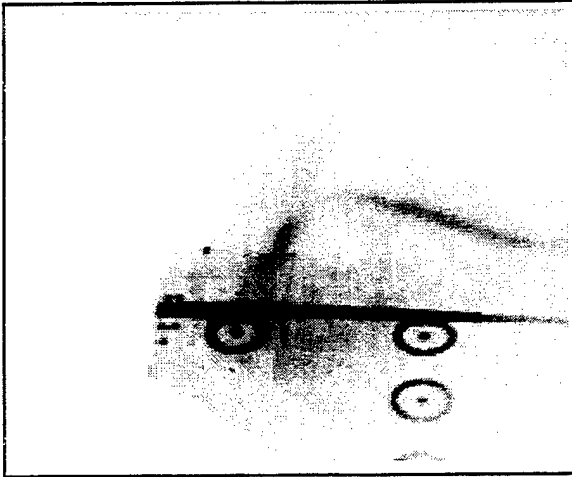
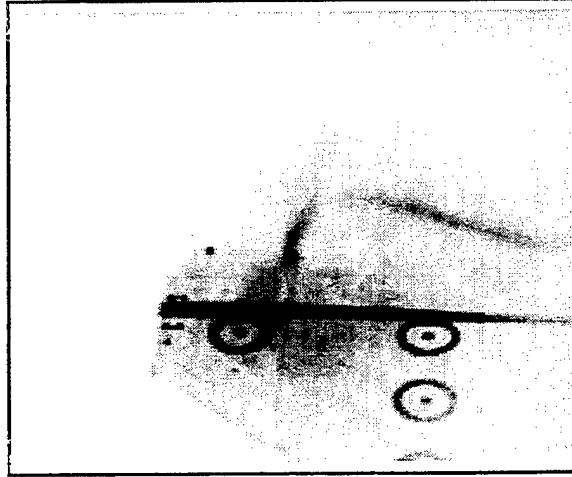


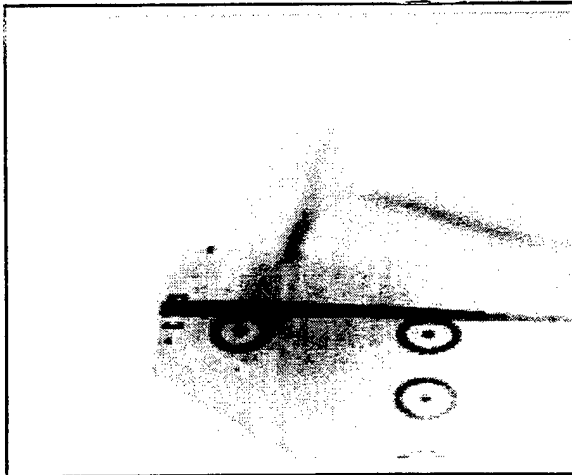
Figure 24 - Flow Visualization for the Clean Wing at $M = 0.9$, $\alpha = 11$ deg (Stationary), Time Sequence Showing Natural Unsteadiness (Data Point 47, Sheet Position 12)



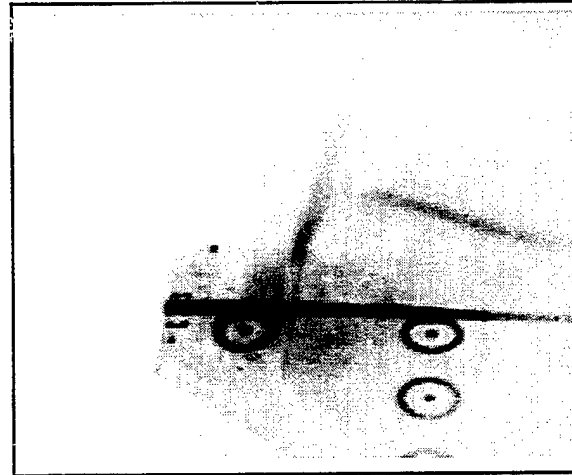
FRAME = 876



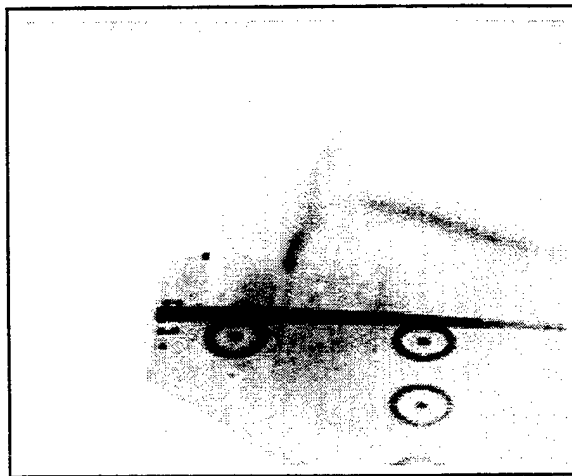
FRAME = 877



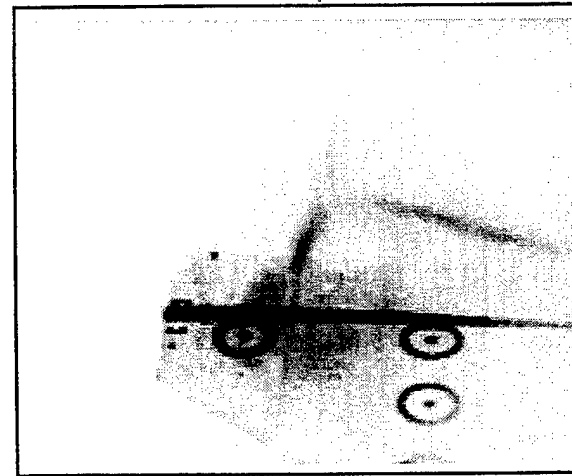
FRAME = 878



FRAME = 879



FRAME = 880



FRAME = 881

Figure 24 - Continued

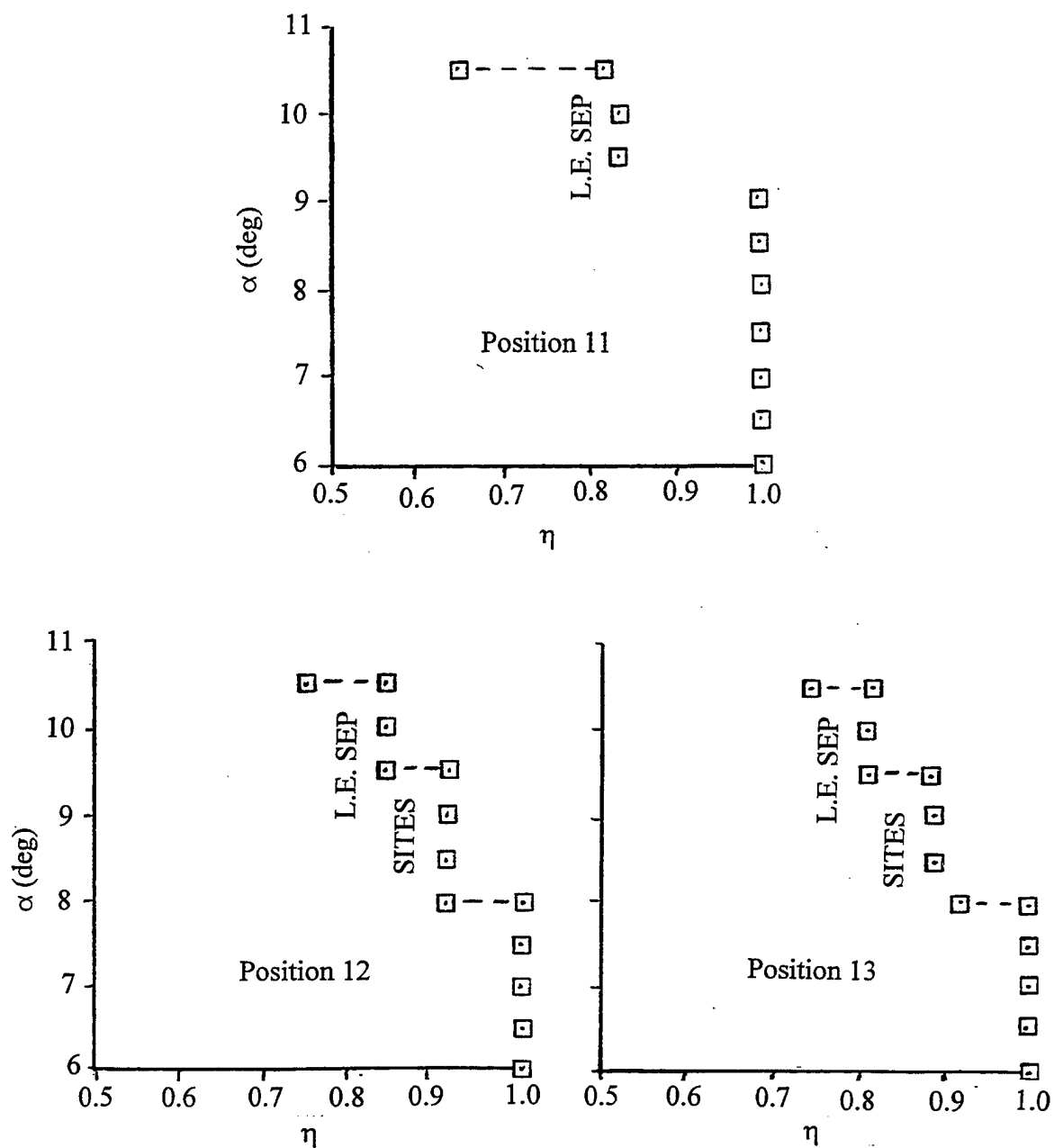


Figure 25 - Variation of Spanwise Separation Locations at the Three Sheet Positions, 11, 12, and 13 at $M = 0.9$ for the Tip Missile/Launcher Configuration

stepwise nature with transition zones with respect to incidence is very clear in this figure, as well as the distinction between SITES and leading edge separated flows. It also emphasizes the importance of such flow transitions on the aeroelastic behavior of flexible wings which can produce LCO. A sequence of frames corresponding to the transition at 9.5 deg seen at sheet position 13 is shown in Figure 26 where three flow states are illustrated (1) leading edge separation in Frames 870 and 879, (2) transition in Frames 880 and 887, and (3) SITES in Frames 888 and 901. Note that the jumps from (1) to (2) and from (2) to (3) occur in consecutive frames.

6.2.3 Wing with Tip Launcher LCO-Type Flows

Flow visualization data for the wing with tip launcher is not as systematical as those data for the clean wing and the wing with tip missile/launcher configurations. Because of the LCO encountered with the tip launcher, most of the data were taken for $M = 0.85$ at angles that were lower than those for the other two configurations.

The data shown in Figures 12.01, 12.02, and 12.03(p.2) are for $M = 0.9$ and 0.85 at sheet position 11 and for $M = 0.85$ at sheet position 12. Similar trends are seen in the $M = 0.9$ data at sheet position 11 in these three figures (at 6.5 deg through 8.5 deg) and comparable clean wing data in Figures 10.01 through 10.05 (p.2). Comparing $M = 0.9$ and $M = 0.85$ data in Figures 12.01, 12.02, and 12.03(p.2) for sheet position 11 also shows similar trends in the shear layer development. It is interesting to note, however, that the $M = 0.85$ images are very close to those at $M = 0.9$ but at 0.5 deg lower in incidence. This is demonstrated by the $M = 0.85$ data at 7.5 deg and the $M = 0.9$ data at 7.0 deg in Figures 12.02 and 12.01(p.2), respectively.

The sheet position 12 data in Figures 12.01, 12.02, and 12.03(p.2) are all at $M = 0.85$ and correspond to the $M = 0.85$ data at sheet position 11 in the same figures. Referring to Figure 23, the onset of LCO occurred between 7.5 deg and 8.5 deg at $M = 0.85$ with the wing oscillating in pitch at ± 0.5 deg and 36 Hz. The appearance of SITES is observed at 7.0 deg in Figure 12.01(p.2) at sheet position 12 but, as expected, not at position 11. This characteristic is first identified by the outboard vertical tip of the shear layer at 7.0 deg and is more visible at 7.5 deg through 8.5 deg in Figures 12.02 and 12.03(p.2). At 9.0 deg in Figure 12.03(p.2), the flow is transitioning to leading edge separation in the vicinity of pressure row 3. The fact that LCO onset angle is above that for SITES onset at 7.0 deg, but agrees with occurrence of leading edge separation between 8.5 deg and 9.0 deg indicates that SITES might not be the primary transition that is involved in this particular non-linear aeroelastic example. The mechanism for the LCO will be further discussed in connection with the oscillating model data in the following subsections.

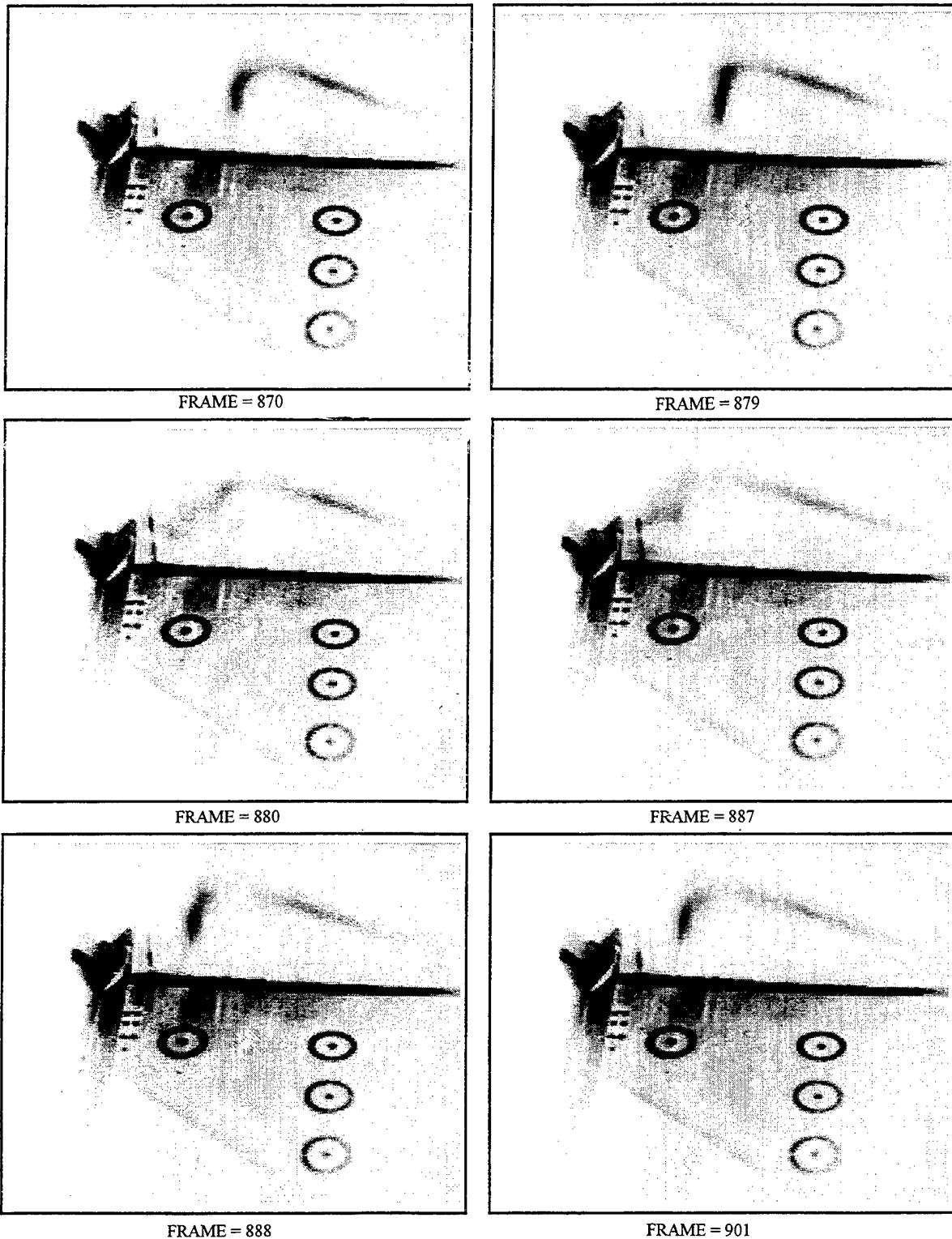


Figure 26 - Flow Visualization for the Tip Missile/Launcher Configuration at $M = 0.9$, $\alpha = 9.51$ deg (Stationary), Illustrating Multiple Flow States (Data Point 261, Sheet Position 13)

6.3 Oscillatory Aerodynamic Characteristics for LCO-Type Flows

The flow visualization data to be discussed in this section are shown in Part 3 of this final report in Sections 3.0, 4.0, and 5.0 where in all cases, this model is executing forced pitch oscillations at 36 Hz and ± 0.5 deg amplitude. These discussions are organized in the same manner as Section 6.3 for the steady characteristics where the effects of tip stores will be illustrated by examining (1) the clean wing, (2) wing plus tip missile/launcher, and (3) wing plus tip launcher. The discussions on the tip launcher case will also address the LCO encountered with that configuration.

6.3.1 Oscillating Clean Wing LCO-Type Flows

Flow visualization data are presented in Section 3.0 of Part 3 of this report, Figures 6.01, 6.02, and 6.03(p.3), for $M = 0.9$ on the clean wing. The data are shown at four phase angles: (1) 0.0 deg for model pitching-up through mean incidence; (2) 90.0 deg for maximum incidence; (3) 180.0 deg for model pitching-down through mean incidence; and (4) 270.0 for minimum incidence. The three wing tip sheet positions, 11, 12, and 13, are also used in these figures to correspond with those discussed in Section 6.2, above.

The oscillatory data in Figure 6.01(p.3) are for a mean angle of 8.0 deg with a ± 0.5 deg amplitude. The three angular positions of mean at 8.0 deg (phase angles 0.0 deg and 180 deg), at maximum at 8.5 (phase angle 90.0 deg), and minimum at 7.5 deg (phase angle of 270.0 deg) correspond to the steady data shown in Figures 10.04, 10.05, and 10.03(p.2), respectively. A close examination of these two sets of figures shows that some lagging is present at the two forward sheet positions, but it is much higher at the trailing edge sheet position. At this last position, the shear layer image at phase angle 180 deg appears to be at a higher incidence than that at phase angle 90 deg where the maximum incidence actually occurs. In fact, the image at 180 deg phase angle looks more like the steady image at 9.0 deg in Figure 10.06(p.2). Other than this observation, the unsteady effects are as expected.

Figure 6.03(p.3) presents oscillatory data for a mean angle of 9.0 deg. The corresponding steady data at the angles of 8.5 deg, 9.0 deg, and 9.5 deg are shown in Figure 10.05, 10.06, and 10.07(p.2), respectively. At this mean angle, the oscillatory data lag at all three sheet positions in a manner similar to that shown in Figure 6.01(p.3) at 8.0 deg. The large differences seen at sheet position 13 in Figure 6.03(p.3) are not present in Figure 6.02(p.3).

A similar comparison at 10.0 deg between the oscillatory data in Figure 6.03(p.3) and the steady data in Figures 10.07, 10.08, and 10.09(p.2) also shows that a consistent lagging characteristic is seen at all sheet positions. On this basis, it is believed that the oscillatory data for sheet 13 shown in Figure 6.01(p.3) may not be correct at the phase angle of 180 deg.

6.3.2 Oscillatory Wing with Tip Missile/Launcher LCO-Type Flows

Flow visualization data are presented in Section 4.0 of Part 3 of this report, Figures 8.01, 8.02, and 8.02(p.3) for $M = 0.9$ on the oscillating wing with the tip missile/launcher and in Figure 9.01(p.3) for $M = 0.85$. These data are shown in the same format as those data for the clean wing.

The oscillatory data in Figure 8.01(p.3) are for a mean incidence of 8.0 deg at $M = 0.9$ with minimum and maximum angles of 7.5 deg and 8.5 deg, respectively. The corresponding steady data in Part 2 are Figures 10.03, 10.04, and 10.05(p.2) for the angles 7.5 deg, 8.0 deg, and 8.5 deg, respectively. The primary transition that is seen within this range is SITES at 8.0 deg, as discussed in Section 6.2.2 for steady flow. This transition is likewise seen in the oscillatory data in Figure 8.01(p.3). It appears that the lagging of the SITES onset and re-attachment is greater than the lagging seen in changes for the shape of the shear layer at all three sheet positions.

At the mean incidence of 9.0 deg, the oscillatory data for $M = 0.9$ in Figure 8.02(p.3) correspond to the steady data in Figures 10.05, 10.06, and 10.07(p.2) at the angles of 8.5, 9.0, and 9.5 deg, respectively. Comparisons between oscillatory and steady data at the four phase angles show that the images at all sheet positions track very well with a small lag. Sheet position 13 at 0.0 deg phase angle appears to be showing a greater tendency to re-attach from SITES during pitch-up as might be expected. This is downstream of sheet position 12 which does not show the same tendency.

Finally, at $M = 0.9$ and 10.0 deg mean angle, the oscillatory data are shown in Figure 8.03(p.3). The mean angle is above the point at which wing tip leading edge separation occurs at 9.5 deg, as discussed in Section 6.2.2. This is seen in the corresponding steady data in Figures 10.07, 10.08, and 10.09(p.2) at angles of 9.5 deg, 10.0 deg, and 10.5 deg, respectively. Unlike the SITES transition at 8.0 deg, the leading edge separation seems to not be very sensitive to model pitching motion. Comparisons of the oscillatory images with those for steady flow, show the typical small lag.

For purpose of comparison with data for the wing with tip launcher, data for the wing with missile/launcher are shown in Figure 9.01(p.3) for a mean angle of 9.0 deg at $M = 0.85$. The primary effect of a lower Mach number is the occurrence of leading edge separation at a lower angle. This is illustrated by a comparison of Figures 9.01 and 8.02(p.3) at $M = 0.85$ and 0.9, respectively. Leading edge separation exists throughout the cycle at $M = 0.85$, whereas SITES dominates the flow at $M = 0.9$. In addition, inboard excursions of leading edge separation are also observed at phase angles of 90.0 deg and 180.0 deg at $M = 0.85$.

6.3.3 Oscillatory Wing with Tip Launcher LCO-Type Flows

Flow visualization data are presented in Section 5.0 of Part 3 of this report, Figures 11.01 and 11.02(p.3), for $M = 0.85$ on the oscillating wing with tip launcher. The format is the same as for the clean wing.

The oscillatory data shown in Figure 11.01(p.3) are for a mean incidence of 7.5 deg with minimum and maximum angles of 7.0 deg and 8.0 deg. The corresponding steady data for sheet positions 11 and 12 at $M = 0.85$ are given in Part 2, Figures 12.01 and 12.02(p.2). The primary transition that occurs within the incidence range of 7.0 deg to 8.0 deg is SITES at 7.0 deg, as shown in Figure 12.01 (p.2). The oscillatory data in Figure 11.01(p.3) do not show a change from SITES dominated flow, but instead show a modulation of SITES as the spanwise position moves inboard at the peak angle (90.0 deg phase) and outboard at the lower angles. The shear layer image also shows a small lag as observed for the other configurations and conditions.

A puzzling picture is presented, however, at 8.5 deg in Figure 11.02 where high response of the tip store pitch mode was encountered in an LCO (see Figure 23). This incidence range of 8.0 deg to 9.0 deg is covered by steady data in Figure 12.02 and 12.03(p.2) at $M = 0.85$, where SITES is dominant at 8.0 deg and 8.5 deg, but leading edge separation is starting at 9.0 deg. It was stated in Section 6.2.3 that the LCO onset appeared to correlate with that of leading edge separation. The data shown at the four phase angles in Figure 11.02(p.3) do not show any existence of leading edge separation. The same is true for the other 12 phase angles at this condition that are included in the data base. (Sixteen phase angles are available for each cycle of oscillation in the data base.) These data indicate that the SITES is modulated with model motion as was seen at 7.5 deg in Figure 11.01(p.2); but the modulation does not appear to be consistently correlated with the forced model motion phase angles as has been the case for other examples discussed previously.

The reason for the inconsistent correlation of flow conditions and forced model motion is that the second harmonic response, near the tip launcher pitch mode frequency, is nearly as large as the forced motion at the first harmonic. The values given in Reference 16 are listed below:

	$\alpha = 7.500$ (DPN = 190)		$\alpha = 8.495$ (DPN = 192)	
	1 st HARM	2 nd HARM	1 st HARM	2 nd HARM
Frequency, Hz	36.000	72.000	36.000	72.000
Forced Amplitude, deg	0.564	0.000	0.580	0.000
Near Wing Tip Amplitude, deg	0.645	0.049	0.662	0.057
Wing Tip Amplitude, deg	0.733	0.167	0.768	0.616
Tip Launcher Amplitude, deg	0.030	0.170	0.088	0.526

where, it is seen that the second harmonic motion is mostly confined to the outer 10% of the wing and the tip launcher. This type of wing motion for the second harmonic would be felt primarily at the wing tip and, thus in the current case, where SITES exists. A careful observation of the data in Figure 11.02(p.3) confirms this postulation to be true, in that the shear layer images inboard of the SITES boundary, do indeed show the expected correlations with model phase angle as well as the small lag seen in other cases. The inconsistency exists only in the modulation of SITES. This modulation will probably not be correlated exactly with the second harmonic at 72 Hz, since the tip launcher pitch mode (see Figure 21), which is suspected to be responding, has a frequency of 70 Hz.

Based on the above reasoning, the LCO encountered on this model with a tip launcher was probably driven by SITES in the wing tip region. Since SITES onset occurs at 7.0 deg for $M = 0.85$, this angle should also coincide with the onset of LCO for this configuration. If this is true, then the amplitude for the wing with tip launcher should be the same as that for the wing with tip missile/launcher below the SITES onset angle of 7.0 deg. The dashed lines shown in Figure 23 for the first and second harmonics of the wing with launcher case, are essentially straight line extensions of the solid lines connecting the two LCO points at 7.5 deg and 8.5 deg for both harmonics. Thus, it is confirmed that the wing tip launcher configuration LCO was very likely driven by wing tip SITES flows.

7.0 CONCLUSIONS

A flow visualization test was conducted with the simple straked wing in August, 1996 (at the National Aerospace Laboratory [NLR], The Netherlands), for the purpose of obtaining flow visualization data to complement the pressure and force data base generated in earlier tests of the same configuration. This test was conducted in two parts to examine the flow field characteristics (1) at high alpha conditions that involve vortices, shocks, and separated flows, and (2) at low alpha conditions typical of transonic LCO flows with and without tip stores. Laser light sheet/water vapor techniques were used to illuminate the flows, and video recording was used to obtain the data. Both low and high speed video cameras were used to examine spanwise and streamwise laser sheet positions. In addition, under NLR funding, some preliminary particle image velocimetry (PIV) data were obtained at $M = 0.225$ and 0.6 , as well as some pulsed laser flow visualization (9 nano-sec pulse) at $M = 0.9$.

A background summary was given to trace the steps leading up to this test starting with the low speed full span model investigation of the simple straked wing in 1986. The effects of increasing Mach number were reviewed using data from a semi-span test in 1992. A more extensive test was also reviewed where a fighter type model with wing stores was tested in 1991 at conditions typical of LCO.

A brief description was presented of the flow visualization experiment conducted at NLR in August of 1996 on the simple straked wing model. A summary was also given for the flow visualization data base contained in Part 2 of this report for the stationary model, followed by a similar summary for Part 3 of this report pertaining to the oscillating model. Finally, brief descriptions were given for several VHS video tapes which are very helpful in understanding the unsteady flow fields.

Steady and unsteady flow visualization data at $M = 0.6$ for the clean wing showed that characteristics observed at $M = 0.225$ in the 1986 full span test were applicable to the $M = 0.6$ case. This was also confirmed through analysis of the force and pressure data. The flow field regimes addressed were (1) linear flow, (2) vortex flow, and (3) burst vortex flow. Unsteady effects produced the expected aerodynamic lags in the flow fields.

At $M = 0.9$, the many complexities of transonic vortex flows were explored. Between high speed video recordings at multiple positions and conventional video data at other positions, streamwise and spanwise flow characteristics were identified. This data base was augmented by the force and pressure data obtained during an earlier test in 1992. Both spatial and temporal details were obtained of the complex interactions of primary vortices, turbulent shear layers, stalled regions, and shocks. The flow field regimes addressed were (1) attached transonic flow, (2) shock-induced trailing edge separation (SITES), and tip leading edge separation, (3) transonic vortex flow, (4) shocklets and finger vortices, and (5) turbulent separation boundary during progressive stalling.

The investigation of LCO-type flows with and without wing tip stores was restricted to the outer wing panel, but with higher resolution and at three spanwise sheet positions. Testing with the wing tip launcher was complicated by the encounter of severe LCO with this configuration involving the tip store pitching mode. This was compensated for by the opportunity to study an actual LCO in the wind tunnel with flow visualization. These data provided strong evidence that the LCO was driven by SITES in the wing tip region. The effects of adding a wing tip launcher/missile were identified where the onset angles for SITES and tip leading edge separation were lowered, but the basic flow character was not significantly changed.

8.0 REFERENCES

1. Cunningham, A. M., Jr.; den Boer, R. G., et al: Unsteady Low-Speed Wind Tunnel Test of a Straked Delta Wing, Oscillating in Pitch; AFWAL-TR-87-3098 (Parts I through VI), April 1988.
2. den Boer, R. G. and Cunningham, A. M., Jr.: "Low Speed Unsteady Aerodynamics of a Pitching Straked Wing at High Incidence - Part I: Test Program", Journal of Aircraft, Vol. 27, January 1990, pp. 23-30.
3. Cunningham, A. M., Jr. and den Boer, R. G.: "Low Speed Unsteady Aerodynamics of a Pitching Straked Wing at High Incidence - Part II: Harmonic Analysis", Journal of Aircraft, Vol. 27, January 1990, pp. 31-41.
4. Cunningham, A. M., Jr.: "A Critique of the Experimental Aerodynamic Data Base for an Oscillating Straked Wing at High Angles", Proceedings Fourth Symposium on Numerical and Physical Aspects of Aerodynamic Flows, California State University, Long Beach, California, 16-19 January 1989.
5. Cunningham, A. M., Jr. and den Boer, R. G.: "Steady and Unsteady Aerodynamics of a Pitching Straked Wing Model at High Angles of Attack", presented at the AGARD FDP Symposium "Vortex Flow Aerodynamics", Scheveningen, The Netherlands, 1-4 October 1990.
6. Cunningham, A. M., Jr. and den Boer, R. G.: "Analysis of Unsteady Force, Pressure and Flow-Visualization Data for a Pitching Straked Wing Model at High Angles of Attack", presented at the AGARD FDP Specialists' Meeting "Maneuvering Aerodynamics", Toulouse, France, 1-2 May 1991.
7. den Boer, R. G. and Cunningham, A. M., Jr.: "Unsteady Transonic Wind Tunnel Testing of Fighter Type Wings", 31st AIAA/ASME/ASCE/AHS/ASC Structures, Structural Dynamics, and Materials Conference, Long Beach, California, 2-4 April 1990.
8. Cunningham, A. M., Jr. and den Boer, R. G.: "Transonic Wind Tunnel Investigation of Limit Cycle Oscillations on Fighter Type Wings - Update", AIAA Dynamics Specialist Conference Proceedings, Dallas, Texas, 16-17 April 1992.
9. Cunningham, A. M., Jr. and den Boer, R. G.: Overview of Unsteady Transonic Wind Tunnel Test on a Semi-Span Straked Delta Wing Oscillating in Pitch, WL-TR-94-3017, WL-TR-94-3095, and WL-TR-94-3096, August 1994.

10. Cunningham, A. M., Jr. and Spragle, G. S.: A Study of the Effects of Reynolds Number and Mach Number on Constant Pressure Coefficient Jump for Shock-Induced Trailing Edge Separation, NASA CR 4090, August 1987.
11. Coe, C. F. and Cunningham, A. M., Jr.: Predictions of F-111 TACT Aircraft Buffet Response and Correlations of Fluctuating Pressures Measured on Aluminum and Steel Models and the Aircraft, NASA CR-4069, May 1987.
12. Cunningham, A. M., Jr.: "Practical Problems: Airplanes", Chapter 3, Unsteady Transonic Aerodynamics, Edited by D. L. Nixon, AIAA Progress in Astronautics and Aeronautics Series, 1989.
13. Meijer, J. J. and Cunningham, A. M., Jr.: "Understanding and Development of a Prediction Method of Transonic Limit Cycle Oscillation Characteristics of Fighter Aircraft", AIAA Paper No. 92-4501-CP, August 1992.
14. Cunningham, A. M., Jr.: A Generic Non-Linear Aeroelastic Method with Semi-Empirical Non-Linear Unsteady Aerodynamics, to be published as a Wright Laboratory Report in 1998.
15. Cunningham, A. M., Jr.: "A Preliminary Assessment of the Transonic Aerodynamic Characteristics of a Straked Wing Configuration", Lockheed Martin Tactical Aircraft Systems, Fort Worth, TX, July 1993.
16. Cunningham, A. M., Jr.; Geurts, E. G. M.; Dogger, C. S. G.; and Persoon, A.J. : Transonic Wind Tunnel Test on the Flow-Visualization of a Semi-Span Simple Straked Delta Wing Model, National Aerospace Laboratory, The Netherlands, Contract Report, CR97577L (Parts I and II), January 1998.
17. Cunningham, A. M., Jr., "Aerodynamic Aspects of Transonic Limit Cycle Oscillations", Aeroelasticity and Fluid Structure Interaction Problems, ASME Publication AD - Vol. 44, 1994.
18. Geurts, E. G. M. and Cunningham, A. M., Jr.: Flow Visualization and Particle Image Velocimetry on a Semi-Span Straked Delta Wing, Stationary and Oscillating in Pitch, National Aerospace Laboratory, The Netherlands, Report TP97261L, 1997.
19. Campbell, J. F. and Chambers, J. R.: Patterns in the Sky - Natural Visualization of Aircraft Flow Fields. NASA SP-514, 1994.